Doctoral Dissertation

博士論文

A study of star-forming galaxies at $2.1 < z < 2.5$ selected by broad-band flux excesses

（広帯域フィルターのフラックス超過を用いた赤方偏移 2.1–2.5 の星形成銀河の研究）

A Dissertation Submitted for the Degree of Doctor of Philosophy
December 2019

令和元年１２月博士（理学）申請

Department of Astronomy, Graduate School of Science,
The University of Tokyo

東京大学大学院理学系研究科天文学専攻

Yasunori Terao

寺尾　恭範

Acknowledgments

First of all, I would like to express the deepest gratitude to my supervisor, Dr. Kentaro Motohara. He has given me the opportunity of everything I have experienced during my PhD course as well as helped me improve this work with his insightful and instructive advice based on deep knowledge and great experiences in this field. I would never have successfully finished my PhD without his patient and constant support.

It has been the greatest luck for me to have a chance to work with Dr. Lee Spitler, a senior lecturer at Macquarie University. Through the collaboration with him, I have learned a lot of things about data analysis and how to discuss statistical properties of distant galaxies, which have been essential for this thesis to be what it is. Therefore I would like to offer the greatest thanks to him.

I am also grateful to Dr. Masahiro Konishi who has helped me learn computer and programming skills as well as how to operate and evaluate astronomical instruments. In addition he has given me important comments that has made the discussion in this thesis more reliable.

My appreciation goes to Dr. Hidenori Takahashi too, who has always not only encouraged me but also inspired me by his excellence in instrument development. Working with him has taught me how engineering has pushed observational astronomy forward.

Natsuko M. Kato has kindly supported my research life, especially in terms of network environment. Thanks to her I have focused on my work with comfort.

It has been my biggest pleasure to share fruitful time with all of the student members and alumni of the SWIMS development team, namely Dr. Ken Tateuchi, Dr. Yutaro Kitagawa, Soya Todo, Yutaka Kobayakawa, Hirofumi Ohashi, Yukihiro Kono, Kosuke Kushibiki and Hiroki Nakamura. Especially I have spent brilliant days with Hirofumi Ohashi, Yukihiro Kono and Kosuke Kushibiki enjoying casual discussions and conversations. They have made these five years an invaluable period in my life.

Special thanks to the members of the MIMIZUKU and Tomo-e Gozen development teams with whom I have shared lunchtime everyday with fun. Especially I and Tomohiro Mori have encouraged each other to complete our PhDs.

Finally, and sincerely, I thank my family and my friends who have always supported and encouraged me. I would like to return the favor throughout my life.

Contents

Abstract

To understand galaxy formation and evolution is one of the biggest goals of modern astronomy. In this context, thousands of observations have been conducted to investigate properties of star-forming galaxies. Most star-forming galaxies exhibit prominent emission lines in their spectra, such as Lyα, Hα, and [OIII]. Hence the emission lines have been used to detect the star-forming galaxies and derive their properties. Emission line fluxes have been usually measured from spectroscopic or narrow-band imaging data. However, such observations require long observation time to construct large samples which are necessary to investigate statistical properties of the galaxies.

In this thesis, we establish a method to derive the emission line fluxes from broad-band photometry using a multi-band photometric catalog of the Fourstar Galaxy Evolution Survey (ZFOURGE). The wide wavelength coverage (0.3–8 μm) of the ZFOURGE and its deep near-infrared broad/medium-band imaging data allow us to accurately estimate properties of the galaxies by SED fitting. When performing the SED fitting, it is important to consider effects of the emission lines, which boost fluxes in the broad-band filters. Unless these effects are taken into account, the SED fitting overestimates continuum levels resulting in overestimated stellar masses. Hence we use spectral templates in which the emission lines are included. We find that the stellar masses can be overestimated by nearly 1 dex in some cases without the emission line templates.

We define "flux excess" as a difference between an observed flux and a continuum flux derived from the SED fitting, and select Hα emitters and [OIII] emitters at $2.1 < z < 2.5$ based on the flux excesses in the $K_{\rm s}$-band and $H_{\rm s}/H_{\rm l}$-band, respectively. When comparing the Hα fluxes derived from the flux excesses with those derived from narrow-band color excesses, long-slit spectroscopy and integral-field spectroscopy, we find 73%, 67% and 62% of the Hα emitters have consistent fluxes within a factor of 2 in both methods, respectively. Scatters around the one-to-one relations are similar in any pairs among the four derivation methods. Therefore we conclude that there is no significant error introduced by using the flux excess.

We investigate properties of both the Hα and [OIII] emitters selected by the flux excesses. Almost all our Hα emitters are classified as star-forming galaxies by the UVJ diagram, which indicates that our method works properly to select the star-forming galaxies.

First we find a correlation between star formation rates (SFRs) and the amounts of dust attenuation to Hα. This suggests that more luminous Hα emitters are more obscured by the dust.

Next we compare our Hα luminosity function with that obtained by a narrow-band imaging survey named the High-z Emission Line Survey (HiZELS). Our luminosity function exhibits an excess compared to the result of the HiZELS in the bright-end, while both luminosity functions are in good agreement in the faint-end. We show that most of the difference between the luminosity functions can be explained by a combination of extended Hα profiles and the correlation between the Hα luminosity and the amount of dust attenuation. According to our simulation with structural parameters in a literature, the fixed 2" aperture of the HiZELS might have missed at most $\sim 40\%$ of Hα fluxes of galaxies in the bright-end. In addition, its luminosity function has been derived assuming the attenuation of 1 mag to Hα for all the galaxies, which are insufficient for the most luminous Hα emitters. Despite the excess, we obtain a consistent cosmic star formation rate density with previous studies as the contributions of the most luminous Hα emitters to the total SFR in the universe are insignificant due to their small numbers.

The star formation main sequence (SFMS) of our Hα emitters agrees well with those of previous studies at $\log M/M_{\odot} > 9$. On the other hand, there are many low-mass galaxies much above an extrapolation of the SFMS. Such low-mass galaxies with large specific star formation rates (sSFRs) have also large Hα/UV luminosity ratios, which suggests that they might have undergone short-period starbursts within past 10 Myr. In addition, they are also selected as the [OIII] emitters with extremely high ($\gtrsim 1000$ Å) equivalent widths. This makes their large sSFRs more reliable because the [OIII] equivalent width is an independent proxy of the sSFR.

We find that strong [OIII] emitters are characterized by large sSFRs, large [OIII]λ5007/Hβ ratios, and small amounts of the dust attenuation as expected from previous studies.

Given that the Hα emitters represent diverse populations of the star-forming galaxies, the [OIII] emitters are expected to be a sub-population of the Hα emitters. When comparing these two populations, we find that more than 70% of the [OIII] emitters are also selected as the Hα emitters, while $\sim 55\%$ of the Hα emitters are also selected as the [OIII] emitters. This result is qualitatively consistent with our expectation. However, there are uncertainties in the fractions due to different sensitivities of our selection to both emission lines.

In conclusion, the combination of our flux excess method and deep imaging data of the ZFOURGE has enabled us to discover the star-forming galaxies with extreme properties, which are important populations to better understand galaxy evolution. For example, Hα luminosities of the galaxies in the bright-end of the Hα luminosity function correspond to SFRs of a few 100 $M_{\odot}\mathrm{yr}^{-1}$. In addition, we find large AGN fraction in the bright-end. Therefore it is important to investigate the most luminous galaxies to better understand what triggers the very active star formation activities and how the AGNs are connected with them. Our method is an efficient way to detect such very rare objects.

On the other hand, the low-mass galaxies with large sSFRs are also very important populations, which are expected to be undergoing rapid stellar mass assembly. We might obtain a clue to understand the downsizing of galaxies by investigating typical stellar masses of such populations at different redshifts. In addition, since supernova feedbacks have been thought to play an important role in star formation histories of low-mass galaxies, investigating the bursty galaxies may put a constraint on the feedback models. Moreover, they are also interesting targets to understand ionizing photon escapes at this redshift because their properties are similar to those of the local galaxies with large escape fractions.

List of Figures

List of Tables

Chapter 1

Introduction

Understanding how galaxies have been formed and evolved through the cosmic time is one of the biggest goals of modern astronomy. In this chapter, we first summarize several important facts regarding galaxies revealed by recent observations and current interpretations for them (§ 1.1). Then we introduce how previous studies have selected star-forming galaxies (§ 1.2) and estimated their star formation rates (SFRs) (§ 1.3) from observational data. It is followed by a section where pros and cons of major observational methods are discussed (§ 1.4). Finally we present the aim of this thesis in the last section (§ 1.5).

1.1 Galaxy evolution through cosmic time

It is important to investigate properties of galaxies at various redshifts to understand galaxy evolution. Since all galaxies increase their stellar masses through star formation, thousands of observational studies for star-forming galaxies have been done so far. In this section, we review several important results of recent works about statistical properties of the star-forming galaxies.

1.1.1 Cosmic star formation rate density

Cosmic star formation rate density (SFRDs) are defined as SFR per unit volume. It indicates how actively galaxies form stars on average in the entire populations. Measurements of the cosmic SFRDs at various redshifts provide us with information

on the history of the stellar mass assembly in the universe.

Many previous studies have measured the cosmic SFRDs at various redshifts mainly based on rest-frame ultraviolet (UV) and/or infrared (IR) observations (e.g., Reddy & Steidel 2009, Bouwens et al. 2015, Gruppioni et al. 2013, Koprowski et al. 2017). As a result, it has been known that the cosmic SFRD has a peak at $\sim$ 10–11 Gyr ago ($z \sim 2$–3) (Madau & Dickinson 2014). Galaxies have formed stars most actively at this epoch on average.

For accurate measurements of the cosmic SFRDs, It is important to select all star-forming galaxies without biases toward specific populations as well as to take dust attenuation into account. Some previous studies have corrected UV luminosities for the dust attenuation, while others have added IR luminosities to the UV in order to derive total SFRs. On the other hand, Fujimoto (2019, PhD thesis) has suggested a possibility that the previous observations have missed star-forming galaxies strongly obscured by dust by showing a higher cosmic SFRD than previously reported with a 1σ significance at $1 < z < 4$ using Atacama Large Millimeter/submillimeter Array (ALMA) data. To understand the cosmic SFRD and its time evolution, SFR measurements with various wavelengths are important.

1.1.2 Star formation main sequence

It has been known that there is a correlation between stellar masses and SFRs of galaxies, which is called star formation main sequence (SFMS). It is usually fitted by a simple function in a shape of

$$\log \mathrm{SFR} = a \log M + b, \tag{1.1}$$

where $\log M$ is stellar mass of a galaxy. Measurements of previous studies have suggested that the slope a is between 0 and 1. The SFMS has been observed up to at least $z \sim 4$ and the normalization b increases toward high-z. This indicates more active star formation of galaxies in the early universe than today. At $z \sim 2$, for example, SFRs per unit stellar mass (specific star formation rate; sSFR) are typically $\sim$ 20 times higher than local values (e.g., Whitaker et al. 2012, Sobral et al. 2014).

Another important measurement is the scatter around the SFMS. It has been thought to reflect dominant mechanisms which govern evolution of galaxies on the SFMS. Tacchella et al. (2016) have suggested that observed small scatters (~ 0.3 dex) can be explained by a "self-ragulated" process, where star formation of galaxies is governed by gas inflows and depletions, rather than bursty events such as major mergers. Other studies have also shown that the evolution of sSFR can be provided by the time evolution of gas accretion rate onto the galaxies (Dutton et al. 2010, Dekel et al. 2013). Hence the galaxies on the SFMS are expected to evolve along the tight correlation until they start to be quenched at the high-mass end.

On the other hand, however, it is unclear if the SFMS holds on in the low-mass end ($\log M/M_{\odot} < 9$) due to observational limits, especially for high-z galaxies. By a cosmological hydrodinamical simulation (FIRE; Hopkins et al. 2014), Sparre et al. (2017) have found that low-mass galaxies probably show larger scatters around the SFMS than more massive ones. This is explained by stronger supernova feedbacks in the low-mass galaxies due to their shallower gravitational potentials. They have also suggested that significant bursts and suppressions of star formation occur with short timescales (~ 10 Myr) as a consequence of the feedbacks. Hence we should use a SFR indicator with an enough time sensitivity to detect the increased scatters. Hα emission line is the most suitable tracer to such short time fluctuations of star formation activity because it originates from HII regions ionized by the most massive stars. Since lifetimes of the massive stars are short (~ 10 Myr), the SFR derived from the Hα luminosity is sensitive to the short time fluctuations.

To find candidates of galaxies with the bursty star formation histories (SFHs), we can use luminosity ratios of Hα and UV. Since both luminosities reflect average SFRs over different periods (~ 10 Myr and ~ 100 Myr for Hα and UV, respectively), their ratios change as a function of time if galaxies have experienced starbursts within past 100 Myr (Sparre et al. 2017, Faisst et al. 2019, Emami et al. 2019). Indeed Faisst et al. (2019) have found a number of galaxies with high sSFRs and Hα/UV ratios at $z \sim 4.5$ using the Spitzer/IRAC photometry. Even in the local universe, Emami et al. (2019) have shown the existence of such populations. They are important populations to constrain galaxy evolution models at early phases and further investigations are

required, especially at intermediate redshift, to better understand them.

1.1.3 Equivalent width

Equivalent widths are defined with ratios between flux densities of nebula emission lines and stellar continua so that they indicate how remarkable the emission lines are in galaxies. Measurements of the equivalent widths, especially for rest-frame optical lines, have been actively performed for a long time in many works to understand their redshift evolution and connections with other properties of galaxies (e.g., Thomas et al. 2013, Lamareille et al. 2009, Stark et al. 2013, Sobral et al. 2014, Rasappu et al. 2016, Reddy et al. 2018). For example, Fumagalli et al. (2012) have measured Hα equivalent widths of galaxies at $0,8 < z < 1.5$ using grism spectroscopic data of the 3D-HST and found that low-mass galaxies tend to have higher equivalent widths than more massive ones. In addition, the emission lines become stronger at fixed stellar masses with increasing redshift. Sobral et al. (2014) have found the same trends for galaxies at redshift up to 2.23 with a larger sample obtained by a narrow-band imaging survey. Even at $z > 4$, Hα equivalent widths have been measured using the Spitzer/IRAC broad-band photometry and followed the redshift evolution (Smit et al. 2014, Rasappu et al. 2016). The increases of the equivalent widths with redshift suggest larger contributions of the emission lines in broad-band photometry of the high-z galaxies so that we should be careful when deriving their stellar masses by spectral energy distribution (SED) fitting, where the boosted fluxes lead to overestimated stellar masses.

Connections between equivalent widths of optical lines, such as [OII], Hβ, [OIII], Hα and [NII], and properties of galaxies have been thoroughly investigated by Reddy et al. (2018) for galaxies at $1.4 < z < 3.8$ using the spectroscopic data of the MOSFIRE Deep Evolution Field (MOSDEF) survey. They have found that galaxies with higher equivalent widths tend to show lower stellar masses, younger ages, and higher sSFRs. These correlations are the most significant to the [OIII] equivalent widths. In addition, ionization parameters and ionizing photon production efficiencies are also high in the highest equivalent width galaxies. Such properties have been expected for typical galaxies in the cosmic re-ionization era and they have indeed occupied the upper left

region on the BPT diagram, where the galaxies show large Lyα equivalent widths (Erb et al. 2014, Trainor et al. 2016). As a consequence, to investigate the galaxies with high [OIII] equivalent widths may enable us to understand populations which contribute to the cosmic re-ionization.

1.2 Selection of star-forming galaxies

To correctly understand star formation activities at each epoch, it is important to properly and efficiently select star-forming galaxies and investigate their properties statistically. Star-forming galaxies have been known to exhibit several features in their spectra, which have been used to identify them.

1.2.1 Nebula emission lines

Spectra of star-forming galaxies usually contain some prominent emission lines, which are originated from nebulae ionized by radiations of young stars. Hence we can detect and identify the star-forming galaxies by existences of the emission lines in their spectra. In previous studies, several emission lines, such as Lyα, Hα, [OII] and [OIII], have been often used to investigate the star-forming galaxies both at the local and high-z universe.

1.2.2 Lyman break

Strong UV continua are another characteristic of star-forming galaxies, which are mostly contributed by young stars. However, photons with wavelengths shorter than the Lyman limit (912 Å) are almost all absorbed by neutral hydrogen. As a consequence, there is a remarkable break in each of their spectra across 912 Å, which is known as the Lyman break. This feature can be used to select the star-forming galaxies. However, the UV continua are easily absorbed by interstellar dust too. Thus the star-forming galaxies identified by the Lyman breaks have been thought to be less dusty systems (e.g., Oteo et al. 2015).

1.2.3 UVJ diagram

It has been known for a long time that galaxies form two distinct populations on a optical color-magnitude diagram, which are called "red sequence" and "blue cloud". The galaxies located in the blue cloud are generally regarded as young and relatively unobscured star-forming galaxies. On the other hand, it is difficult to distinguish types of the red sequence galaxies because ages and dust extinctions can similarly redden the optical colors so that dusty star-forming galaxies and old quiescent galaxies can occupy the same places on the color-magnitude diagram. This degeneracy makes proper selections of the star-forming galaxies challenging when single optical colors are used.

During the past decade, a new technique has been developed and used to break the degeneracy and distinguish the dusty star-forming and the quiescent galaxies without spectroscopic information, which uses a rest-frame optical-to-near-infrared color in combination with an optical color. Wuyts et al. (2007) have investigated how galaxy properties derived from SED fitting are related to their locations on a color-color diagram of rest-frame $(U-V)$ and $(V-J)$ (UVJ diagram) using galaxies at redshift up to 3.5. They have shown that the $(V-J)$ distributions of the galaxies with a fixed $(U-V)$ has been broad and that there has been too red $(V-J)$ populations which cannot be explained by dust-free stellar population synthesis models with any SFHs. They have also found that the galaxies with such red $(V-J)$ colors have had younger ages and been strongly attenuated by dust according to the SED fitting while those with bluer $(V-J)$ colors have been older and less obscured. With consistency between A_V values from the SED fitting and the Spitzer/MIPS 24 μm band fluxes, they have concluded that the UVJ diagram effectively separate the star-forming and the quiescent populations with breaking the degeneracy of the reddening.

The bimodality of the star-forming and the quiescent populations on the UVJ diagram persists at least up to $z \sim 2.5$ (Williams et al. 2009, Whitaker et al. 2011). Williams et al. (2009) have investigated if the locations occupied by the two populations on the UVJ diagram vary with redshift and found some trends. First, the $(U-V)$ colors of the quiecent galaxies become bluer with increasing redshift, while their $(V-J)$

colors do not change. This reflects passive evolution of their stellar populations, where the $(U - V)$ colors are getting redder due to age increases. Second, the number fraction of the dusty star-forming galaxies increases toward high-z. Moreover, high-z dusty star-forming galaxies tend to have redder $(V - J)$ colors than those at lower redshift. These results indicate active star formation activities in the high-z universe.

Based on such findings, several previous works have defined criteria to separate the two populations by the colors. However, these criteria are not perfect due to intrinsic scatters of the rest-frame colors and uncertainties of photometric redshifts.

1.3 SFR indicators

One of fundamental properties to characterize star-forming galaxies is SFR. SFRs of galaxies have mainly been estimated from luminosities at various wavelengths, which are thought to be emitted as a consequence of star formation. Since different SFR indicators have different origins, they respond variations of star formation activities with different timescales. In this section, we summarize SFR indicators which have been often used. Descriptions of individual indicators below are mainly based on Kennicutt (1998) and Kennicutt & Evans (2012).

1.3.1 UV continuum

UV continua between 1216–3000 Å are dominated by young stellar populations so they linearly trace SFRs. They have been used in many studies about distant galaxies as they shift to the visible region due to redshift.

The main contributors to the UV continua of the galaxies are stars with masses above $\sim 5\ M_{\odot}$, whose lifetimes are typically less than 100 Myr. Thus the UV continua are indicators of SFRs averaged over past ~ 100 Myr.

The emissions in this wavelength range are easily absorbed by interstellar dust. Hence considering the dust attenuation is important when using the UV SFRs.

1.3.2 Hα emission line

Ionizing photons emitted by massive stars, whose wavelengths are shorter than 912 Å, are almost completely absorbed by the surrounding neutral hydrogen. Their energy is then re-emitted as recombination lines such as Lyα, Hα, Paα, and higher-order lines. Since only massive and young stars emit the ionizing photons, the recombination lines are closely related to SFRs. Especially, Hα has been used for a long time because it is a rest-frame optical (6563 Å) line and strong enough to be detected easily.

Fluxes of the ionizing photons are dominated by the most massive ($> 10\ M_{\odot}$) stars with very short lifetimes less than 10 Myr. Thus Hα SFRs trace nearly instantaneous star formation. Although its wavelength is longer than the UV continuum, it is still important to take the dust attenuation into account.

1.3.3 [OII]$\lambda\lambda 3726, 3729$ doublet

The [OII]λ3727 forbidden-line doublet also has been used as a SFR indicator. Main advantage of the use of [OII] is its detectability in the observed-frame optical wavelength range for high-z galaxies, where Hα falls into the near-infrared (NIR) region. Though [OII] luminosities generally correlate with Hα luminosities, the [OII] SFRs are more uncertain than the other indicators because of their dependence on the abundance and ionization state of the gas.

1.4 Observation types

There are great numbers of telescopes and instruments aiming to take spectral information on galaxies at rest-frame optical and NIR wavelengths. Although each instrument has its own unique capabilities, there are two fundamental types of observations, namely imaging and spectroscopy. Here we introduce both advantages and shortcomings of each observation type in the context of extragalactic studies. Table 1.1 summarizes principal information of current surveys targeting Hα emission lines of galaxies.

1.4.1 Imaging

Imaging observations have been usually performed using filters with specific passbands. One of its advantages is a capability of observing many galaxies at once in combination with field of views (FoVs) of the telescopes and instruments. The imaging observations also enable us to obtain spatial information such as sizes of the galaxies and their morphologies.

The filters used for the imaging have been divided into two categories, namely broad-band and narrow-band, based on their bandwidths. Imaging surveys with various broad-band filters covering wide wavelength ranges enable us to perform the SED fitting, where observed data points are fitted by stellar population synthesis (SPS) models, to derive properties of the galaxies. However, due to their wide bandwidths, precise information on spectra such as the emission and/or absorption lines is lost.

On the other hand, observations with narrow-band filters enable us to derive the emission line fluxes without spectroscopy. The narrow-band filters are designed to have passbands which correspond to wavelengths of specific emission lines at specific redshifts. Hence the use of the narrow-band filters makes it easier to identify star-forming galaxies and measure their emission line strengths at specific epochs. However, the narrow-band imaging surveys need much time than the broad-band imaging surveys to achieve a certain searching volume because of their narrow redshift windows.

1.4.2 Spectroscopy

Spectroscopy enables us to investigate precise information on spectra of galaxies, which leads to accurate flux measurements. Spectroscopic observations with ground-based facilities have generally been performed using slit masks which are designed by aligning one or several long slits on the target objects. The long slits make accurate measurements possible by minimizing background sky contributions and avoiding overlaps of the target spectra. However, because of limited widths of the slits, which are usually comparable to seeing sizes, the long-slit spectroscopy may miss lights from outskirts of the galaxies. In addition, it takes much longer time to construct large samples by spectroscopic surveys compared to the imaging ones.

Recently a new technique is becoming popular, which is called integral-field spectroscopy (IFS). The IFS makes it possible to obtain both spatial and spectral informations simultaneously, which results in better understandings of kinematics and precise physics in the galaxies. Nevertheless, the IFS still requires the large amount of time as well as the long-slit spectroscopy to construct large samples.

Table 1.1: Summary of recent surveys

Survey	Type	Redshift[1]	FoV (deg^2)	Volume ($10^5 cMpc^3$)
Villar et al. (2008)	NB imaging	$0.830 < z < 0.845$	0.1738	0.1773
New Hα Survey (Lee et al. 2012)	NB imaging	$0.804 < z < 0.825$	0.82	0.912
		$2.182 < z < 2.214$	0.0353	0.136
HiZELS (Geach et al. 2008)	NB imaging	$0.391 < z < 0.411$	1.68	0.88
		$0.830 < z < 0.860$	1.30	1.9
		$1.450 < z < 1.482$	2.24	7.4
		$2.214 < z < 2.260$	2.06	7.7

1.5 Aim of this thesis

The aim of this thesis is to verify a method to derive emission line fluxes from broad-/medium-band photometry at $z = 2.1$–2.5 using a multi-band photometry catalog of the Fourstar Galaxy Evolution Survey (ZFOURGE; Straatman et al. 2016). As mentioned above, both constructing large samples and measuring emission line fluxes are important to understand statistical properties of star-forming galaxies, which has been a trade-off so far. If we can extract the emission line fluxes from the broad-band photometry, it becomes an efficient way to construct large samples of star-forming galaxies at the epoch of the most active star formation. Similar concepts have been verified at $z > 4$ in previous studies (e.g., Smit et al. 2014, 2015, Stark et al. 2013, Schaerer & de Barros 2009, Faisst et al. 2016, 2019) with the Spitzer/IRAC. We apply

our method to Hα emitters and [OIII] emitters at $z = 2.1$–2.5 and investigate their properties.

The structure of this thesis is as follows. In Chapter 2, we describe our data and method, where continuum estimates by the SED fitting are important to derive emission line fluxes. Then we investigate properties of the Hα emitters at $2.1 < z < 2.5$ selected by our method in Chapter 3. Thanks to the multi-band photometric data, we can correct them for the dust attenuation in more reasonable way than in previous narrow-band imaging surveys. In Chapter 4, we also apply our method to derive [OIII] emission line fluxes of the galaxies at the same redshift and compare the [OIII] emitters with the Hα emitters to understand what differentiate the two populations. Finally we summarize our result in Chapter 5 and present proposals for future observations to further investigate the galaxies with extreme properties.

Throughout this thesis, we adopt the AB magnitude system and a cosmology with $H_0 = 70$ km s^{-1} Mpc^{-1}, $\Omega_{\rm m} = 0.3$, and $\Omega_\Lambda = 0.7$.

[1]The redshift of Hα corresponding to the wavelength range of each survey

Chapter 2

Data and method

In this chapter we describe the data used in this thesis and our method to extract emission line fluxes from broad-band photometry.

2.1 ZFOURGE catalog

We use a photometric catalog of the FourStar galaxy evolution survey (ZFOURGE; Straatman et al. 2016) for our analysis. Table 2.1 is a summary of the catalog.

Observations of the ZFOURGE were conducted over 45 nights with the FourStar near-infrared camera on the Magellan telescope (Persson et al. 2013), targeting three legacy survey fields: COSMOS (Scoville et al. 2007), UDS (Lawrence et al. 2007), and CDFS (Giacconi et al. 2002). The survey area is ~ 407 arcmin^2 in total. Since many ground-based and space observations have been conducted in these fields, there are much public data available so that the catalog covers from 0.8–8 μm with 26–40 filters. Such the large number of the data points makes it possible to accurately derive properties of galaxies by SED fitting. Especially, photometry of the Spitzer/IRAC at 8.0 μm band is important to estimate stellar masses of the galaxies by putting good constraints on rest-frame near-infrared (NIR) regimes of the SEDs. In addition, the Spitzer/MIPS 24 μm band data is available for all of the fields, which is essential to estimate infrared bolometric luminosities and derive infrared SFRs (see § 2.4.2).

A big advantage of the ZFOURGE is the very deep K_s-band imaging, whose 5σ limiting magnitude is ≥ 25.5 across the fields. As a result, Straatman et al. (2016)

have found that 80% completeness has been achieved for galaxies with $\log M \sim 9.0$ at $z = 2$.

Another unique characteristic of the ZFOURGE survey is its medium-band filters dividing J and H-bands into three (J_1, J_2, J_3) and two (H_s, H_l), respectively. When determining redshifts of galaxies using photometric data, it is important to sample spectral features straddling a pair of adjacent filters. Balmer break (3636 Å) and 4000 Å break have been often used for such purposes and they shift to the NIR region at $z \gtrsim 1.5$. The medium-band filters of the ZFOURGE are optimal to sample the breaks of galaxies at $1.5 \lesssim z \lesssim 3.5$ and improve photo-z accuracies in this redshift range. Straatman et al. (2016) have derived photo-zs from SED fitting by the EAZY (Brammer et al. 2008) and compared them with publicly available spectroscopic redshifts (Skelton et al. 2014, Kriek et al. 2009, Tasca et al. 2017). They have used $\sigma_z \equiv 1.48 \times |z_\mathrm{phot} - z_\mathrm{spec}|/(1 + z_\mathrm{spec})$ to quantify errors in the photo-zs, where z_phot and z_spec are the photometric and spectroscopic redshifts, respectively, and found $\sigma_z \sim 0.013$–0.022 in the three fields.

The catalog provides information on the data quality of each object as use flags, which are determined according to signal-to-noise ratios (S/N), star/galaxy classifications, and depths of images at the object locations. In this thesis, we include only galaxies with good quality (use flag=1) in our analysis.

Table 2.1: Summary of ZFOURGE catalog

field	COSMOS	UDS	CDFS
area (arcmin^2)	139.2	135.6	132.2
Ks depth (AB mag,5σ)	25.5	25.7	26.2–26.5
# of filter	38	27	43
coverage (μm)	0.8–8, 24	0.8–8, 24	0.8–8, 24, 100, 160
σ_z	0.022	0.013	0.020

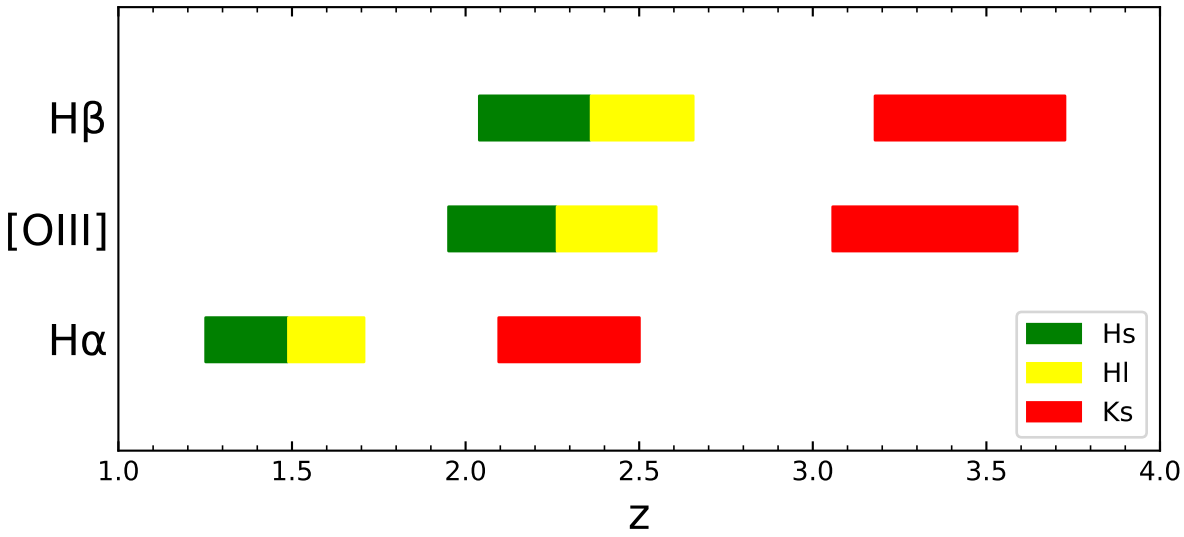

Figure 2.1: Combinations of the emission lines and the filters at each redshift. At $z > 1$, Hα, Hβ, and [OIII] emission lines are observed in the NIR regime. Especially, at $2.1 < z < 2.5$, Hα falls into the $K_{\rm s}$ broad-band filter of the ZFOURGE, while Hβ and [OIII] are simultaneously observed in the H medium-band filters.

2.2 Emitter selection by flux excess

Hα emission lines (rest-frame 6563 Å) of galaxies at $2.1 < z < 2.5$ fall into the $K_{\rm s}$-band of the ZFOURGE, while [OIII] (rest-frame 4959 & 5007 Å) and Hβ (rest-frame 4861 Å) emission lines are shifted into the two medium-bands ($H_{\rm s}$ and $H_{\rm l}$) as shown in Figure 2.1.

To select emitters, we define "flux excess" (in units of erg s^{-1} cm^{-2} Å^{-1}) as a difference between an observed flux and a continuum flux in a broad-band filter as follows:

$$f_{\rm excess} = f_{\rm obs} - f_{\rm cont}. \tag{2.1}$$

This is the total flux of all emission lines in the filter and expected to be zero when no emission line falls into the filter. The continuum flux is estimated by SED fitting, where contributions of the emission lines must be taken into account as described in 2.2.1. The extractions of the emission line fluxes from the flux excesses are more robust against model assumptions than estimates from only the SED fitting (2.2.2).

2.2.1 SED fitting with emission line templates

SEDs are fitted by spectral templates based on stellar population synthesis models to derive properties of galaxies such as stellar masses, amounts of dust attenuation, metallicities, and ages.

When redshifted emission lines fall into certain filters, fluxes observed in the filters are boosted by the lines. Hence the SED fitting can overestimate continuum fluxes of the galaxies unless the effect of the emission liens is properly taken into account. This is important especially for high-z galaxies because they have been known to show larger equivalent widths compared to those in the local universe (Stark et al. 2013, Salmon et al. 2015, Forrest et al. 2018). Figure 2.2 shows examples of the galaxies having clear flux excesses, where the left panels show their RGB images based on the fluxes in the $K_{\rm s}$, $H_{\rm l}$, and $H_{\rm s}$-band, respectively. Their best-fit SEDs in the right panels make it clear that each object has significant flux excess.

In this thesis, we run the Fitting and Assessment of Synthetic Templates (FAST; Kriek et al. 2009) with templates including emission lines to accurately estimate continuum fluxes of galaxies. These templates were created by Spitler (private communication), who injected emission line fluxes into the Bruzual & Charlot (2003) templates following the technique of Salmon et al. (2015). Table 2.3 summarizes the model and parameters used here. The emission lines are added to the templates following Salmon et al. (2015) using emission-line strengths calculated by Inoue (2011) via CLOUDY 08.00 (Ferland et al. 1998). Briefly, Inoue (2011) has generated sets of relative strengths to Hβ for emission lines from Lyα to 1 μm varying ionization parameters, metallicities, and densities of hydrogen (Table 2.2).

On the other hand, a Hβ luminosity is calculated from an escape fraction and a production rate of the Lyman continuum photons (Eq. 1 in Salmon et al. 2015). Since the production rate of the Lyman continuum photons depends on ages of stellar populations, it is calculated for each Bruzual & Charlot (2003) model template based on each age. Regarding the escape fraction of the Lyman continuum photons, there is no consensus on its value and redshift dependency. Salmon et al. (2015) have provided calculations for two extreme cases, $f_{\rm esc} = 0$ and $f_{\rm esc} = 1$. We adopt $f_{\rm esc} = 0$, where

Table 2.2: Relative line strengths of Inoue (2011) at solar metallicity

Line	Relative strength
Hβ	1
[NII]λ6548	0.09031
Hα	3.093
[NII]λ6584	0.2665
[SII]λ6716	0.1153
[SII]λ6731	0.08187

all the Lyman continuum photons are absorbed and their energy is converted to the emission lines, to be consistent with a result obtained for Lyman break galaxies (LBGs) at $z \sim 3$ (Nestor et al. 2011).

Table 2.3: FAST parameter setting

Parameter	Used value
SPS model	Bruzual & Charlot (2003) with emission lines
SFH	Delayed tau
IMF	Chabrier (2003)
Dust law	Kriek & Conroy (2013)
Metallicity	Solar ($Z_{\odot}$)

Figure 2.3 shows several comparisons of the best-fit SEDs obtained with and without the emission line templates (blue and orange, respectively). These clearly show

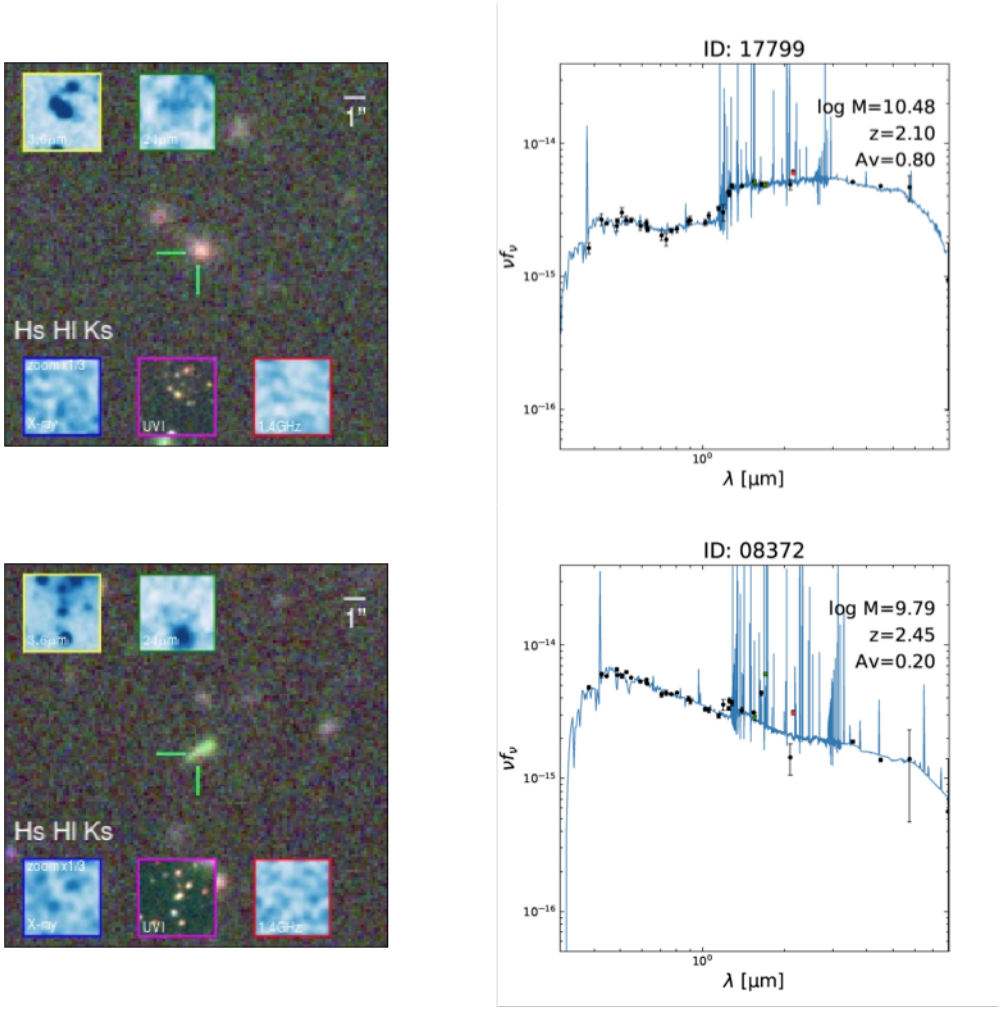

Figure 2.2: Examples of galaxies showing the flux excesses in the K_s-band (Top) and H_s/H_l-band (Bottom). The left panels are RGB images based on their fluxes in the H_s, H_l, and K_s-band, which are from the ZFOURGE website (http://zfourge.tamu.edu). Their red and green colors illustrate the flux excesses in the K_s and H_l-band, respectively. The right panels show the best-fit SEDs of each object, where photometry points of the K_s-band and the H_s/H_l-band are shown in red and green, respectively. It can be seen clearly that there are the flux excesses in both filters.

that the continuum levels, which are mainly constrained by the Spitzer/IRAC photometry, can be significantly overestimated resulting in the overestimated stellar masses by at most ~ 0.8 dex.

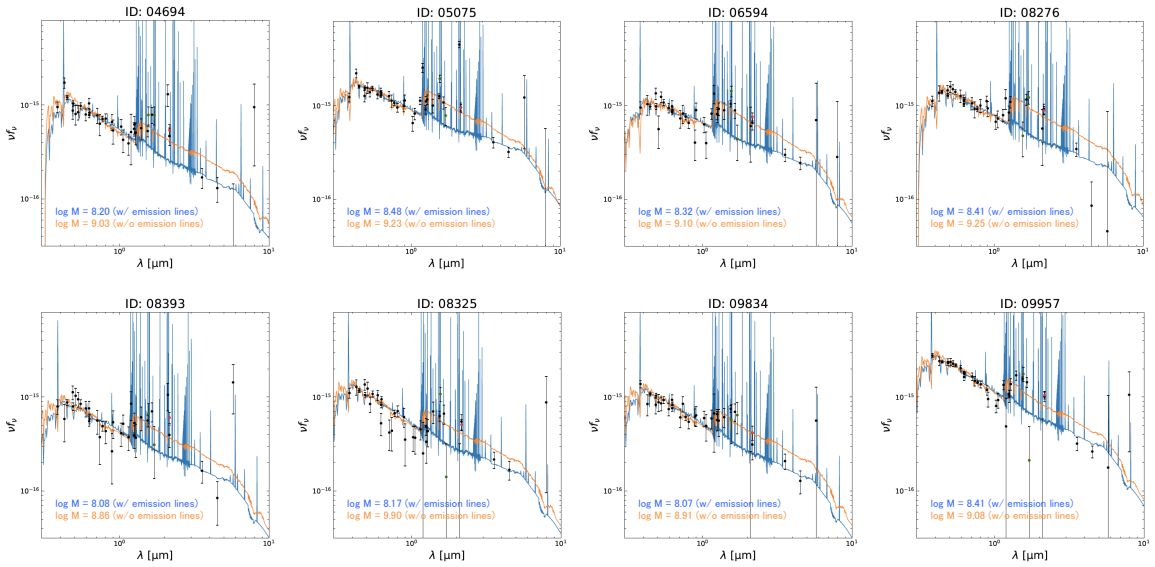

Figure 2.3: Examples of the best-fit SEDs with (Blue) and without (Orange) the emission line templates. The Spitzer/IRAC photometry at 3.6 and 4.5 μm bands, which sample rest-frame ~ 2 μm, can not be fitted well unless the effects of the emission lines are taken into account. The estimated stellar masses can be differ at most ~ 0.8 dex.

2.2.2 Robustness of the flux excess

The SED fitting described above allows us to derive not only the continuum levels but also the emission line strengths of the galaxies. However, the line strengths in the templates strongly depend on model assumptions. Equation 2.2 is the definition of the Hβ luminosity in the SED templates of Salmon et al. (2015).

$$L_{\mathrm{H}\beta} = 4.78 \times 10^{-13} \frac{1 - f_{\mathrm{esc}}}{1 + 0.6 f_{\mathrm{esc}}} N_{\mathrm{lyc}}, \tag{2.2}$$

where f_{esc} and N_{lyc} represent the escape fraction and the production rate of the Lyman continuum photons in a galaxy, respectively. Since their correct values are controversial and may vary among galaxies, the line strengths determined by the templates have uncertainties.

On the other hand, the continuum fluxes estimated by the SED fitting are more robust against the model assumptions. Figure 2.4 shows changes of the continuum fluxes when the production rate of the Lyman continuum photons is doubled. We find a typical difference of $\lesssim 10\%$ between the continuum fluxes derived with the different

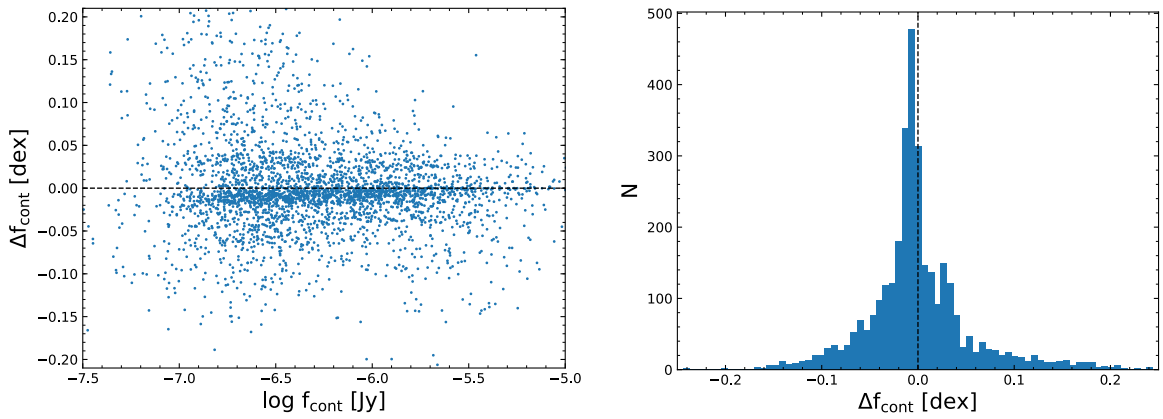

Figure 2.4: (Left): Changes of the estimated continuum fluxes when assuming a doubled production rate of the Lyman continuum photons. (Right): The distribution of the continuum offsets between the two models.

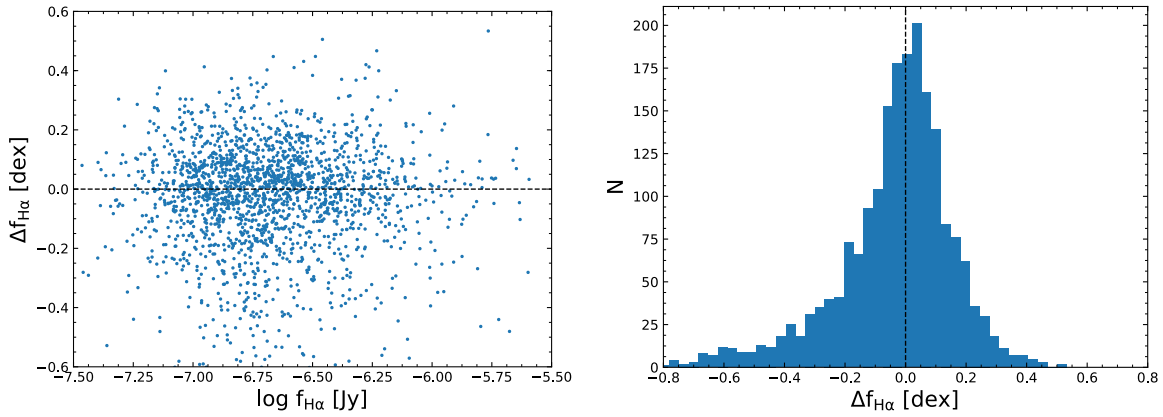

Figure 2.5: (Left): Offsets of the Hα fluxes derived from the best-fit SEDs and the flux excesses. (Right): The distribution of the offsets.

assumptions. Therefore the emission line fluxes derived from the flux excesses are more reliable than those derived from only the SED fitting. In our sample, a typical difference of Hα fluxes is $\sim 40\%$ between the two derivations as shown in Figure 2.5

2.2.3 Selection of Hα emitter candidates at $z = 2.1$–2.5

We select candidates of Hα emitters at $z = 2.1$–2.5 by requiring the flux excesses in the K_s-band to be twice larger than its photometric errors. This selection results in

2005 Hα emitters (699, 632, and 674 in COSMOS, UDS, and CDFS, respectively).

Hα fluxes (in units of erg s^{-1} cm^{-2}) of our sample are derived from the flux excesses as follows:

$$f_{\mathrm{H}\alpha} = r_{\mathrm{H}\alpha} \times f_{\mathrm{excess}} \times \Delta\lambda, \tag{2.3}$$

where $r_{\mathrm{H}\alpha}$ is a ratio of Hα to total strengths of all emission lines in the Ks-band, while $\Delta\lambda$ is its bandwidth. The Hα ratios can be calculated from the line-strengths table used in § 2.2.1. We determine which lines fall into the Ks-band based on the photo-zs of individual galaxies and find a median value of $r_{\mathrm{H}\alpha} \sim 0.79$ assuming the solar metallicity ($Z = Z_{\odot}$). The rest of the flux excesses are contributed mainly from [NII] and [SII] doublets.

To evaluate an impact of metallicity assumptions, we also calculate the $r_{\mathrm{H}\alpha}$ with the line-strength tables obtained for different metallicities. We find that the Hα ratio is almost constant in a range from $0.20Z_{\odot}$ to $Z_{\odot}$. Although it increases up to $r_{\mathrm{H}\alpha} \sim 0.9$ for an extreme case, $Z = 0.02Z_{\odot}$, the effect of metallicity is still insignificant.

2.2.4 Selection of [OIII] emitter candidates at $z = 2.1$–2.5

We also select galaxies showing the flux excesses in either the H_{s} or the Hl-band, which are candidates of [OIII](+Hβ) emitters. By applying a threshold to the flux excesses in the same manner as we have done in § 2.2.3, 623 and 841 emitters are selected by the flux excesses in the H_{s} and H_{l}-bands, respectively. In total 1464 galaxies consist of our [OIII] emitter sample.

It has been known that the ratio between [OIII]λ5007 and Hβ ([OIII]λ5007/Hβ) varies from 1 to 10 for typical star-forming galaxies at $z \sim 2.3$ while the [NII]/Hα is at most ~ 0.3 (Steidel et al. 2014). Hence it is very important to estimate contributions of Hβ to extract [OIII]λ5007 fluxes from the excesses. We estimate the Hβ fluxes of our emitters based on their Hα fluxes so that the [OIII] flux measurement is done only for the galaxies also selected as the Hα emitters in § 2.2.3. The intrinsic ratio between Hα and Hβ is 2.8 when assuming the case B recombination, an electron temperature of 10^4 K and an electron density of 10^4 cm^{-3} (Tziamtzis et al. 2011). Therefore we can calculate intrinsic Hβ fluxes (luminosities) from intrinsic Hα fluxes (luminosities) as

follows, assuming the intrinsic Hα/Hβ is 2.8:

$$f_{\mathrm{H}\alpha,\mathrm{int}} = 2.8 \times f_{\mathrm{H}\beta,\mathrm{int}} \tag{2.4}$$

$$\Leftrightarrow 10^{0.4A_{\mathrm{H}\alpha}} \times f_{\mathrm{H}\alpha,\mathrm{obs}} = 2.8 \times 10^{0.4A_{\mathrm{H}\beta}} \times f_{\mathrm{H}\beta,\mathrm{obs}} \tag{2.5}$$

$$\Leftrightarrow f_{\mathrm{H}\beta,\mathrm{obs}} = \frac{1}{2.8} \times 10^{0.4(\mathrm{A}_{\mathrm{H}\alpha}-\mathrm{A}_{\mathrm{H}\beta})} \times f_{\mathrm{H}\alpha,\mathrm{obs}}, \tag{2.6}$$

where $f_{\mathrm{H}\alpha,\mathrm{int}}$ and $f_{\mathrm{H}\beta,\mathrm{int}}$ are the intrinsic fluxes of Hα and Hβ emission liens while $f_{\mathrm{H}\alpha,\mathrm{obs}}$ and $f_{\mathrm{H}\beta,\mathrm{obs}}$ are the observed fluxes attenuated by dust, respectively. $\mathrm{A}_{\mathrm{H}\alpha}$ and $\mathrm{A}_{\mathrm{H}\beta}$ represent the amounts of the dust attenuation against Hα and Hβ, respectively. See § 2.4.3 for details of our correction for the dust attenuation. By subtracting the $f_{\mathrm{H}\beta,\mathrm{obs}}$ from the flux excess, we obtain the [OIII] flux, where contributions from other emission lines are assumed to be zero. Finally we obtain the [OIII]λ5007 flux using the intrinsic ratio of [OIII]λ5007/[OIII]λ4959 = 2.97.

2.3 Flux comparisons with other methods

In this section, we compare the Hα fluxes derived in § 2.2.3 with those obtained by different methods in order to verify the reliability of our method.

2.3.1 Narrow-band imaging

The ZOFURGE catalog contains photometry of the NB209 filter, which has been used in the New Hα survey (Lee et al. 2012), for galaxies in COSMOS and CDFS. The NB209 filter has been designed to have a central wavelength of 20,987 Å and a FWHM of 208 Å to detect Hα from galaxies at $z = 2.2$.

To check the consistency of our method with a conventional narrow-band emitter selection, we derive the Hα fluxes from $(K_{\mathrm{s}} - NB209)$ color excesses and compare them with those derived from the K_{s}-band excesses. Our selection procedure follows general techniques often used in narrow-band surveys (e.g., Sobral et al. 2009, Lee et al. 2012). First we apply a S/N>5 threshold to the NB209 detection. Then we require the emitter candidates to have $(K_{\mathrm{s}} - NB209)$ color excesses with a $> 3\Sigma$ significance compared to random scatters due to photometric errors, where the Σ is defined following

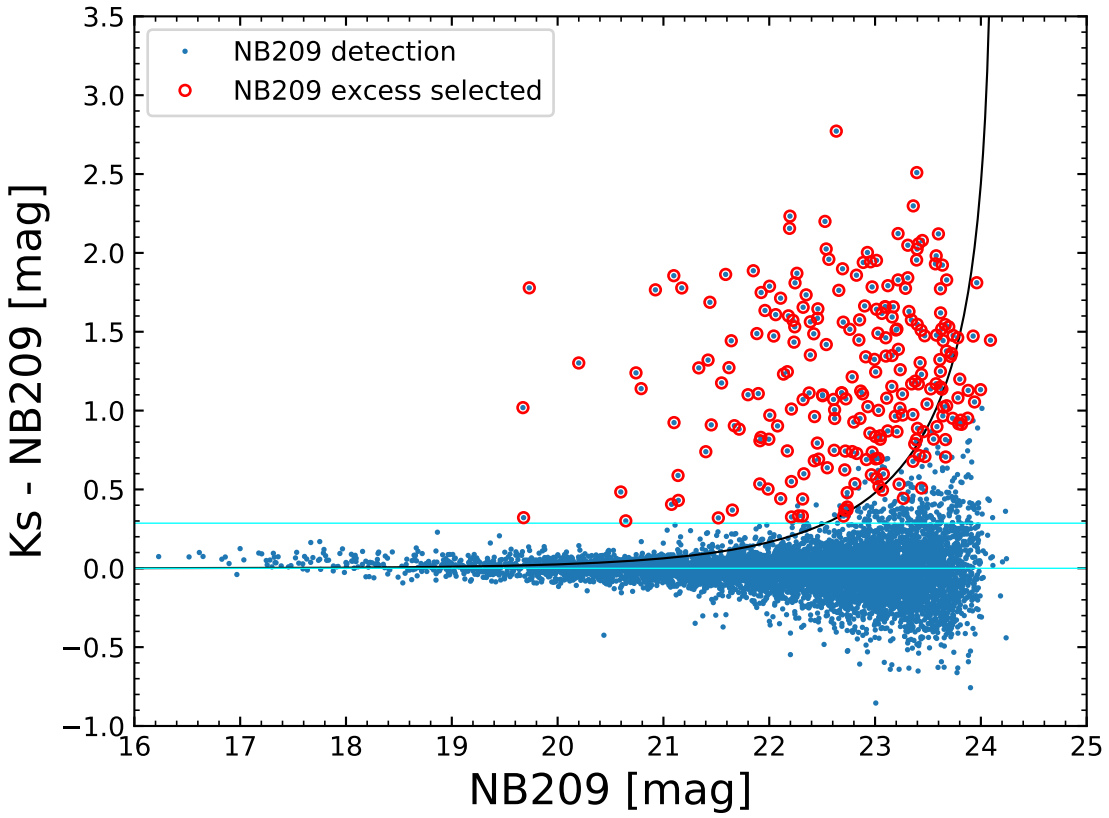

Figure 2.6: Color-magnitude diagram of the K_s and the NB209. The blue filled circles represent individual galaxies detected in the NB209 with S/N>5. The upper cyan line shows the lower limit of the color excess corresponding to the equivalent width of ~ 20 Å. The black solid curve represents the median value of the 3Σ significance from the photometric errors. The red open circles indicate the Hα emitter candidates.

Sobral et al. (2009). Finally we set another threshold of $(K_s - NB209) > 0.29$ to avoid contaminations from the random scatters of continuum objects, which corresponds to an equivalent width of $\sim$ 20Å. As a result, 237 galaxies are selected as the emitter candidates (Figure 2.6). However a part of their color excesses may be due to other emission lines than Hα at different redshifts. Therefore we select the candidates of the Hα emitters at $2.1 < z < 2.5$ based on their photometric redshifts, which results in 73 Hα emitters.

Figure 2.7 shows a fraction of the narrow-band selected Hα emitters which are also selected by our method based on the K_s-band excesses. We find 86% (63/73) of the

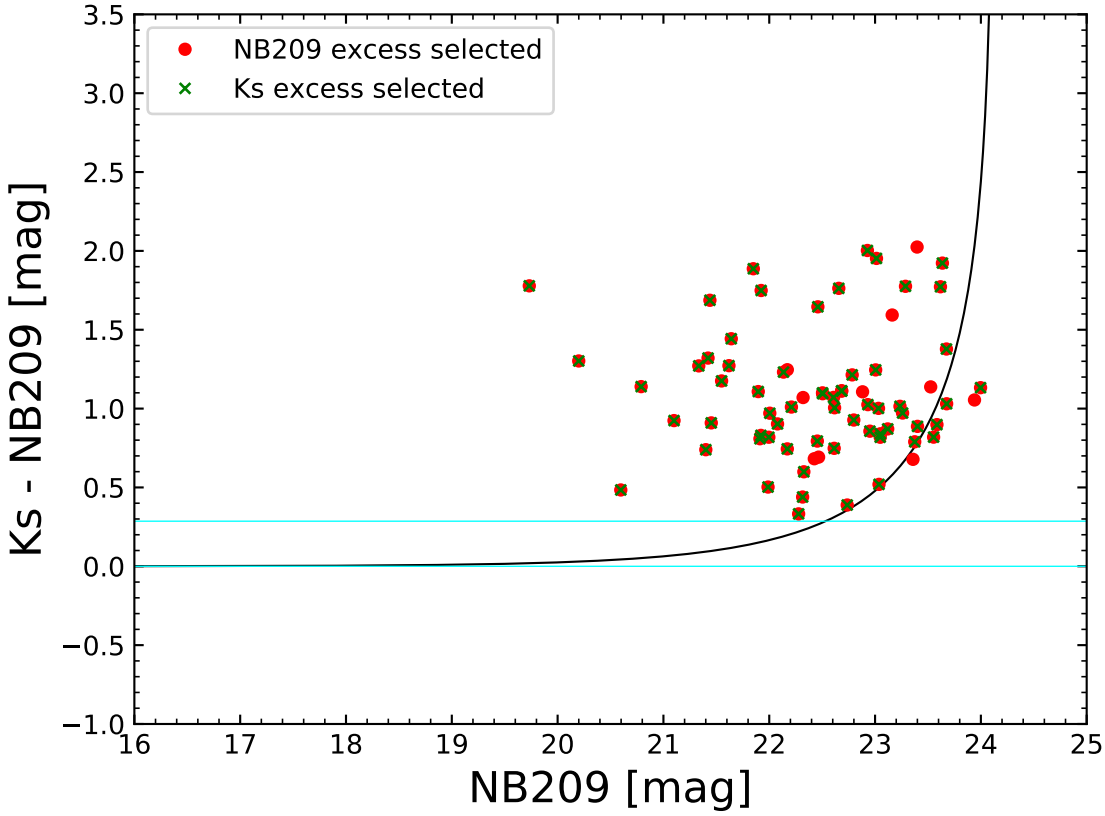

Figure 2.7: Same as Figure 2.6, but only for the emitter candidates. The red circles and green crosses represent the emitters selected from the NB209 color excesses and the flux excesses in the K_s-band, respectively.

narrow-band selected galaxies are also selected by our method. Moreover this fraction does not depend on the amount of the color excess. This suggests that our method can reproduce most of the narrow-band selected sample regardless of their equivalent widths.

We also compare the Hα fluxes derived from both the narrow-band color excesses and the K_s-band excesses as shown in Figure 2.8. We find that 46/63 (73%) of the Hα emitters have consistent values within a factor of 2 in both methods. The scatter around the one-to-one relation is 0.16 dex. Although some outliers from the one-to-one relation exist, there is no clear trend with their stellar masses.

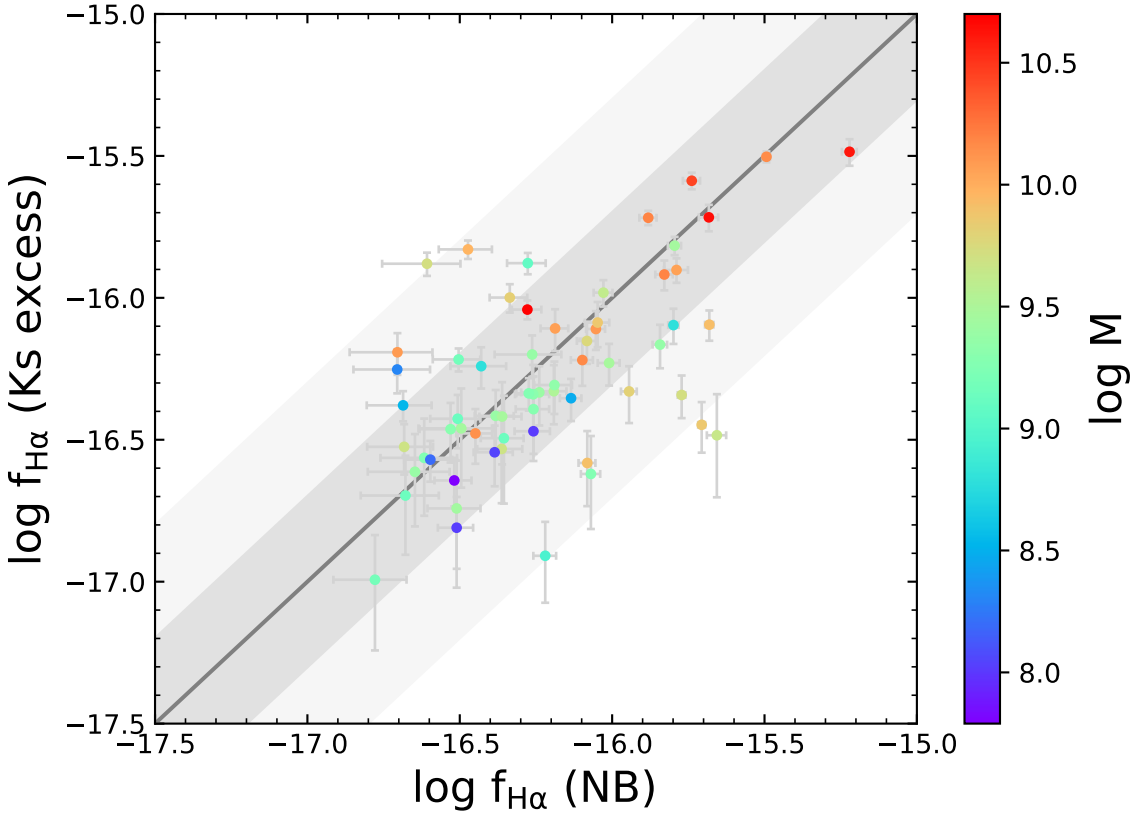

Figure 2.8: Comparison between the Hα fluxes derived from the NB209 color excesses and the flux excesses in the K_s-band. Both axes are in the units of erg s^{-1} cm^{-2}. The grey line shows the one-to-one relation while the regions shaded in grey and light-grey indicate factor 2 and 5 intervals, respectively. The color coding of individual galaxies corresponds to their stellar masses.

2.3.2 Long-slit spectroscopy

Some of the ZFOURGE galaxies have been observed by a follow-up spectroscopic survey, ZFIRE (Nanayakkara et al. 2016). Observations of the ZFIRE were performed with the Keck/MOSFIRE, which has a capability of multi-object spectroscopy sampling 0.97–2.41 μm with $R \sim 3500$. Its 2σ spectroscopic continuum detection limit is $K_s \simeq 24.1$ (0.05×10^{-17} erg s^{-1} cm^{-2} Å^{-1}) in COSMOS. The primary targets of the ZFIRE are star-forming galaxies at $2.0 < z < 2.2$, which are selected based on the photometric redshifts of the ZFOURGE, to detect their Hα, [NII], Hβ, and [OIII] emission lines for investigating ISM conditions, IMFs, kinematics, and cluster properties at $z \sim 2$.

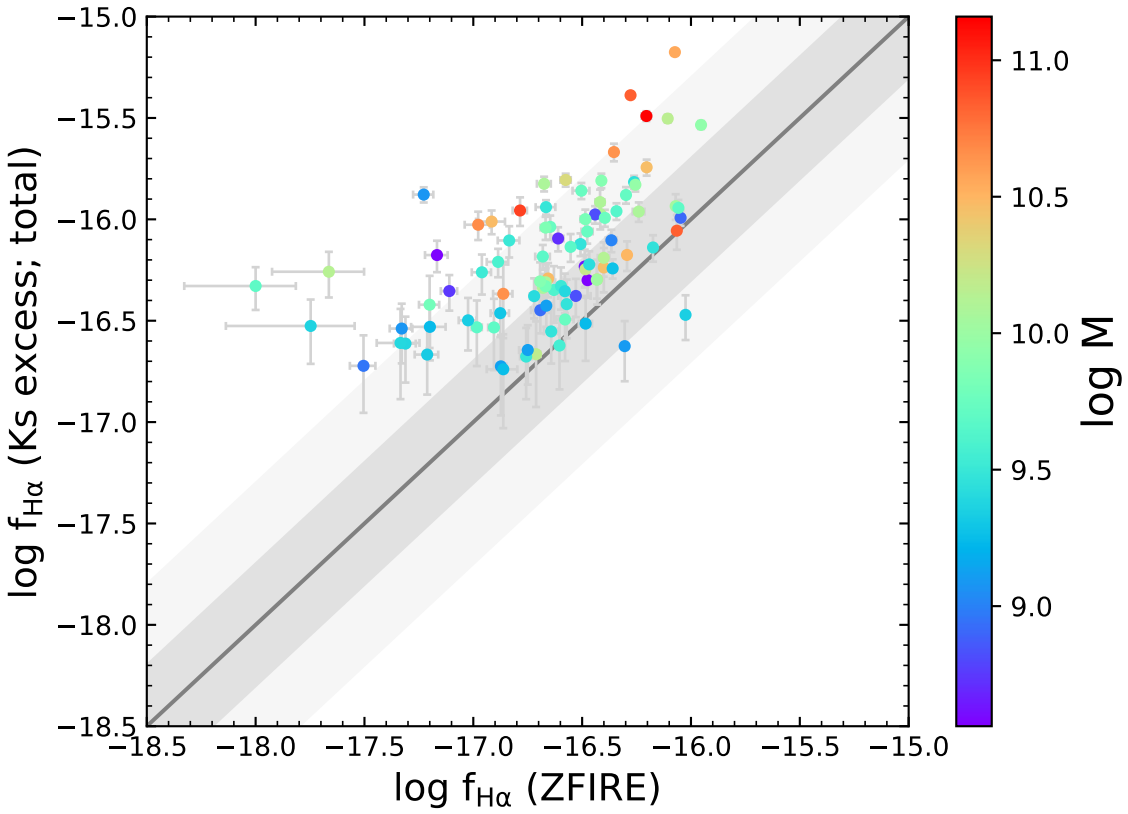

Figure 2.9: Same as Figure 2.8, but for the ZFIRE and our method, where the K_s excesses are derived using the aperture corrected photometry.

In our sample, 93 Hα emitters in COSMOS have been observed in the ZFIRE. Figure 2.9 shows a comparison of the Hα fluxes between our method and the ZFIRE. We find that our values are higher than those of the ZFIRE with a median offset of 0.42 dex. A possible cause of the systematic offset is a difference in aperture sizes between the ZFOURGE and the ZFIRE. According to Nanayakkara et al. (2016), the slit size used in the ZFIRE is 0".7 × 2".8. On the other hand, the K_s-band photometry of the ZFOURGE was taken with a 1".2 aperture and aperture corrections were applied to account for lights from outskirts of the galaxies (see § 2.1). Therefore, the ZFIRE might have missed larger fractions of the Hα fluxes than the ZFOURGE with the aperture corrections. Indeed, both Hα fluxes agree well when we use the data without

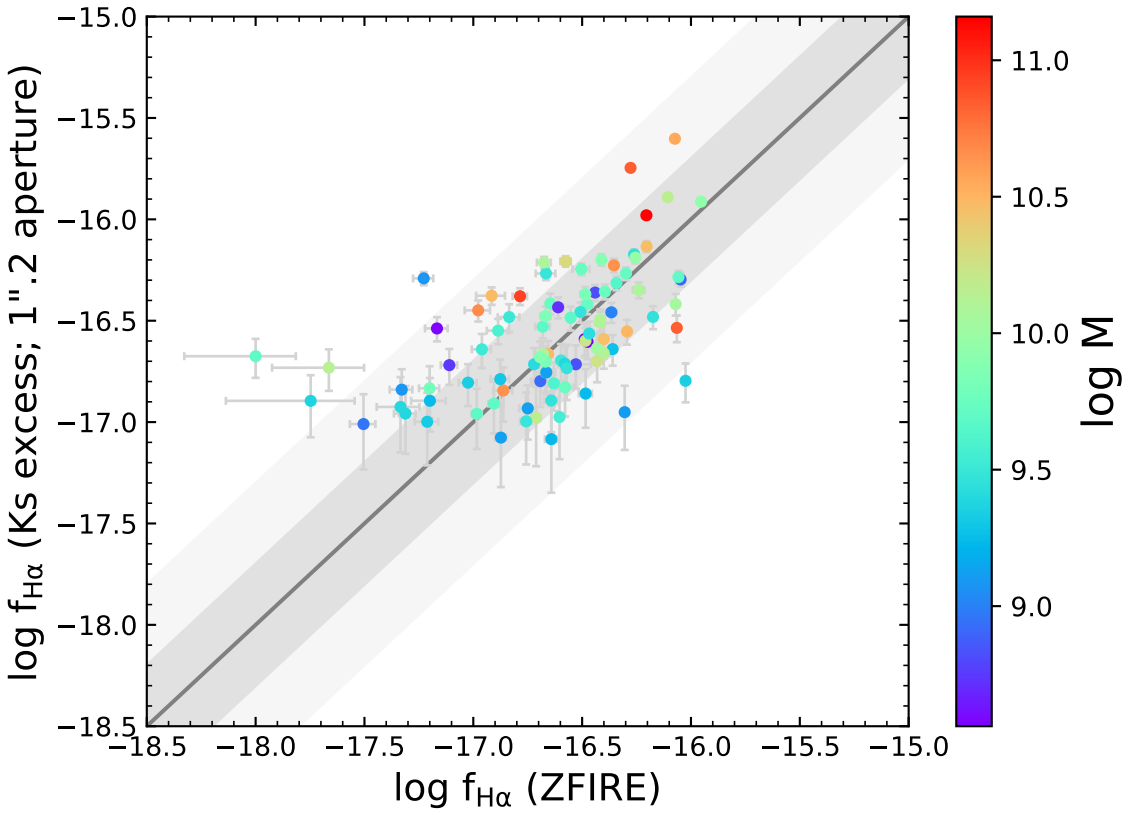

Figure 2.10: Same as Figure 2.8, but for the ZFIRE and our method, where the K_s-band excesses are derived using the 1″.2 aperture photometry.

the aperture corrections as shown in Figure 2.10. We find that 62/93 (67%) of the Hα emitters have consistent fluxes in both methods within a factor of 2. The scatter around the one-to-one relation is 0.21 dex.

2.3.3 Integral-field spectroscopy

We also compare our fluxes with the integral field spectroscopic (IFS) data taken by KMOS^{3D} survey (Wisnioski et al. 2019). It has been conducted with the VLT/KMOS to detect emission lines, such as Hα, [NII] and [SII], of galaxies at redshifts from 0.6 to 2.7. The biggest advantage of the IFS is spatially resolved spectroscopic information on galaxies, which is essential to investigate kinematics of the galaxies. Moreover, by

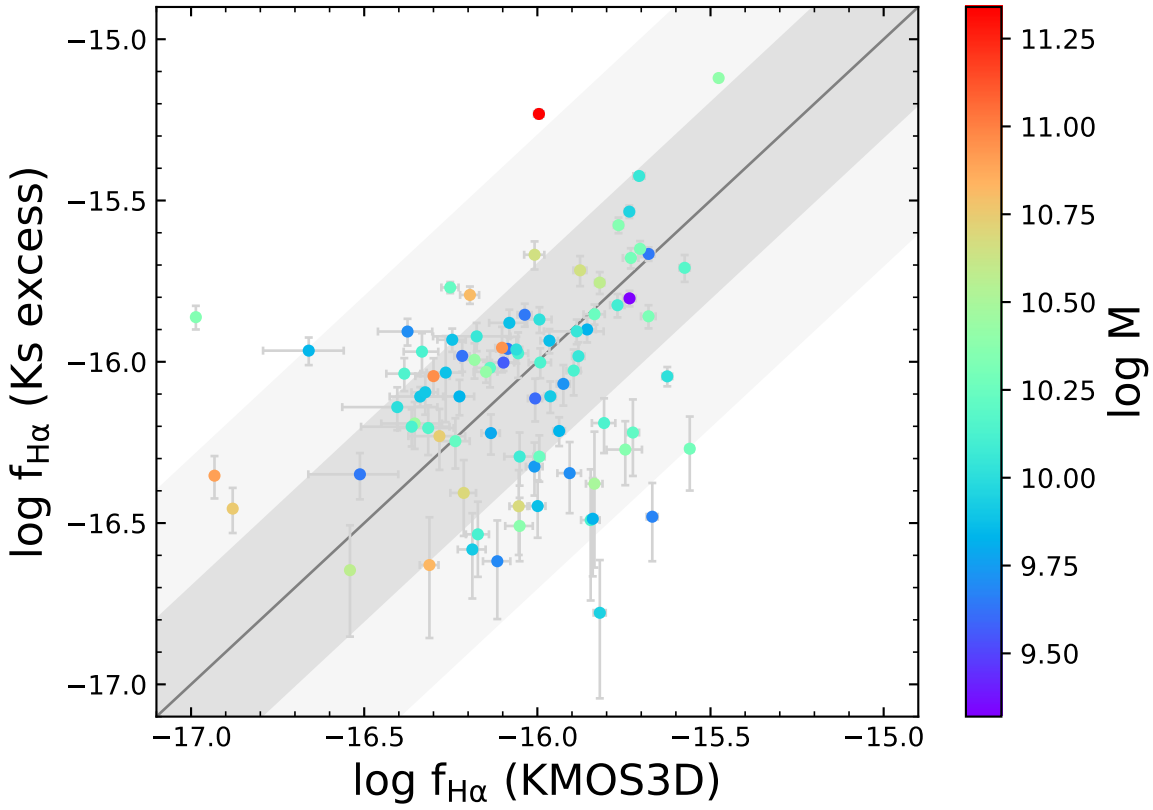

Figure 2.11: Same as Figure 2.8, but for the KMOS^{3D} and our method.

integrating the spatially resolved fluxes across the structures of the galaxies, one can obtain the integrated fluxes of the galaxies without suffering from the slit loss, which makes a direct comparison between photometry and long-slit spectroscopy difficult.

In our sample, spectra of 86 Hα emitters have been taken by the KMOS^{3D} survey (29, 21, and 36 in COSMOS, UDS, CDFS, respectively). Figure 2.11 shows a comparison of the Hα fluxes derived by our method and the IFS. For 53/86 (62%) of the Hα emitters, the Hα fluxes are consistent within a factor of 2.

2.3.4 Scatters between other methods

Scatters around the one-to-one relations between our method and the narrow-band color excess, the long-slit spectroscopy, and the integral field spectroscopy are 0.16 dex, 0.21 dex, and 0.23 dex, respectively, as shown above. However, it is unclear whether

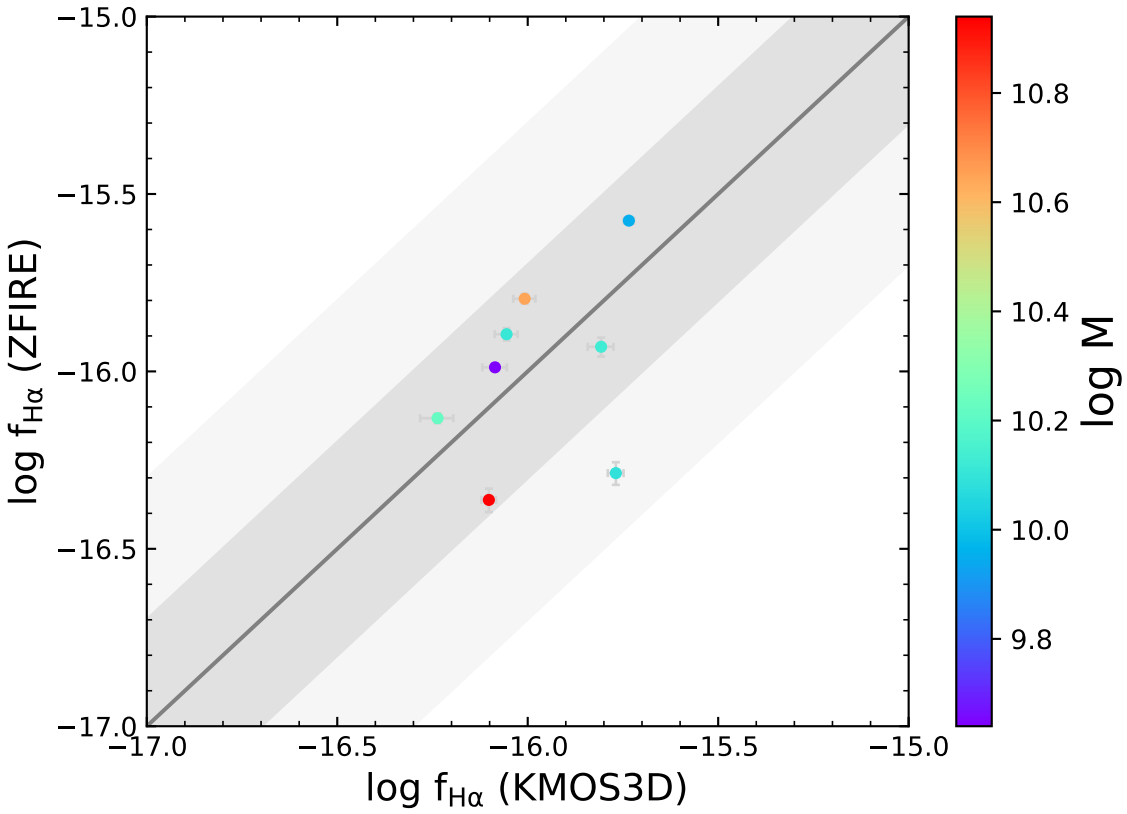

Figure 2.12: Same as Figure 2.8, but for the ZFIRE and the KMOS^{3D}.

the scatters are attributed to any systematics of our methods. Hence we also compare the Hα fluxes between the other three methods.

Figure 2.12 shows a comparison between the ZFIRE and the KMOS^{3D}. We note that the values of the ZFIRE are corrected for the slit loss (see § 2.3.2) assuming the aperture corrections applied to individual galaxies in the ZFOURGE. The mean factor of the correction is ~ 2.7. As a result, we find that the scatter between the ZFIRE and the KMOS^{3D} is 0.16 dex.

On the other hand, Figure 2.13 shows a comparison between the fluxes from the ZFIRE and the narrow-band color excess. The values of the ZFIRE are corrected for the slit loss again with a mean factor of ~ 2.3. We find that the scatter between the

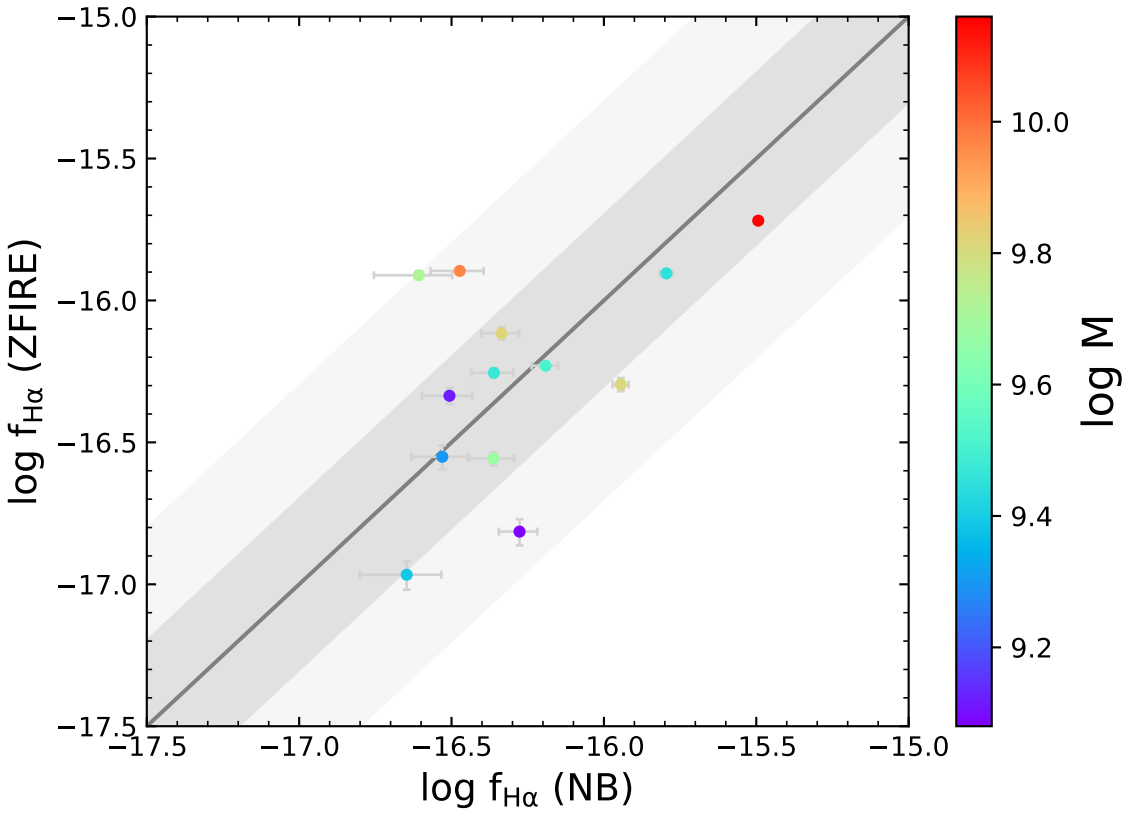

Figure 2.13: Same as Figure 2.8, but for the ZFIRE and the NB209 color excess.

ZFIRE and the narrow-band color excess is 0.22 dex.

There are only four galaxies observed in both the NB209 and the KMOS^{3D}. Hence we exclude the comparison of their fluxes from the scatter evaluation though individual fluxes are consistent.

Although the number of galaxies are small in the above two comparisons, the obtained scatters are consistent with those found between our method and the others. Therefore we conclude that there is no significant systematic error in our Hα flux derivation caused by the use of the flux excess.

2.4 SFR and correction for dust extinction

2.4.1 UV SFR

We estimate UV SFRs using flux densities at 1600 Å derived from SED fitting by EAZY (Brammer et al. 2008). According to Bell et al. (2005), spectral slopes of the UV continua between 1216–3000 Å of star-forming galaxies can be assumed to be flat. Therefore total UV luminosities integrated over this range can be approximated as follows:

$$L_{\rm UV} = 1.5\nu_{2800}L_{\nu,\rm UV}, \tag{2.7}$$

where ν_{2800} is the frequency corresponding to 2800 Å and $L_{\nu,\rm UV}$ is a flux density at a certain wavelength in the range of 1216–3000 Å. Then we convert the $L_{\rm UV}$ to the UV SFRs using the calibration of Bell et al. (2005), which is based on Fioc & Rocca-Volmerange (1997), assuming the Chabrier (2003) IMF:

$$\mathrm{SFR(UV)} = 1.09 \times 10^{-10} \times 2.2L_{\rm UV}. \tag{2.8}$$

2.4.2 IR SFR

IR SFRs are estimated from bolometric IR luminosities (8–1000 μm) which are re-radiations of the UV continua absorbed by dust. The bolometric luminosities are obtained by integrating the IR spectral template of Wuyts et al. (2007) over the rest-frame 8–1000 μm, where they are scaled to match the observed 24um fluxes . Then they are converted to the IR SFRs using the calibration of Bell et al. (2005) as well as the UV SFRs:

$$\mathrm{SFR(IR)} = 1.09 \times 10^{-10} \times L_{\rm IR}, \tag{2.9}$$

where $L_{\rm IR}$ is the bolometric IR luminosity.

2.4.3 Attenuation by dust

The amount of dust attenuation at rest-frame 1600 Å is estimated from the expression of Nordon et al. (2013),

$$A_{1600} = 2.5 \log \left\{ \frac{\mathrm{SFR(IR)}}{\mathrm{SFR(UV)}} + 1 \right\}, \tag{2.10}$$

where SFR(IR) and SFR(UV) are the IR and UV SFRs obtained above, respectively.

A_{1600} is then converted to $A_{\mathrm{H}\alpha}$ assuming the extinction curve of Calzetti et al. (2000). In this conversion, we assume that both stellar continua and nebulae emission lines are attenuated in the same way. Although there are uncertainties in the ratio of the amounts of stellar reddening to nebula, which is known as f-factor, it has been known that the f-factor increases with redshift and become nearly unity at $z \sim 2$ (e.g., Erb et al. 2006, Koyama et al. 2015, Kashino et al. 2017). Moreover, Faisst et al. (2019) have found that even in the local universe, where the typical f-factor is ~ 0.44, galaxies with high Hα equivalent widths ($\gtrsim 100$ Å) have the f-factors close to unity. As the redshifts of our Hα emitters are larger than 2 and their typical equivalent width is higher than 100 Å (see § 3.2), we adopt a fixed f-factor of unity for our sample, which enables a straightforward conversion from A_{1600} derived from the IRX to $A_{\mathrm{H}\alpha}$.

For galaxies with S/N < 3 of the Spitzer/MIPS 24 μm band detections, we estimate the amounts of the dust attenuation from A_V derived by the FAST (A_V(FAST)) as follows. First, we divide our sample into A_V(FAST) bins regardless of the MIPS S/N. Since the 24 μm fluxes are correlated with the amounts of the dust attenuation, galaxies with small A_V(FAST) have small or even negative 24 μm fluxes due to large photometric errors. However, when calculating median values in each bin, the medians are all positive and increase with A_V(FAST). Hence we regard the medians as typical intrinsic 24 μm fluxes of the galaxies in each bin. Using these fluxes, we calculate A_1600 in each bin via Equation 2.10 and convert it to A_V assuming the extinction curve of Calzetti et al. (2000), which we call A_V(IRX). Figure 2.14 shows a correlation between A_V(IRX) and A_V(FAST), where the best-fit relation is given by

$$A_{V,\mathrm{IRX}} = 0.034 A_{V,\mathrm{FAST}}^3 - 0.230 A_{V,\mathrm{FAST}}^2 + 1.59 A_{V,\mathrm{FAST}}. \tag{2.11}$$

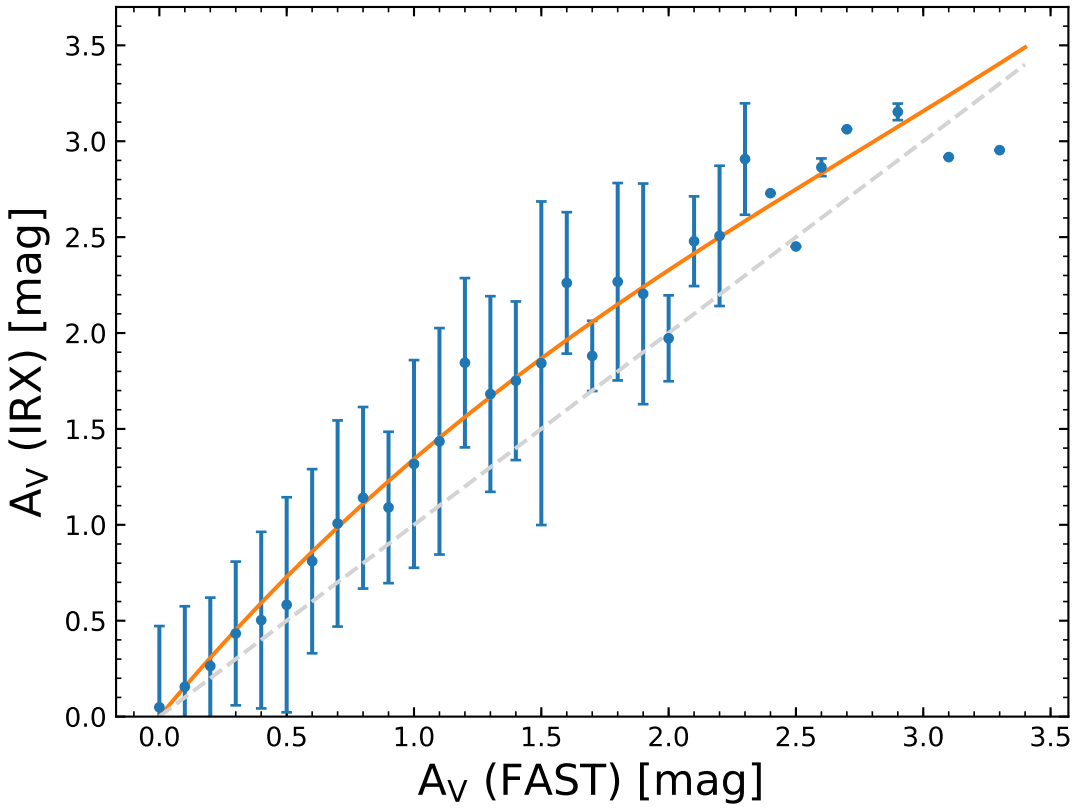

Figure 2.14: Best-fit relation between A_V derived from the SED fitting by the FAST and the IRX.

Both methods result in consistent A_V values. We convert the A_V values from the FAST to those corresponding to the IRX values using this relation for galaxies without the IR detection. Finally we obtain $A_{\mathrm{H}\alpha}$ by converting A_V using the curve of Calzetti et al. (2000) again.

2.4.4 Hα luminosity and SFR

Using the $A_{\mathrm{H}\alpha}$ values, we can derive Hα luminosities corrected for the dust attenuation.

$$L_{\mathrm{H}\alpha} = f_{\mathrm{H}\alpha} \times 4\pi d_{\mathrm{L}}^2 \times 10^{0.4 A_{\mathrm{H}\alpha}}, \tag{2.12}$$

where $f_{\mathrm{H}\alpha}$ is the Hα flux derived from the flux excess in the K_{s}-band, while d_{L} is the luminosity distance corresponding to the redshift of a galaxy .

We then convert $L_{\mathrm{H}\alpha}$ to Hα SFRs using the calibration of Kennicutt (1998) with a correction to the Chabrier (2003) IMF:

$$\mathrm{SFR}(\mathrm{H}\alpha) = 7.9 \times 10^{-42} \times L_{\mathrm{H}\alpha} \times 10^{-0.24}. \tag{2.13}$$

Chapter 3

Properties of Hα emitters at $z = 2.1$–2.5

3.1 Locations on the UVJ diagram

It is worth investigating where our Hα emitters are located on the UVJ diagram (See § 1.2.3). Since our emitter selection, which is based on the flux excess, and the UVJ diagram are independent methods of each other for galaxy classifications, we can make sure by the comparison that our method can properly select star-forming galaxies. Figure 3.1 shows the locations of the 2005 galaxies selected as the Hα emitters on the UVJ diagram. It is clear that most of the Hα emitters are classified as the star-forming galaxies, where we adopt the criterion of Spitler et al. (2014) for the classification. Identified AGNs by either IR, radio, or X-ray are indicated by the red open circles.

Although the fraction is very small, there are 37 Hα emitters in the quiescent region. We find a few low-mass galaxies classified as the quiescent (shown in bluer colors in Figure 3.1) have poorly fitted SEDs so that their rest-frame colors and stellar masses are not reliable. However, most of them have well-constrained SEDs (Figure 3.2) and more strict excess thresholds does not significantly reduce the number of the Hα emitters in the quiescent region (from 37 to 22 if a 3σ excess threshold is adopted). This may suggests that our emitter selection is sensitive enough to detect weak Hα emission lines from galaxies in quenching phases. Indeed, the quiescent Hα emitters show lower SFRs than similar-mass ones and are located below the main sequence at this redshift range

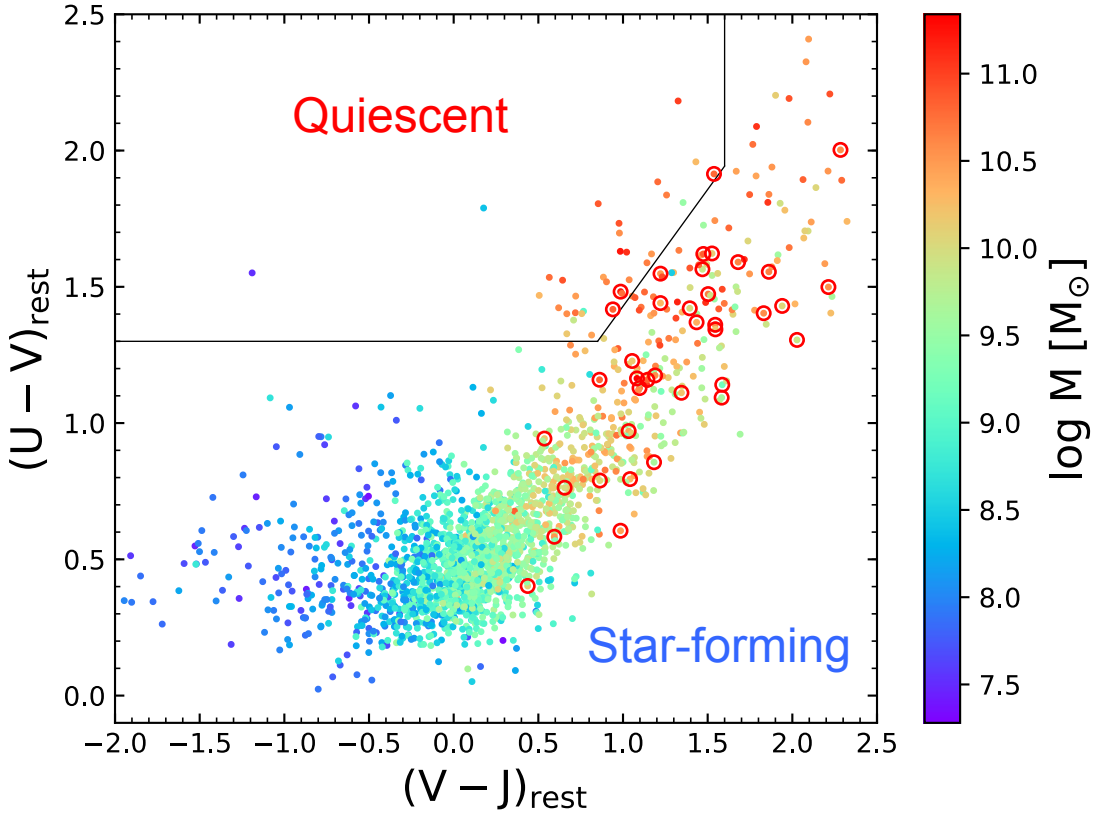

Figure 3.1: Locations of our Hα emitters on the UVJ diagram. The color gradient reflects stellar masses of the galaxies. The criterion of Spitler et al. (2014) is adopted to separate the star-forming and the quiescent regions.

as we will see in § 3.5. However we should note it is possible that the Hα emission lines of the quiescent galaxies are artificial. By the definition of our flux excess and emitter selection (§ 2.2), galaxies with strong stellar continua tend to be easily selected as the emitters even if their equivalent widths are small as photometric errors in a filter are nearly constant. Since the quiescent galaxies are massive, uncertainties in the continuum estimates by the SED fitting may cause unphysical flux excesses. Another possibility is contributions from unidentified AGNs but spectroscopic observations are needed to examine it. In any case, the existence of the quiescent Hα emitters does not affect statistical properties of our sample as their number fraction is only 1.8%.

We also check if the locations of our Hα emitters on the UVJ diagram and their

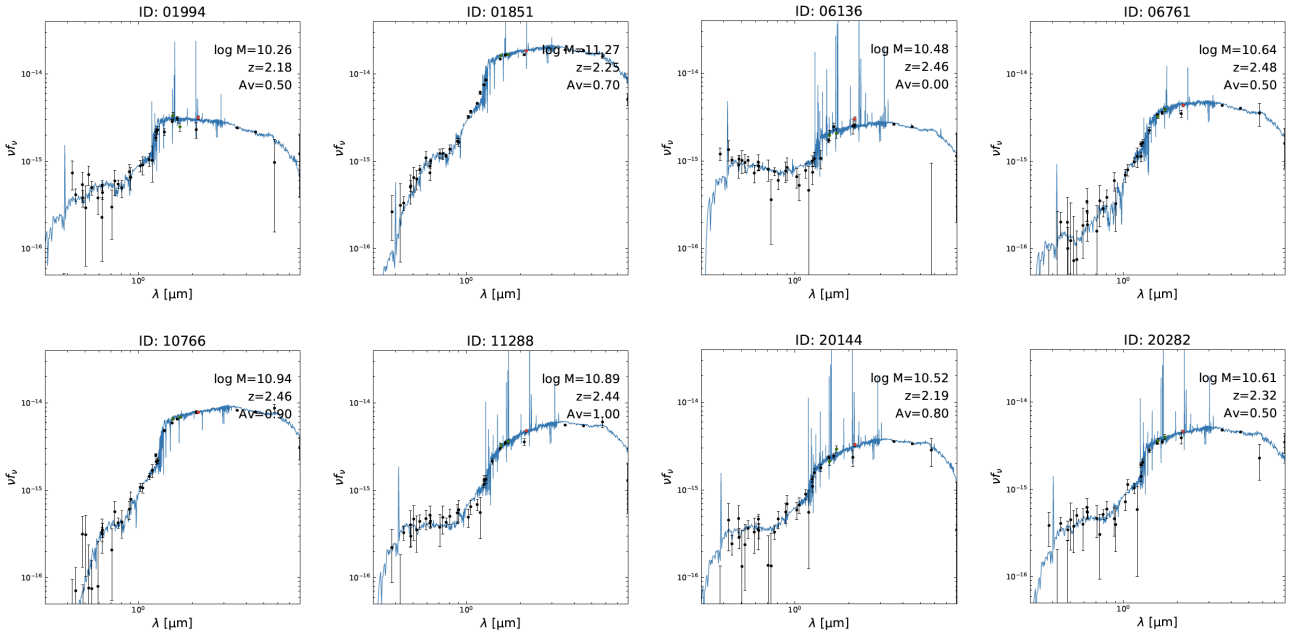

Figure 3.2: Examples of the best-fit SEDs of the Hα emitters classified as quiescent by the UVJ colors. Although the flux excesses in the K_s-band are not significant compared to the others, some show star formation features in their rest-frame UV spectra.

properties derived from the SED fitting are consistent. In Figure 3.3 the galaxies are color-coded based on the amounts of dust attenuation (A_V). Obviously A_V values increase toward the upper right in the star-forming region, which makes the effect of the dust extinction to the rest-frame colors visible. At fixed $(U - V)$ colors, moreover, the $(V - J)$ colors become redder with increasing A_V as expected from the results of previous works (see § 1.2.3). Quiescent galaxies, which have been thought to be a less-obscured passive population, indeed have small A_V values.

When it comes to ages of our sample, the situation is more complicated. Figure 3.4 shows the UVJ diagram color-coded by the ages of the galaxies. As expected, less-obscured star-forming galaxies, which are characterized by their blue $(U - V)$ colors, have younger ages while the quiescent ones seem much older. On the other hand, however, dusty star-forming galaxies on the upper right region show both young and old ages. To understand these populations, we examine their ages and A_V values (Figure 3.5) by defining the dusty star-forming population as the galaxies with $(U -$

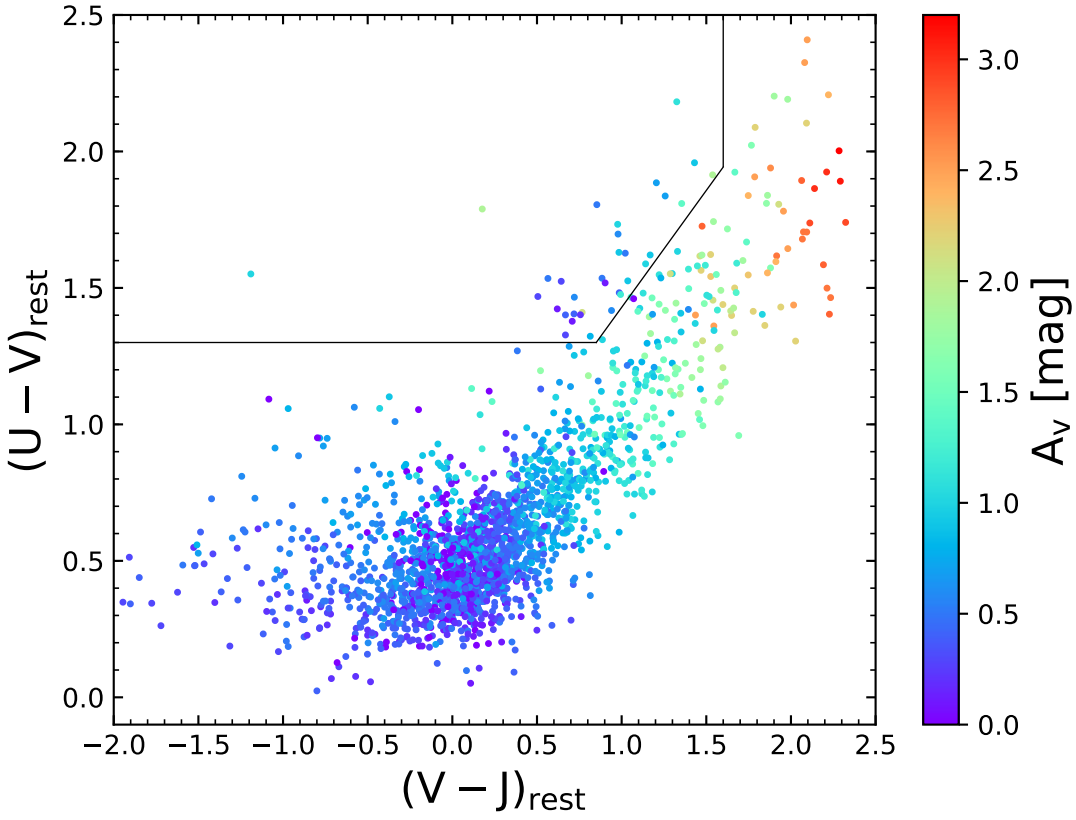

Figure 3.3: Same as Figure 3.1, but color-coded by the amounts of the dust attenuation.

$V) \geq 1.0$ in the star-forming region. We find the ages of the dusty star-forming galaxies show a bimodal distribution shown in the left panel of Figure 3.5. The right panel makes it clear that the younger galaxies have higher A_V values than the older ones as expected from their $(V - J)$ colors. The absence of dusty star-forming galaxies with intermediate ages might be explained by two distinct populations. One is the population evolving from the lower left to the upper right in the star-forming region. Such galaxies make the age gradient shown in Figure 3.4. Part of them might be quiescent galaxies with some amounts of dust or contaminations due to the incomplete criterion. The other population represents young dusty star-forming galaxies which can be even younger than the young unobscured population. These galaxies have very large A_V values, which correlate with luminous Hα emission lines as we will see in § 3.3. Therefore they may be starburst galaxies which are rapidly building their stellar

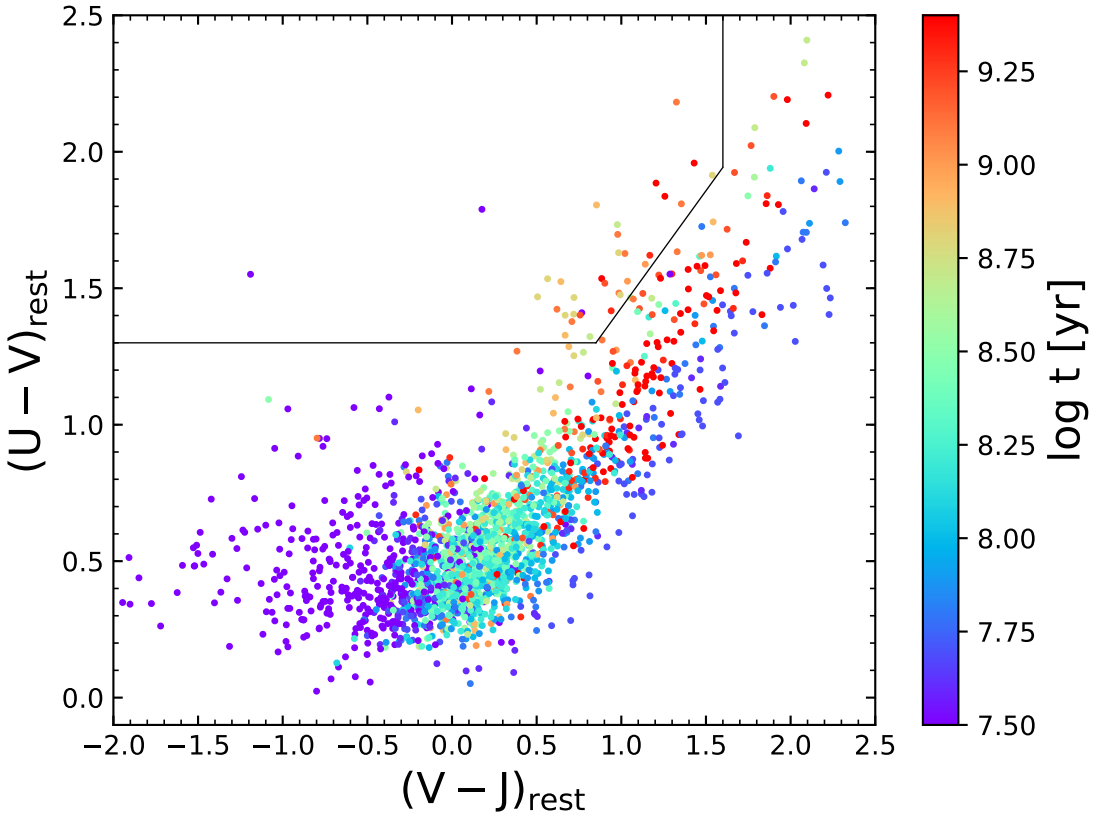

Figure 3.4: Same as Figure 3.1, but color-coded by the ages of the galaxies.

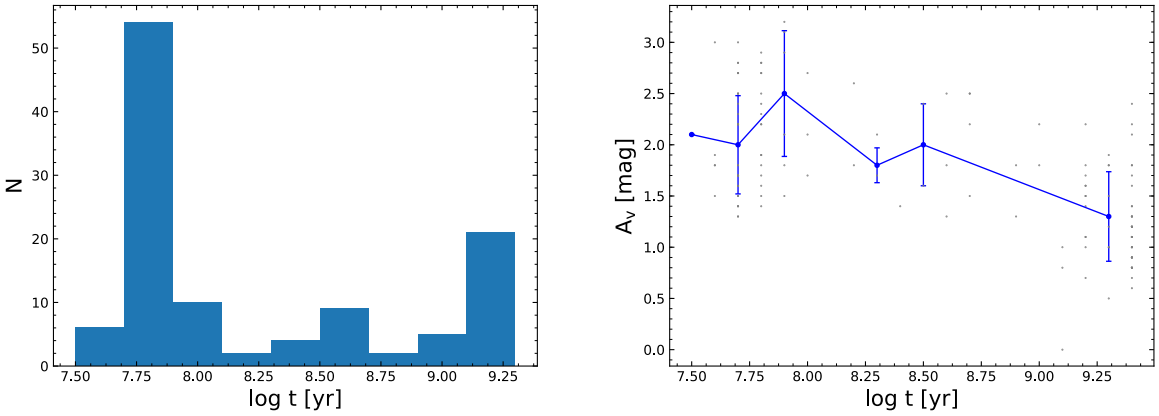

Figure 3.5: (Left): Distribution of the ages of the dusty star-forming galaxies derived by the SED fitting. There are two populations with younger and older ages. (Right): Correlation between the ages and the amounts of the dust attenuation of the dusty star-forming galaxies. The younger population tends to be more obscured by dust.

masses. Indeed, Tadaki et al. (2013) have suggested that there has been two modes of the dusty star-forming galaxies, where one is dusty due to central starbursts while the other has plenty of dust as a consequence of chemical evolution with aging. Our interpretation agrees with the one of Tadaki et al. (2013), but spectroscopic and/or spatially resolved information is necessary to confirm it.

3.2 Equivalent width

A total rest-frame equivalent width of all emission lines in the $K_{\rm s}$-band is calculated as follows:

$$EW(\mathrm{all}) = \frac{f_{\rm excess}}{f_{\rm cont}} \times W/(1+z), \tag{3.1}$$

where W is the bandwidth of the $K_{\rm s}$-band. Then an Hα equivalent width is obtained as follows:

$$EW(\mathrm{H}\alpha) = r_{\mathrm{H}\alpha} \times EW(\mathrm{all}). \tag{3.2}$$

3.2.1 Limiting equivalent width

First we estimate a limiting equivalent width above which our sample is complete. As mentioned in § 3.1, our emitter selection is more sensitive to strong continuum (i.e., massive) galaxies. Therefore the limiting equivalent width is expected to show stellar mass dependence.

By the definition of our emitter selection, we can calculate a minimum equivalent width of an emitter as

$$EW_{\rm min}(\mathrm{H}\alpha) = r_{\mathrm{H}\alpha} \times \frac{2f_{\rm err}}{f_{\rm cont}} \times W/(1+z), \tag{3.3}$$

which can be calculated for each galaxy. As the photometric errors in the $K_{\rm s}$-band do not vary among the galaxies, the values of $EW_{\rm min}(\mathrm{H}\alpha)$ strongly correlate with the stellar masses. We find the minimum Hα equivalent widths can be fitted well by a single slope so we use it as our functional limiting Hα equivalent width as follows:

$$\log EW_{\rm lim}(\mathrm{H}\alpha) = -0.46 \log M + 6.33. \tag{3.4}$$

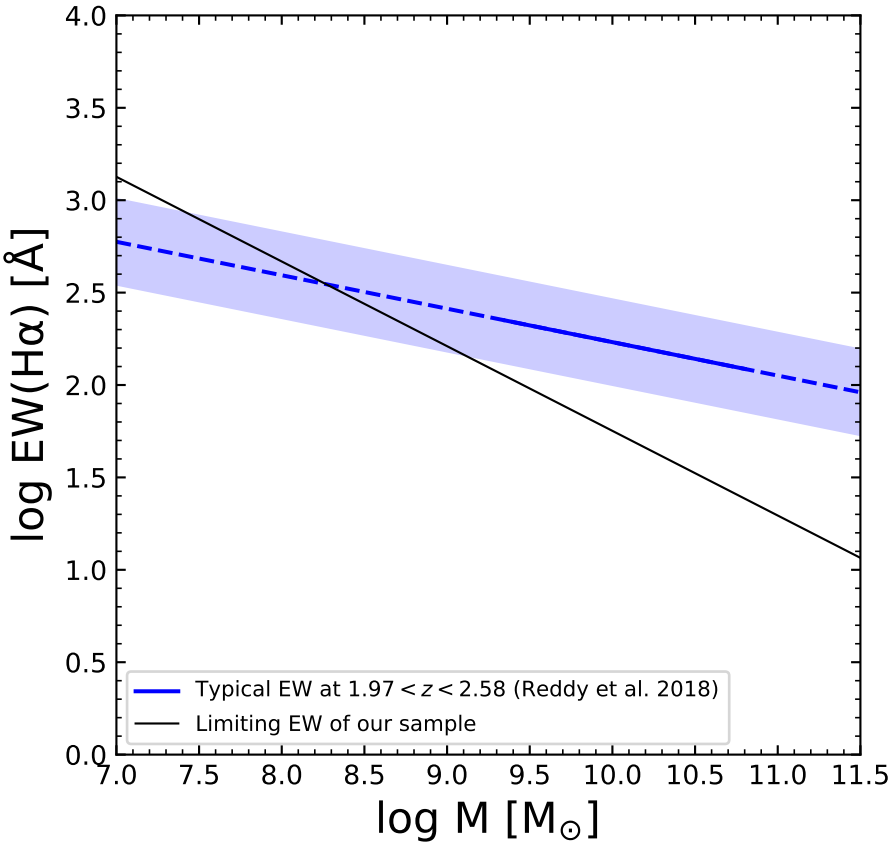

Figure 3.6: Limiting equivalent width of Hα as a function of stellar mass (black solid line). Since our selection is more sensitive to galaxies with strong continua, the limiting equivalent width depends on stellar mass. The blue line and intervals show the typical Hα equivalent width and its scatter reported by Reddy et al. (2018) for galaxies with $\log M \simeq 9.3$–10.7. Our method seems sensitive enough to detect most of the Hα emitters with $\log M > 9.0$, but only extreme ones can be detected below this limit.

Figure 3.6 shows the limiting equivalent width with a typical Hα equivalent width at $z \sim 3$ as a function of stellar mass, which is obtained by Reddy et al. (2018). The blue line represents the best-fit relation of Reddy et al. (2018) with a typical scatter shown as the blue shaded region. We find that our sample is quite complete at $\log M > 9.0$, which corresponds to the 80% mass completeness limit of the ZFOURGE at this redshift, though we may still miss some fractions of the emitters with low equivalent widths. This is thanks to the increase of mean equivalent widths at high-z, which enables us to select intermediate-mass emitters from the broad-band photometry. The

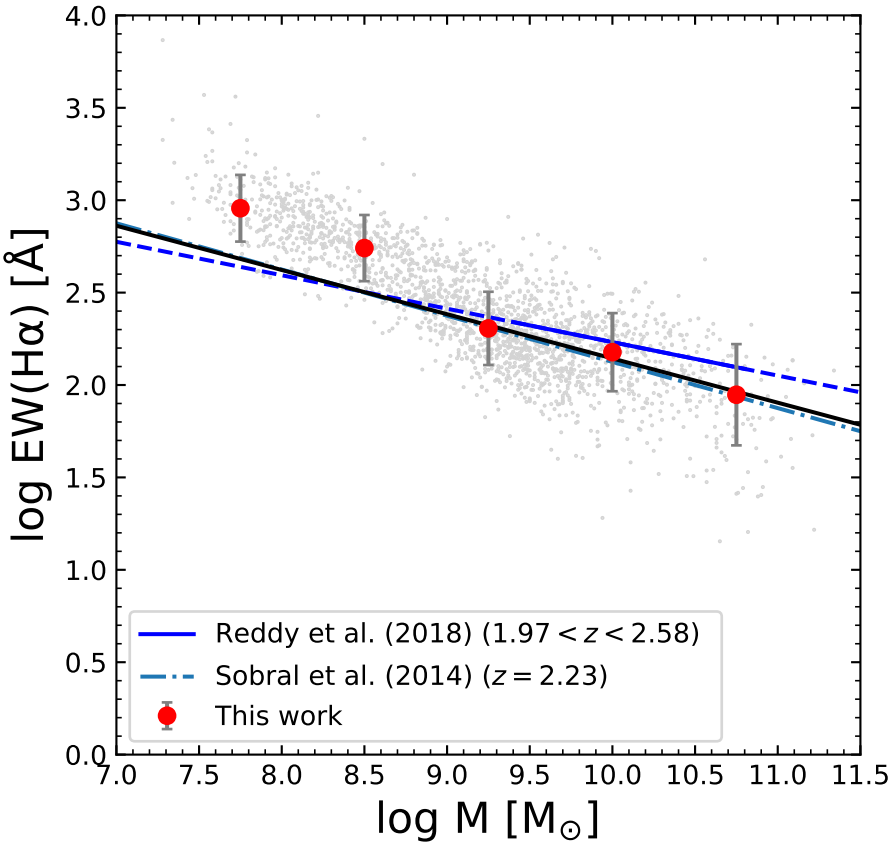

Figure 3.7: Hα equivalent widths of our sample as a function of stellar mass. The grey and red circles represent individual galaxies and their medians in the mass bins, respectively. The best-fit relation obtained in the range of $\log M > 9$ is shown by the black line extrapolated toward the low-mass end. The blue line is the relation found by Reddy et al. (2018).

use of medium-band filters will increase the sensitivities to equivalent widths without losing the advantage of larger searching volumes compared to narrow-band filters.

3.2.2 Stellar mass dependence

Figure 3.7 shows the Hα equivalent widths of our sample as a function of stellar mass. We find the best-fit relation between the equivalent width and the stellar mass at $\log M > 9.0$, which is expressed as

$$\log EW(\mathrm{H}\alpha) = -0.24 \log M + 4.54. \tag{3.5}$$

This agrees very well with the results of previous studies supporting the high completeness of our sample in this mass range.

For galaxies with $\log M < 9.0$, we cannot know their statistical properties due to the incompleteness. Nevertheless it is interesting that there are many low-mass Hα emitters that are selected due to their extremely high Hα equivalent widths (> 500 Å). They have higher equivalent widths than those predicted from the extrapolation of the relation in $\log M > 9.0$. Such galaxies are expected to have high sSFRs and we will investigate them further in § 3.5.

3.3 Dust attenuation

3.3.1 Correlation between SFR

Figure 3.8 shows a correlation between the Hα SFR (or luminosity) and the amount of Hα attenuation by dust. Clearly the galaxies with higher SFRs (i.e., luminous in Hα) are more obscured. This is unsurprising given the dust production in galaxies: it has been thought that dust in the inter stellar media (ISM) of the galaxies is mainly produced by super novae and AGB stars (e.g., Morgan & Edmunds 2003). Hence the amounts of the dust are correlated with SFRs of the galaxies, which results in the SFR dependence of the amount of the attenuation. Indeed galaxies most actively forming stars are the dusty ones both in the local and high-z universe. The best-fit relation between the Hα SFRs and the amounts of the dust attenuation in our sample is given by

$$A_{\mathrm{H}\alpha} = 0.95 \log \mathrm{SFR}(\mathrm{H}\alpha) - 0.51. \tag{3.6}$$

A similar relation is obtained comparing the amounts of the attenuation and UV+IR SFRs using only the galaxies detected in the Spitzer/MIPS 24 μm band with S/N>3 (390/2005; Figure 3.9):

$$A_{\mathrm{H}\alpha} = 0.99 \log \mathrm{SFR}(\mathrm{UV} + \mathrm{IR}) - 0.61. \tag{3.7}$$

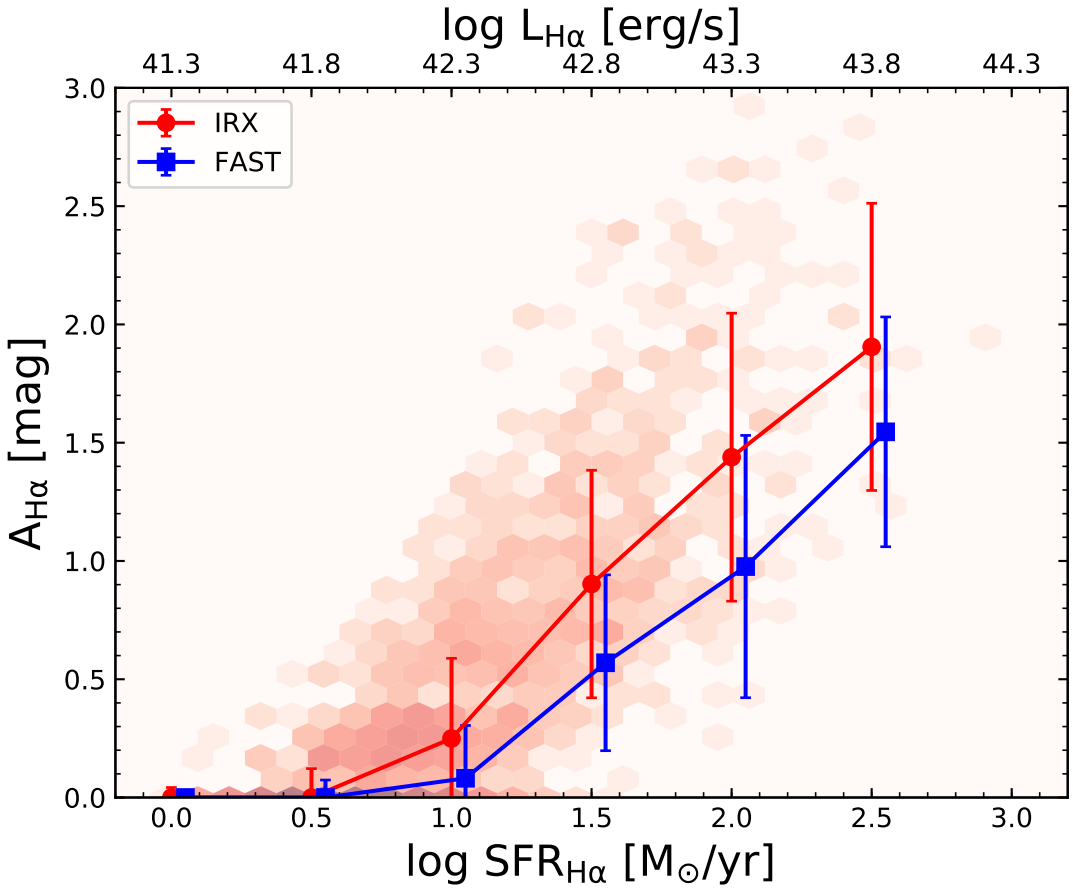

Figure 3.8: Correlation between Hα SFRs (luminosities) and the amounts of the dust attenuation to the Hα emission lines, $A_{\mathrm{H}\alpha}$. The red hexagonal tiles show the $A_{\mathrm{H}\alpha}$ distribution of our sample, where $A_{\mathrm{H}\alpha}$ values are derived by the IRX as described in § 2.4.3. Median values of $A_{\mathrm{H}\alpha}$ in SFR bins derived from the IRX and the SED fitting by the FAST are shown in the red circles and the blue squares, respectively.

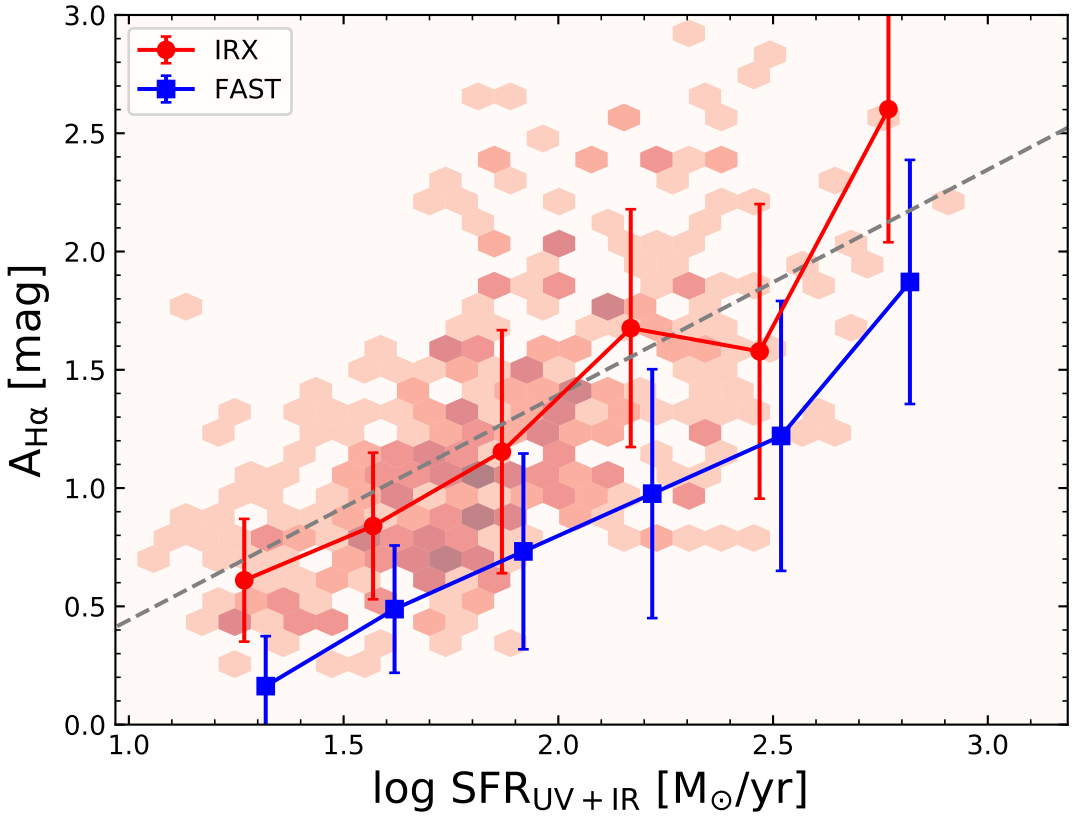

Figure 3.9: Correlation between the UV+IR SFRs and the values of $A_{H\alpha}$, where only the galaxies detected with S/N>3 in the Spitzer/MIPS 24 μm band are shown. The color coding is the same as Figure 3.8 while the grey dashed line represents the best-fit relation between the Hα SFRs and the $A_{H\alpha}$ values (Equation 3.6).

3.3.2 Different extinctions between IRX and SED fitting

Both relations above are for the $A_{H\alpha}$ derived from the IRX (see § 2.4.3). We find that there is an offset between the amounts of the attenuation derived from the IRX and the SED fitting by the FAST. For galaxies with SFR(Hα) > 10, a typical value of $A_{H\alpha}$ based on the IRX is ~ 0.21 mag larger than that from the SED fitting. This discrepancy may be explained by the different indicators both techniques use to estimate the amounts of the dust attenuation. In the SED fitting, the amounts of the attenuation are estimated from the slopes of the UV continua via an empirical relation (IRX-β relation; e.g., Meurer et al. 1999, Overzier et al. 2011). However, as the UV

continua are easily absorbed by the interstellar dust, the UV slopes only contain information on the surface regions when the galaxies are very dusty Qin et al. (e.g., 2019). On the other hand, the IRX method directly measures the ratios of the absorptions and re-radiations. Therefore the IRX can better trace the total amounts of the dust attenuation than the SED fitting which might underestimate the attenuation in the dusty galaxies.

3.4 Hα luminosity function

In this section, we show a Hα luminosity function of our sample and compare it with the result of a narrow-band imaging survey named High-z Emission Line Survey (HiZELS; Geach et al. 2008, Sobral et al. 2009, 2013).

3.4.1 Completeness estimate

Before deriving the luminosity function, we estimate the Hα luminosity completeness of the sample to properly interpret our results.

We evaluate the completeness by performing a brief simulation using observed relations. First we generate 100,000 mock galaxies with stellar masses following a power-law distribution with the slope of Tomczak et al. (2014) ($N \propto M^{-1.38}$). Then we estimate their stellar continuum fluxes in the $K_{\rm s}$-band using a relation between the continuum fluxes and the stellar masses of our sample. Next, Hα luminosities of the galaxies are drawn from a normal distribution with a mean and a standard deviation corresponding to the observed SFMS and its scatter (see § 3.5). These Hα luminosities are then converted to the flux excesses, where redshifts of the galaxies are randomly chosen from the observed distribution. Finally we obtain their total fluxes by adding the excesses to the stellar continuum fluxes. To reproduce the $K_{\rm s}$ detection limit of the real data, we require the simulated total fluxes to be five times larger than simulated errors which are generated from the observed relation between the continuum fluxes and the photometric errors. In addition, we apply the excess threshold in § 2.2 to the simulated flux excesses to be identified as emitters. By calculating fractions of the emitters above the detection limit in each Hα luminosity bin, we obtain the completeness as a function of

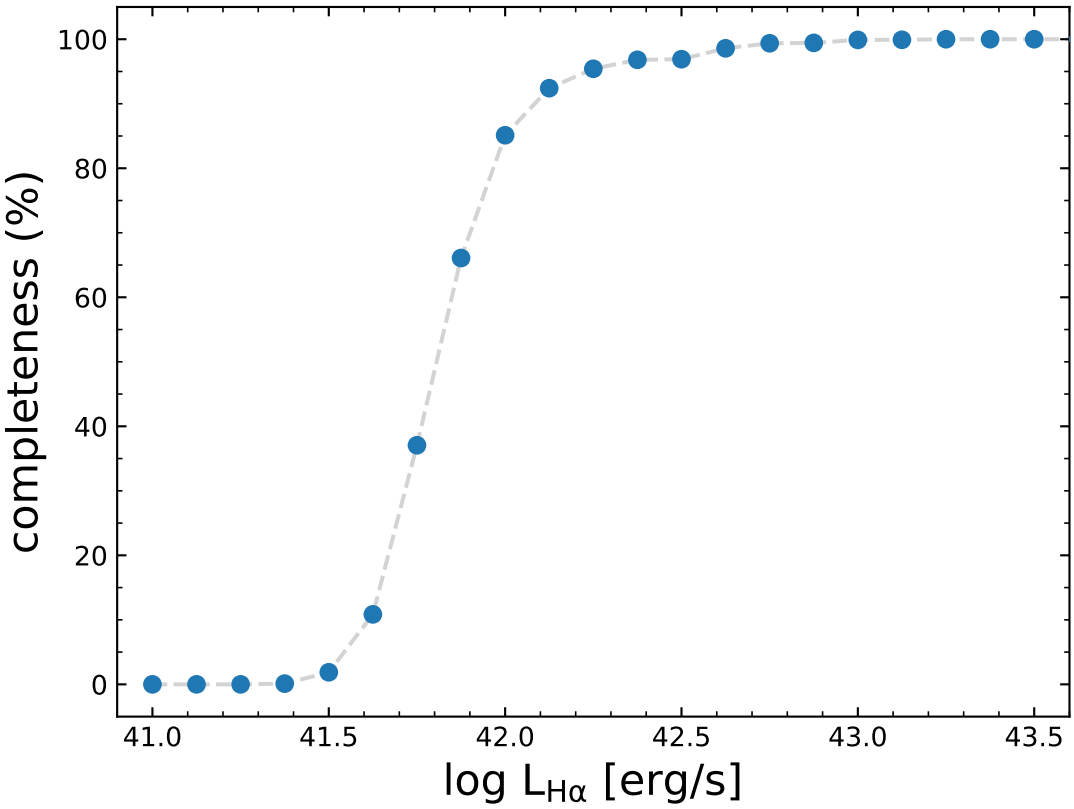

Figure 3.10: Simulated completeness as a function of the Hα luminosity

the Hα luminosity (Figure 3.10), where the dust extinction is taken into account. We

Table 3.1: Simulated completeness in Hα luminosity bins

$\log L(\mathrm{H}\alpha)$ (erg/s)	< 41.25	41.5	41.75	42.0	42.25	> 43.0
completeness (%)	0	1.4	35	85	96	100

find that almost all the galaxies with $\log L(\mathrm{H}\alpha) > 42.25$ are selected as the emitters in our simulation (Table 3.1. Therefore no completeness correction is needed to the luminosity function above this value.

3.4.2 Calculation

3.4.2.1 Number density

Number densities of the Hα emitters at fixed luminosities are calculated by dividing the numbers of the emitters in each luminosity bin by the comoving volume determined by the redshift range and the survey area. In our case, the total comoving volume searched by the K_s-band of the ZFOURGE is $\sim 5.51 \times 10^5$ Mpc^3 (see Table 3.2 for individual fields). We decide the width of the luminosity bins as 0.25 in logarithmic

Table 3.2: Searched comoving volume of ZFOURGE in each field

COSMOS	UDS	CDFS
$\sim 1.88 \times 10^5$ (Mpc^3)	$\sim 1.83 \times 10^5$ (Mpc^3)	$\sim 1.79 \times 10^5$ (Mpc^3)

scale ($\Delta \log L = 0.25$). Then a number density of the emitters is calculated as follows:

$$\phi(\log(L_c)) = \frac{1}{\Delta(\log L)} \sum_{|\log \frac{L_i}{L_c}| < \frac{\Delta \log L}{2}} \frac{1}{\Delta V}, \tag{3.8}$$

where we count the number of galaxies within a bin and divide it by the total volume (ΔV) and the bin width. This definition is the same as the one used in Sobral et al. (2009).

3.4.2.2 Schechter function fitting

We fit a Schechter function to the number densities to obtain the best-fit Hα luminosity function, which is defined as:

$$\phi(L)dL = \ln 10 \phi^* \left(\frac{L}{L^*}\right)^{\alpha} e^{-(L/L^*)} \left(\frac{L}{L^*}\right) d\log L, \tag{3.9}$$

where L^*, α, and ϕ^* are a characteristic luminosity, a faint-end slope, and a normalization, respectively.

Figure 3.11 shows the luminosity function of our Hα emitter sample and the result of Sobral et al. (2013) for a comparison, which is based on the narrow-band imaging data taken by the HiZELS. Best-fit parameters are listed in Table 3.3. Obviously there is

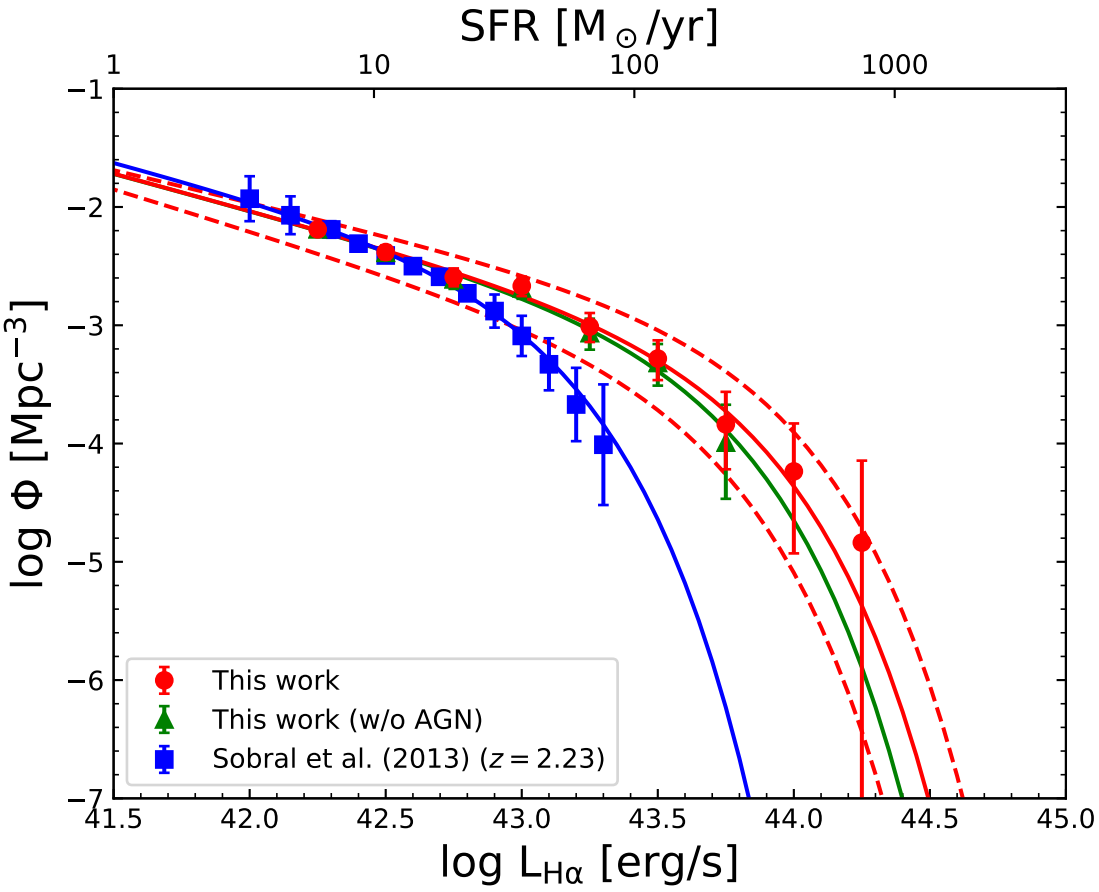

Figure 3.11: Hα luminosity function of our sample with the result of Sobral et al. (2013) for a comparison, which are shown by the red circles and the blue squares, respectively. The green triangles illustrate how our result change when removing the AGNs. Each curve shows the best-fit Schechter function with the parameters summarized in Table 3.3, where 1σ fitting uncertainties of our result are shown by the red dashed curves.

Table 3.3: Best-fit parameters of Hα luminosity functions

	α	$\log L^*$	$\log \phi^*$
This work	-1.62	43.6	-3.38
This work (w/o AGN)	-1.61	43.5	-3.30
This work ($A_{\mathrm{H}\alpha} = 1$)	-1.53	43.3	-3.11
Sobral et al. (2013)	-1.59	42.9	-2.78
Sobral et al. (2013) w/ correction	-1.74	43.2	-3.09

an excess in the bright-end of our luminosity function compared to that of Sobral et al. (2013), while the faint-end slopes are consistent. We should note that the brightest two bins of our luminosity function completely consist of the AGNs. Nevertheless, the excess still exists even when they are removed.

3.4.3 What causes the bright-end excess?

We investigate the origin of the bright-end excess in our luminosity function. Here we introduce two possible causes. One is related to structural properties of the galaxies, while the other is different corrections for the dust extinction between this work and Sobral et al. (2013).

3.4.3.1 Extended Hα profile

It has been thought that galaxies form their stars in disks around central cores and increase their sizes, which has been called inside-out growths (e.g., van Dokkum et al. 2010). At $0.7 < z < 1.5$, Nelson et al. (2016) have found that radial profiles of Hα emission lines are more extended than stellar components using stacking images taken by the 3D-HST. Moreover, they have showed that the offset of the light profiles has become larger with increasing stellar mass. Even at $z > 2$, Suzuki et al. (2019) have also revealed the extended Hα profiles with AO-assisted imaging data. These results suggest the importance of the sizes of apertures used in photometry to contain all the

extended Hα fluxes.

The photometry contained in the ZFOURGE catalog was originally performed with the 1.″2 aperture and then the measured fluxes were corrected to total fluxes using growth curves in the $K_{\rm s}$-band (Straatman et al. 2016). On the other hand, in the HiZELS catalog, Sobral et al. (2009) used a fixed 2″ aperture for all galaxies so they might have missed some fractions of the Hα fluxes. To estimate how much their fixed aperture can affect the luminosity function, we perform a simulation as follows. First we assume that an intensity of a galaxy follows a Sérsic profile Graham & Driver (2005), that is

$$I(R) = I_{\rm e}\left\{-b_n\left[\left(\frac{R}{R_{\rm e}}-1\right)^{1/n}\right]\right\}, \tag{3.10}$$

where n is a Sérsic index while $R_{\rm e}$ is an effective radius at which $I(R_{\rm e}) = I_{\rm e}$. We adopt the Sérsic indices measured by Nelson et al. (2016) as listed in Table 3.4. Then b_n is determined to satisfy following equation:

$$\Gamma(2n) = 2\gamma(2n, b_n), \tag{3.11}$$

where $\Gamma(n)$ and $\gamma(n, x)$ are complete and incomplete gamma functions, respectively.

Table 3.4: Structural parameters of Nelson et al. (2016)

$\log M/M_\odot$	n	$R_{\rm e}$ (kpc)
$9.0 < \log M/M_\odot < 9.5$	1.83 ± 0.15	1.77 ± 0.11
$9.5 < \log M/M_\odot < 10.0$	1.98 ± 0.16	2.91 ± 0.17
$10.0 < \log M/M_\odot < 10.5$	1.47 ± 0.10	3.10 ± 0.20
$10.5 < \log M/M_\odot < 11.0$	1.90 ± 0.20	5.34 ± 0.80

To reproduce the observation, we convolve the intensities with a point spread function (PSF) corresponding to the seeing. According to Trujillo et al. (2001), the seeing can be modeled as a moffat profile:

$$\mathrm{PSF}(r) = \frac{\beta-1}{\pi^2\alpha}\left[1+\left(\frac{r}{\alpha}\right)^2\right]^{-\beta}, \tag{3.12}$$

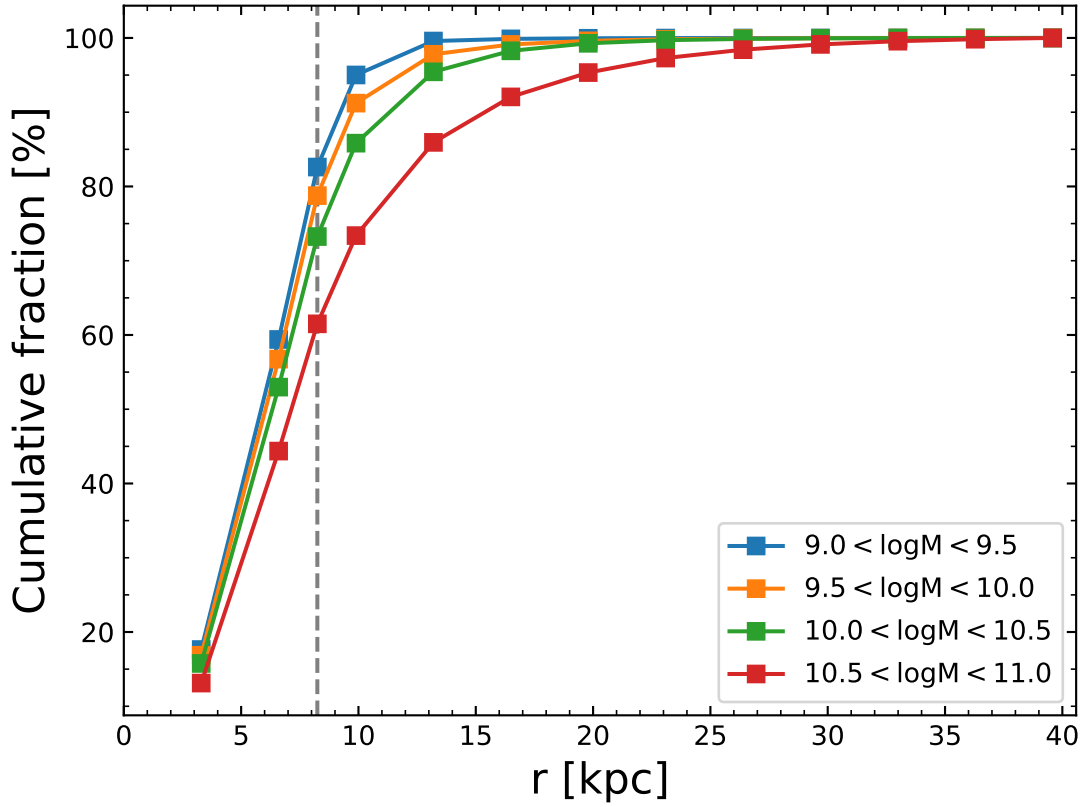

Figure 3.12: Cumulative fractions of Hα as a function of radius in our simulation. They are obtained assuming the Sérsic profiles with the structural parameters of Nelson et al. (2016) and the seeing of the HiZELS observation. The color coding reflects stellar masses of the galaxies, while the grey vertical dashed line shows the physical scale corresponding to the 2″ aperture used in Sobral et al. (2013).

where $\beta = 2.5$. A relation between the FWHM of the seeing, α and β is given as

$$\mathrm{FWHM} = 2\alpha\sqrt{2^{1/\beta} - 1}. \tag{3.13}$$

In the case of the HiZELS, the FWHM of the seeing is $\sim 1''$ (Geach et al. 2008). We create artificial images with the above models and perform photometry with varying aperture sizes. As a result, we obtain cumulative fractions of Hα as a function of radius (Figure 3.12). The radius corresponding to the 2″ aperture at $z = 2.23$ is ~ 8 kpc and shown by the grey dashed vertical line in Figure 3.12. We can clearly see that $\gtrsim 20\%$ of the Hα fluxes are contributed from the outside of their aperture. Especially for the most massive galaxies, which are expected to be in the bright-end of the luminosity

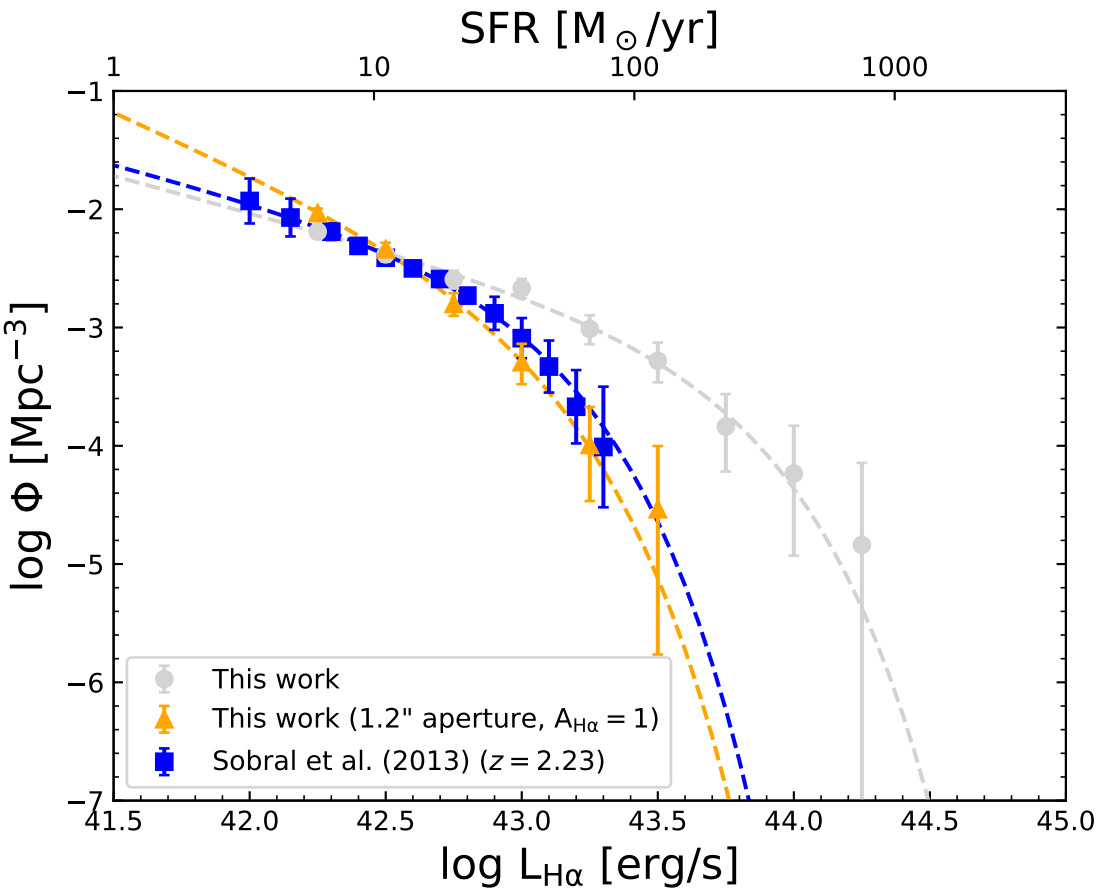

Figure 3.13: Hα luminosity function derived from the ZFOURGE data without the aperture corrections assuming $A_{\mathrm{H}\alpha} = 1$ (orange triangles). The difference between this work (grey circles) and Sobral et al. (2013) (blue squares) is almost completely reduced.

function, Sobral et al. (2013) might have missed $\sim 40\%$ of the Hα fluxes. We should note, however, that the measurements of radial profiles of the Hα fluxes in Nelson et al. (2016) are truncated at the radii of ~ 10 kpc. Therefore our simulation assumes the same structural parameters beyond these radii though that is not obvious.

The effects of the missing fluxes can be also clearly seen in Figure 3.13, where we show a luminosity function (orange triangles) derived from the ZFOURGE data without the aperture corrections assuming a fixed Hα attenuation of 1 mag, which is the same as Sobral et al. (2013). Although corresponding physical scales of the apertures of the

ZFOURGE (~ 5 kpc) and Sobral et al. (2013) (~ 8 kpc) and their seeing sizes ($\sim 0.''5$ and $\sim 1''$, respectively) are slightly different, the two luminosity functions agree very well. This result makes sure that the missing Hα fluxes due to the extended profiles significantly affect the bright-end of the Hα luminosity functions.

When we correct the luminosity function of Sobral et al. (2013) by taking the missing fluxes into account, it moves toward the brighter direction as shown in Figure 3.14 where the difference between the HiZELS and ours in the bright-end is reduced. Therefore we conclude that about half of the excess in our luminosity function can be explained by the missing Hα fluxes in Sobral et al. (2013).

3.4.3.2 Strong attenuation to the luminous galaxies

Another difference between this work and Sobral et al. (2013) is the manner of the correction for the dust attenuation. As discussed in § 3.3, there is a positive correlation between the Hα luminosities and the amounts of the dust attenuation. However, Sobral et al. (2013) have assumed $A_{\mathrm{H}\alpha} = 1$ mag for all the galaxies. Hence they have underestimated intrinsic luminosities of the brightest Hα emitters, which have caused a part of the difference from our luminosity function. We recalculate our number densities of the most luminous Hα emitters ($\log \mathrm{H}\alpha > 43.9$) with assuming the fixed attenuation ($A_{\mathrm{H}\alpha} = 1$ mag) to examine its effect. As a result, the brightest two bins disappear and the offset is reduced to some extent (Figure 3.15). From these results, we conclude that the discrepancy between the luminosity functions is mostly explained by the extended Hα profiles and the larger $A_{\mathrm{H}\alpha}$ values of the bright Hα emitters. Therefore we argue that there are more intrinsically very bright Hα emitters than previously reported. However, since the number of such objects is small, there are uncertainties such as cosmic variances and contributions of AGNs. Larger surveys and spectroscopic follow-ups are required to better understand the populations in the bright-end.

3.4.4 Cosmic star formation rate density

By integrating the luminosity function, we can derive a cosmic SFRD at $2.1 < z < 2.5$. Here we remove the contribution from the identified AGNs, which is $\sim 13\%$ to the

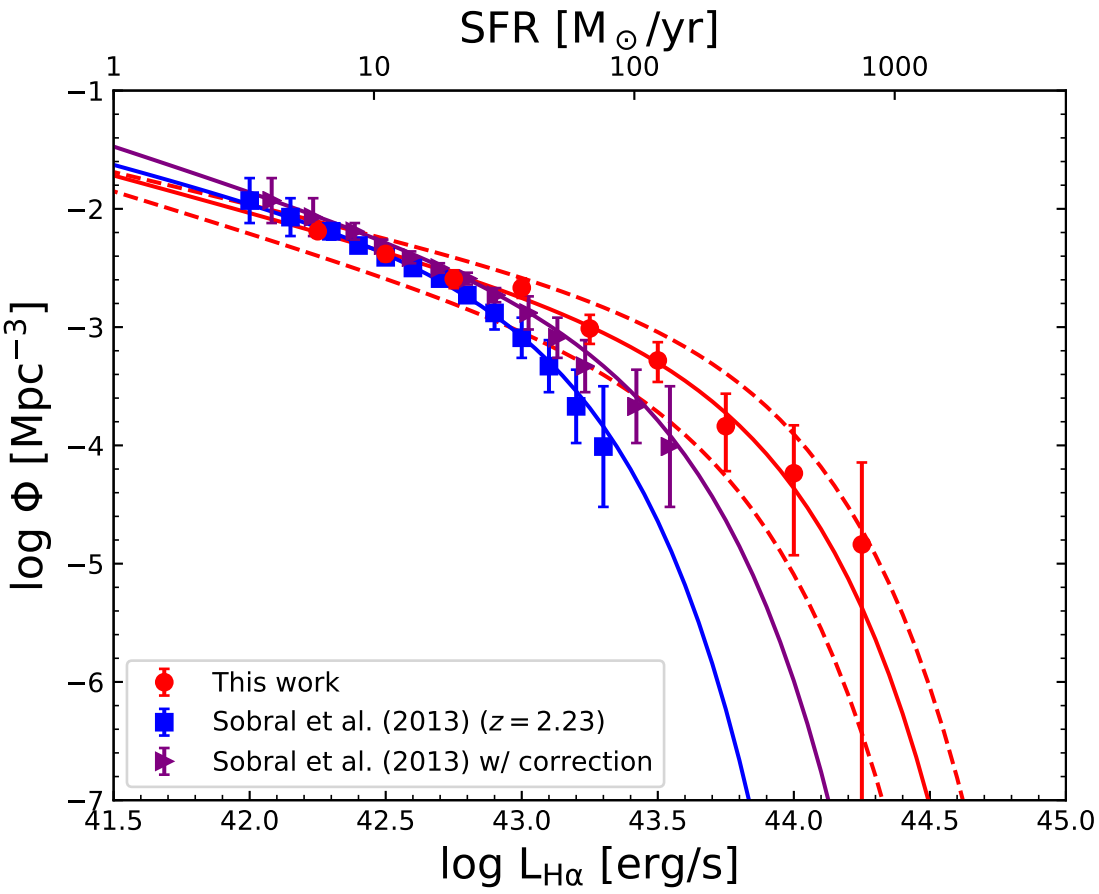

Figure 3.14: The red and blue are the same luminosity functions as Figure 3.11. The purple triangles show the values obtained when we correct the result of Sobral et al. (2013) for the missing Hα fluxes based on the mass-dependent cumulative fractions in our simulation (Figure 3.12). As the stellar mass information of individual galaxies of Sobral et al. (2013) is not available, we calculate a correction factor for each luminosity bin using observed distributions in our data. Specifically, we examine the stellar mass distribution of our sample in each luminosity bin and calculate a correction factor weighted by the number of the galaxies in each stellar mass range. Then we correct the result of Sobral et al. (2013) assuming the same stellar mass distributions in the luminosity bins.

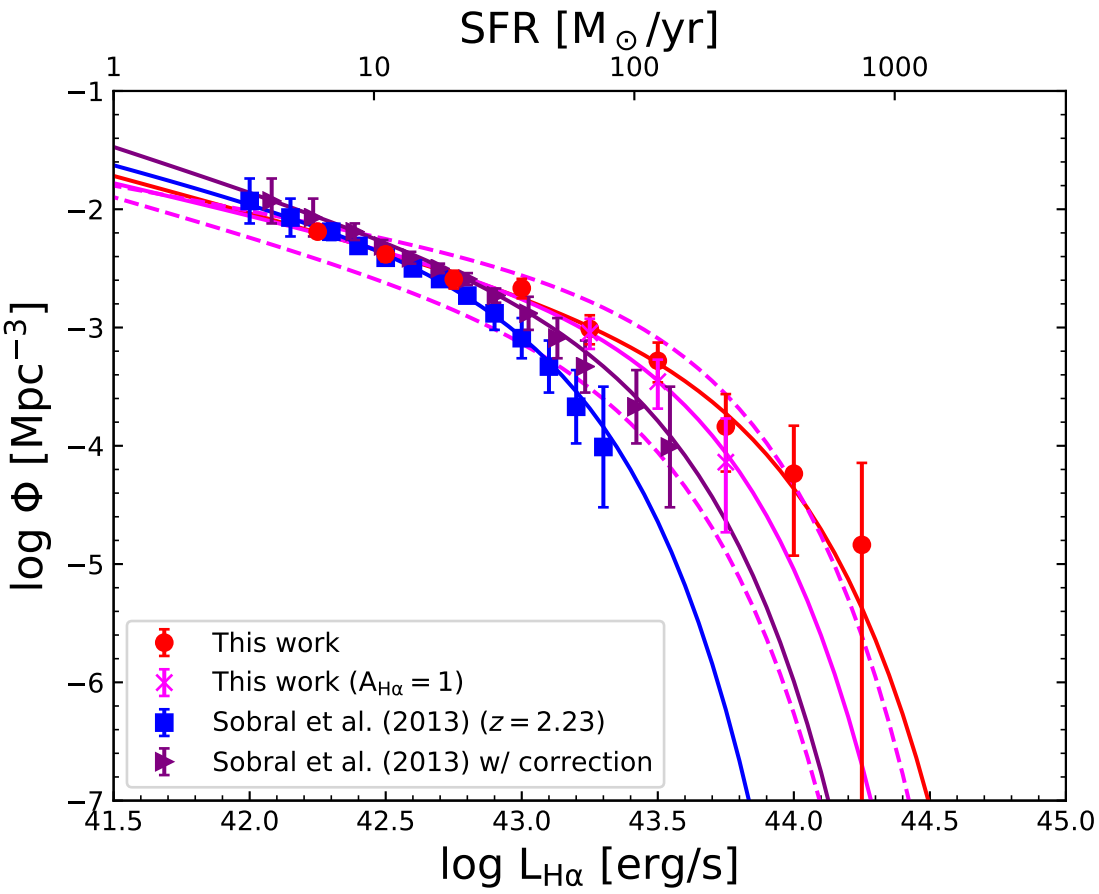

Figure 3.15: The red, blue, and purple are the same luminosity functions as Figure 3.14. The magenta crosses show how the bright-end of our luminosity function is suppressed when using the same assumption as Sobral et al. (2013) for the dust attenuation, $A_{\mathrm{H}\alpha=1\ \mathrm{mag}}$, of all the luminous galaxies.

total Hα luminosity. This fraction is obtained by dividing the total Hα luminosity of the AGNs by the total Hα luminosity of all the galaxies. In addition, we perform the integration with two intervals because the faint-end slope of the luminosity function is uncertain. One is the range of $L_{\mathrm{H}\alpha} = 0$–10^{45} erg s^{-1}, while the other is between $L_{\mathrm{H}\alpha} = 10^{41.6}$–$10^{45}$ erg s^{-1}. These intervals are the same as those used in Sobral et al. (2013), where $L_{\mathrm{H}\alpha} = 10^{41.6}$ erg s^{-1} corresponds to $0.01L^*$.

Given that the Hα emission line is the most direct SFR tracer and that Hα emitters cover diverse populations of star-forming galaxies (Oteo et al. 2015), we can expect

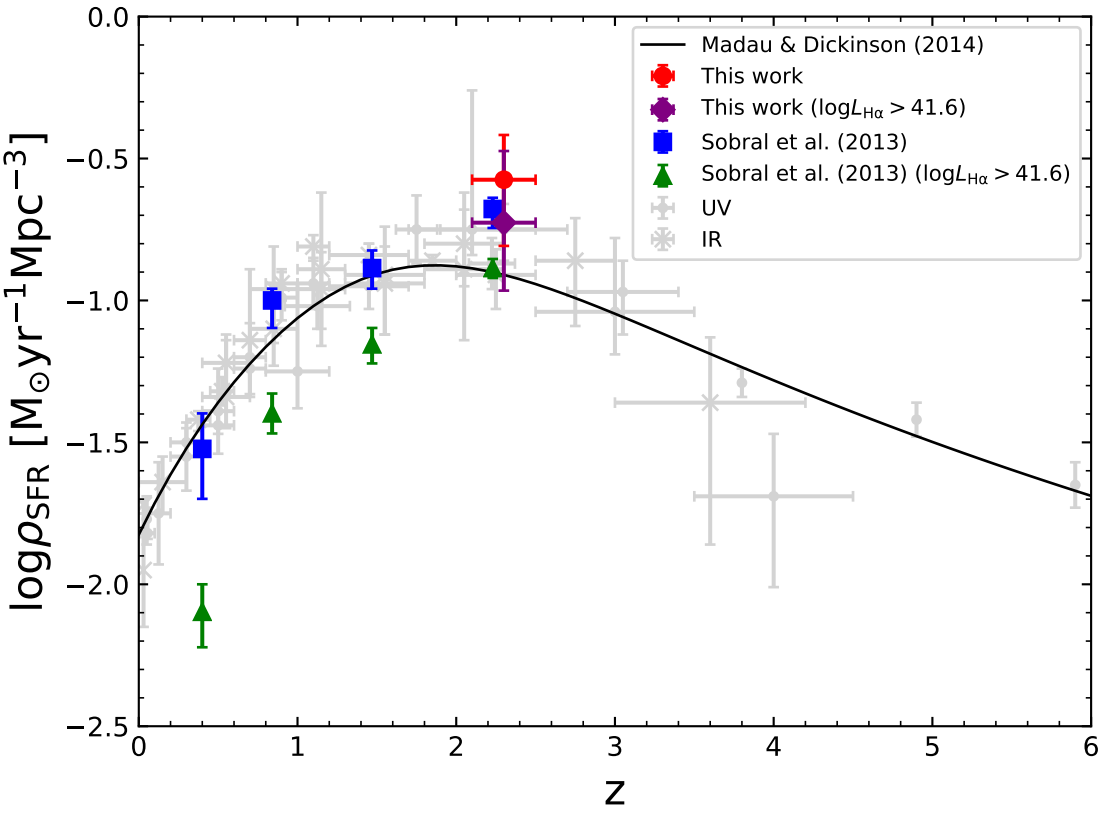

Figure 3.16: Our cosmic star formation rate density in the context of its redshift evolution reported by previous studies. The red circle and blue squares represent our measurement and the results of Sobral et al. (2013), respectively, which are obtained by integrating the Hα luminosity functions. AGN contributions have been removed from both values. The grey circles and crosses show the results of previous studies summarized in Madau & Dickinson (2014) for a comparison, which are measured from UV and/or IR luminosities.

a consistent Hα SFRD with previous studies based on UV and/or IR observations. Figure 3.16 shows our SFRD with the values previously reported at various redshifts, which are summarized in Madau & Dickinson (2014). We find that our SFRD agrees well with those observations. This suggests that our Hα emitter selection successfully reproduces the entire populations of star-forming galaxies and that our correction for the dust attenuation properly works to recover total Hα SFRs. However, though our

data contains the Spitzer/MIPS 24 μm band information, we cannot reject a possibility that there are some missing populations strongly obscured by the dust because our selection requires the galaxies to be detected in the K_s-band.

Despite the excess in the luminosity function, our result is consistent with Sobral et al. (2013). This indicates small contributions of the brightest galaxies to the total star formation activity in the universe because of their very small numbers.

3.5 Star formation main sequence

In this section, we investigate the star formation main sequence (SFMS) of our Hα emitter sample. Specifically, we derive the best-fit SFMS and compare its slope and normalization with previous studies. Then we show sSFRs of our sample as a function of stellar mass, where many low-mass galaxies with high sSFRs are found. Finally we examine SFHs of the low-mass galaxies using Hα/UV luminosity ratios. In our SFMS analysis, all the AGNs identified by either X-ray, IR, or radio (38/2005) are removed while the quiescent Hα emitters (see § 3.1) are included.

3.5.1 Main sequence at $z = 2.1$–2.5

Figure 3.17 shows a correlation between stellar masses and Hα SFRs of our sample with SFMSs of previous studies (Speagle et al. 2014, Whitaker et al. 2014, Behroozi et al. 2013). The black line represents our best-fit SFMS, which is given by

$$\log \mathrm{SFR}(\mathrm{H}\alpha) = 0.66 \log M - 5.32. \tag{3.14}$$

In the fitting, we only use the galaxies in the range of $9 < \log M/M_\odot < 11$ because our sample is incomplete at $\log M/M_\odot < 9$ while the number of the most massive galaxies is small and most of them are classified as the quiescent. Our results is consistent with the previous studies. Especially, the good agreement with (Whitaker et al. 2014), where SFRs were derived from UV+IR luminosities, indicates that our correction for the dust attenuation successfully recovers total Hα SFRs. The small offset in the most massive bins, though within scatters, is probably due to different selections for the star-forming galaxies. A selection by FIR detections may bias a sample toward

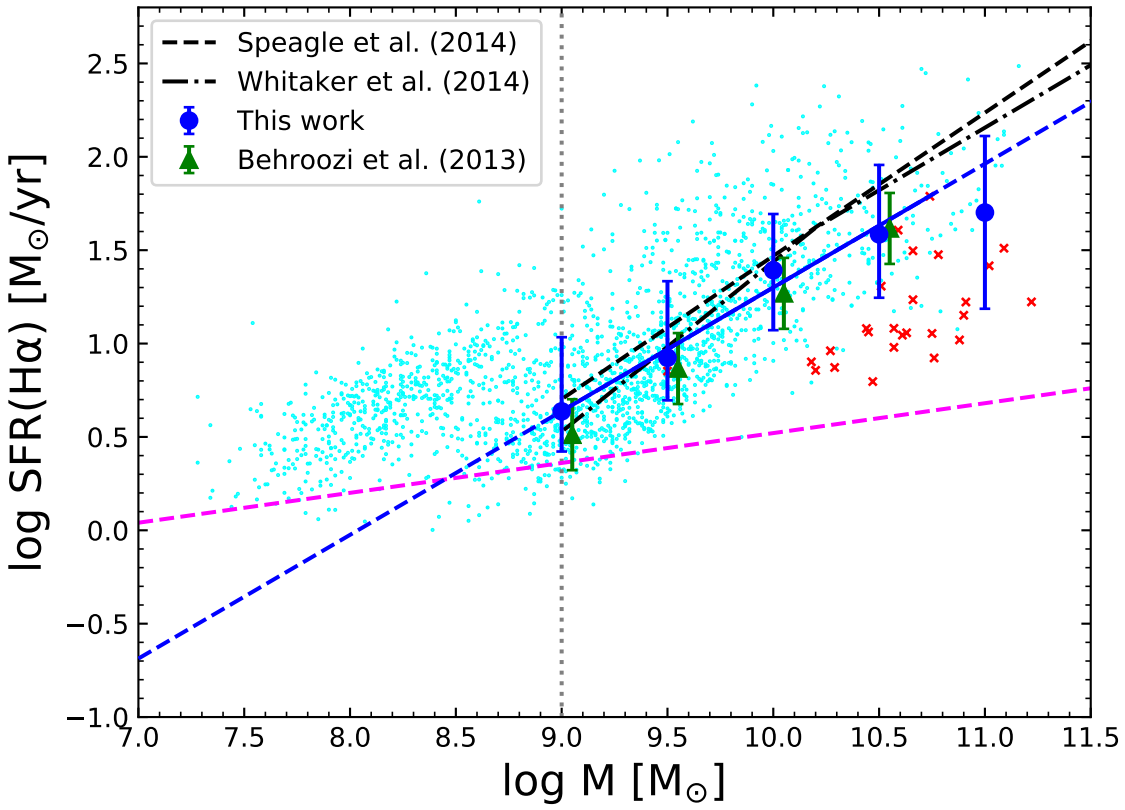

Figure 3.17: Hα star formation main sequence (SFMS) of our sample. The cyan circles represent individual galaxies while the blue circles show median values in each stellar mass bin. By fitting in the range of $9 < \log M < 11$, we obtain the best-fit SFMS shown by the blue line. The green triangles are the typical values among many previous studies with various wavelengths, which are summarized in Behroozi et al. (2013). The black dashed and dash-dotted lines indicate the best-fit SFMSs of Speagle et al. (2014) and Whitaker et al. (2014), respectively. The red crosses represent the quiescent Hα emitters with well-constrained SEDs classified by the UVJ diagram. The dotted grey vertical line shows the stellar mass completeness limit of our sample while the dashed magenta line is the SFR limit of our sample corresponding to the flux excess threshold to be selected as the Hα emitters.

dusty starburst systems rather than normal galaxies on the SFMS (Rodighiero et al. 2011, Lee et al. 2013). On the other hand, Hα emitters cover diverse populations with various properties (Oteo et al. 2015). Hence our Hα emitters represent a less-biased population, where even very weak emission line galaxies are included.

3.5.2 Low-mass galaxies with high sSFR

At $\log M/M_{\odot} > 9$, we find that the scatter around the SFMS is ~ 0.31 dex, where it is defined as the standard deviation of SFR offsets of individual galaxies from the SFMS. This value agrees well with previous observations and support the "self-regulated" evolution of Tacchella et al. (2016).

At $\log M/M_{\odot} < 9$, however, there are many low-mass galaxies with much higher SFRs than predicted from the extrapolation of the SFMS. We should note, of course, that only strong Hα emitters can be detected in the low-mass end due to the sensitivity limit of the $K_{\rm s}$-band of the ZFOURGE. Hence we can never know any statistical properties of the low-mass star-forming galaxies. Nevertheless it is still interesting to investigate the low-mass Hα emitters in our sample further because the high sSFRs may suggest their bursty SFHs.

Before investigating their SFHs, we evaluate impacts of the photometric errors in the data on the sSFRs of the low-mass galaxies. Since contributions of the errors are more significant to the faint galaxies, it might be possible that the observed high sSFRs of the low-mass galaxies are caused by the errors in their Hα fluxes. To check this effect, we perform a simulation as follows. First we generate 100,000 galaxies with stellar masses of $\log M/M_{\odot} = 7.0$–10 following the stellar mass function of Tomczak et al. (2014). Their SFRs are calculated by Equation 3.14, where we assume that the SFMS is held even at the low-mass end. Then we add fluctuations to the SFRs based on the photometric errors in the $K_{\rm s}$-band. Scatters around the SFMS increase with decreasing stellar masses as shown in Figure 3.18. Next we derive probability distributions of the scatters in different stellar mass bins so that we can estimate how much the scatters might be explained by the SFR fluctuations due to the photometric errors. As a result, we find that the scatters of $\gtrsim 0.5$ dex can be hardly caused by only the errors. On the

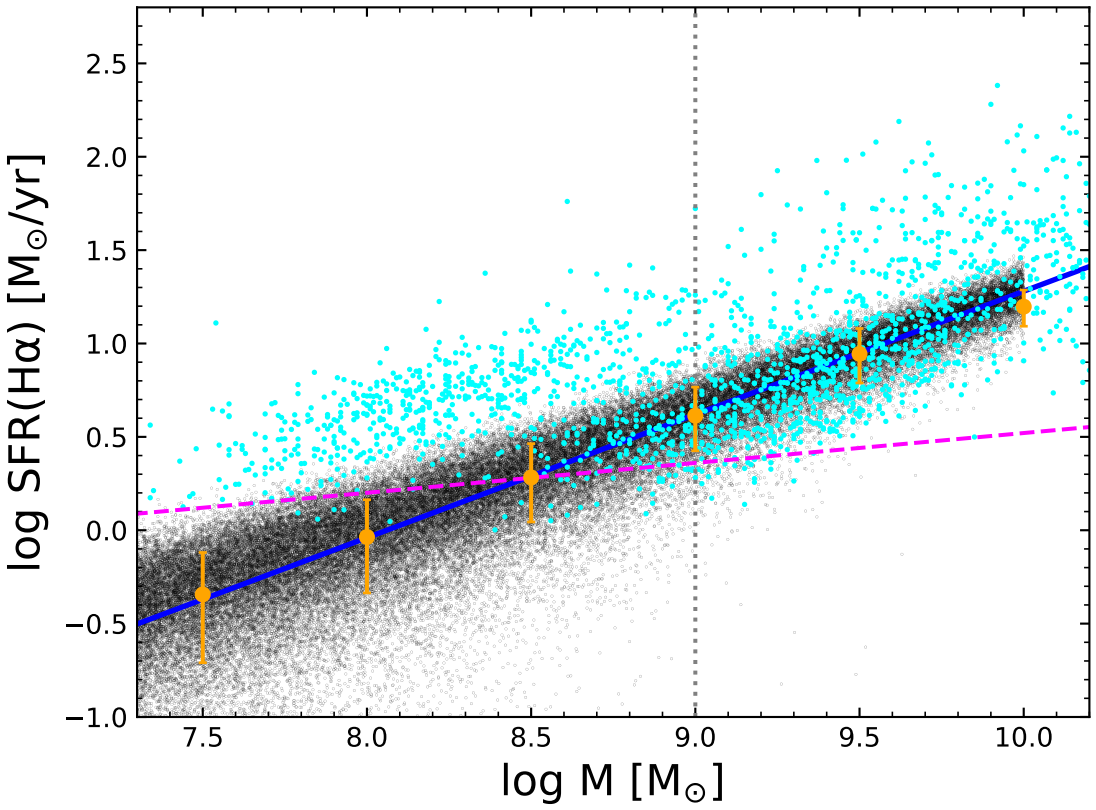

Figure 3.18: Scatters around the SFMS caused by the photometric errors. The cyan circles represent individual Hα emitters in our sample, while the blue line shows the SFMS extrapolated toward the low-mass end. The black dots represent the simulated galaxies following the stellar mass function of Tomczak et al. (2014). Their Hα SFRs are fluctuated based on the photometric errors in the K_s-band. The orange circles are median SFRs of the simulated galaxies in each stellar mass bin. The dotted grey vertical line and the dashed magenta line are the same as Figure 3.17.

other hand, more than 300 galaxies with $\log M/M_{\odot} < 9.0$ have the observed scatters larger than 0.5 dex. Therefore we conclude that the low-mass galaxies with the high sSFRs are really starburst galaxies.

3.5.3 Hα/UV ratio

If a galaxy has undergone an instantaneous starburst within past 100 Myr, its luminosity ratio between Hα and UV is expected to be different from those predicted for galaxies forming stars at a constant rate (Sparre et al. 2017, Faisst et al. 2019). Due to the different characteristic timescales of the Hα emission line and the UV continuum, the Hα luminosity responds to the instantaneous burst more quickly than the UV. As a consequence, when a short starburst occurs at a moment, the Hα/UV ratio is higher than that expected in a constant SFH during first 10 Myr after the burst. On the other hand, the ratio is suppressed during 10–100 Myr after the burst. Therefore, if the high sSFRs of the low-mass galaxies have been caused by recent starbursts, they should also have high Hα/UV ratios.

Figure 3.19 shows a comparison of the Hα luminosities and the UV luminosities of our Hα emitters, where both have been corrected for the dust attenuation following the procedure of § 2.4.3. The grey line represents the expected relation when assuming a constant SFH (Faisst et al. 2019) and the shaded area shows $\pm$0.3 dex intervals. It is obvious that most of the galaxies with $\log M < 9.0$ have very high Hα/UV ratios, which can not be explained by a constant SFH. On the other hand, few massive galaxies show such high ratios, which is NOT due to the completeness issue. Figure 3.20 makes it clear that the low-mass galaxies with much above the SFMS correspond to the population with high Hα/UV ratios. These facts suggest that the low-mass Hα emitters with high sSFRs we discovered are the galaxies which recently have experienced short period starbursts.

3.5.4 SFHs of the starburst galaxies

Although there are also high-mass galaxies with high sSFRs, their Hα/UV ratios do not seem high in contrast to the low-mass ones as shown in Figure 3.20. This

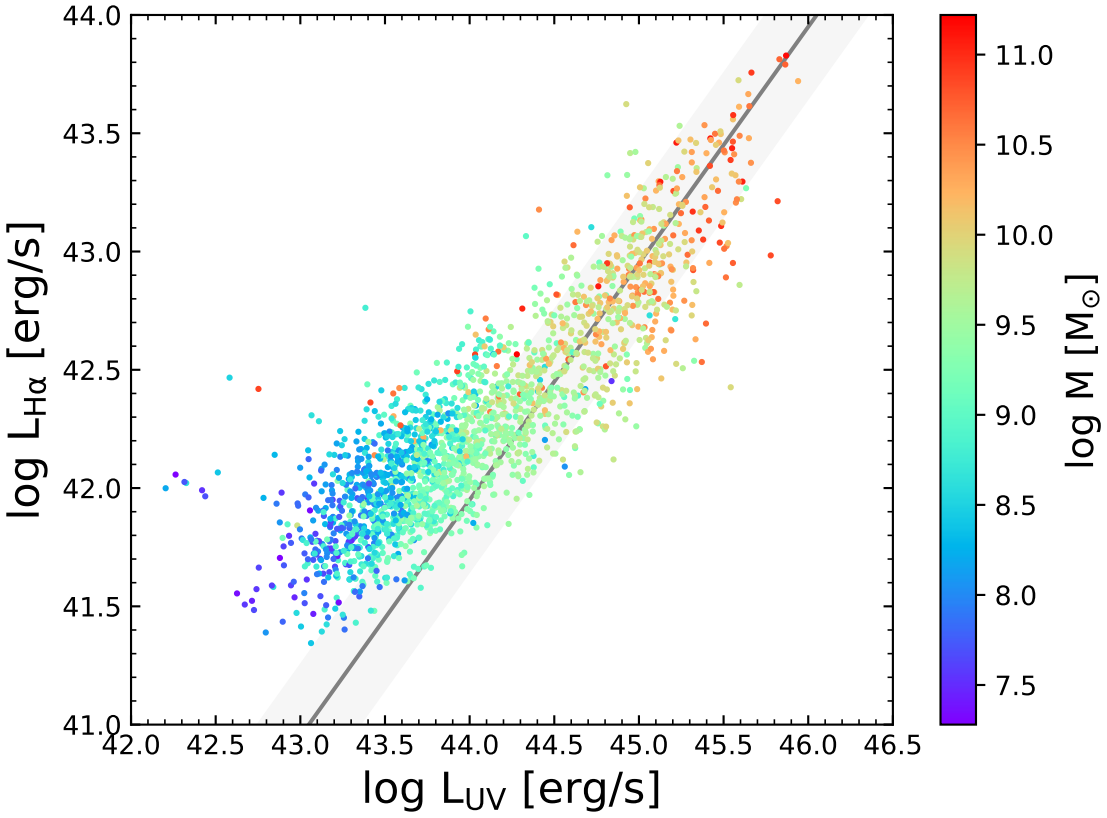

Figure 3.19: Comparison between the Hα and UV luminosities, which are both corrected for the dust attenuation. The color coding reflects stellar masses of the galaxies. The grey line shows the expected relation from a constant SFH without starbursts within 100 Myr (Faisst et al. 2019), while the shaded region indicates ±0.3 dex intervals.

may suggest that starburst galaxies with different stellar masses have different SFHs. In other words, mechanisms which cause the starbursts may be different depending on stellar masses of the galaxies. To investigate it more quantitatively, we define the starburst galaxies as the galaxies with SFRs larger than those expected from the SFMS by 0.3 dex. Then we measure the Hα/UV ratio in each stellar mass bin to examine its mass dependence. Figure 3.21 shows the Hα/UV ratios of the starburst galaxies as a function of stellar mass. It is clear that median values of the Hα/UV decrease with increasing the stellar masses and reach the value expected from a constant SFH. As mentioned above, high Hα/UV ratios imply bursty SFHs of galaxies, where the

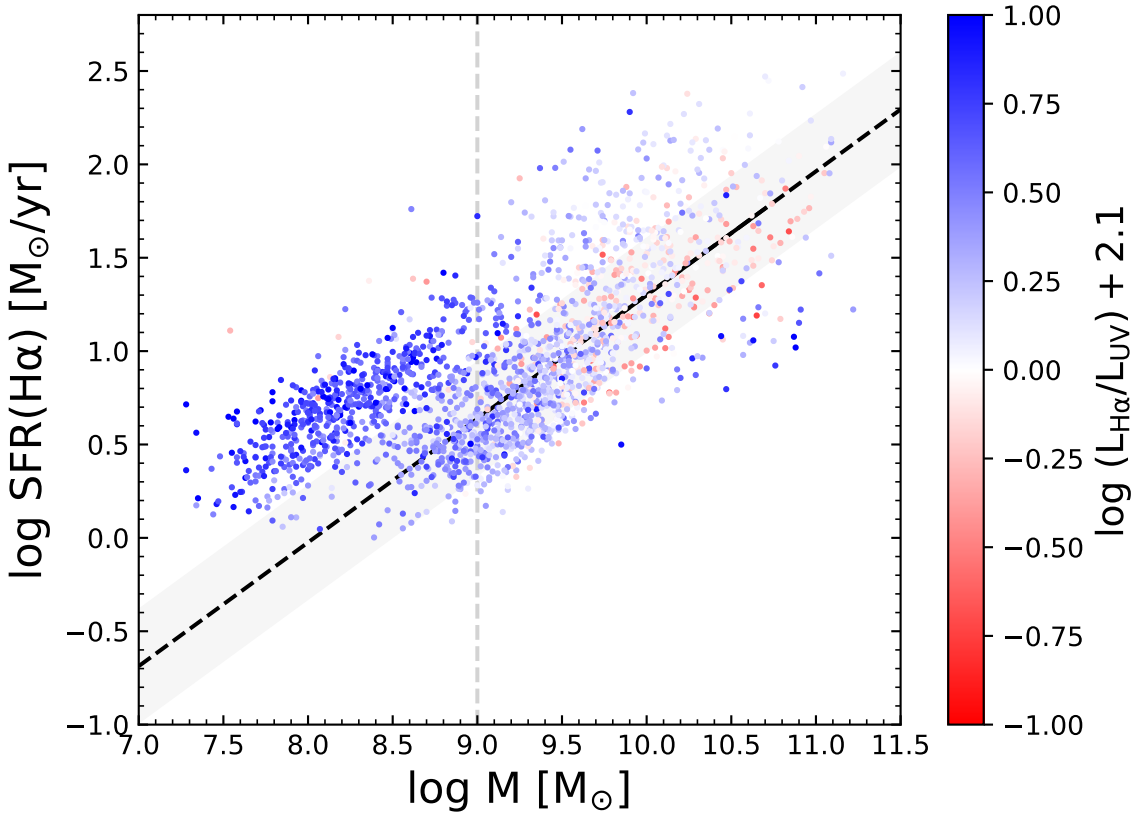

Figure 3.20: The same SFMS as Figure 3.17, but color-coded based on the Hα/UV luminosity ratios. The grey shaded region indicates ±0.3 dex intervals around the best-fit SFMS and its extrapolation toward the low-mass and high-mass ends.

starbursts occurred within past $\sim$ 10 Myr. Therefore the trend shown in Figure 3.21 indicates that there are at least two different types of the starburst. One is a burst with a short duration, which is dominant in the low-mass galaxies, causing the high Hα/UV ratios. The other is a burst with a longer duration, which is dominant in the high-mass galaxies, resulting in constant SFHs during $>$ 10 Myr. Although it is beyond the scope of this thesis to reveal specific mechanisms which govern the starbursts in each stellar mass bin, there have been several events which are expected to cause the starbursts such as supernova feedbacks, gas inflows, and major mergers.

It is important to understand if there are any selection effects in the Hα/UV ratios of the starburst galaxies and how they can affect the result. Especially, as our sample

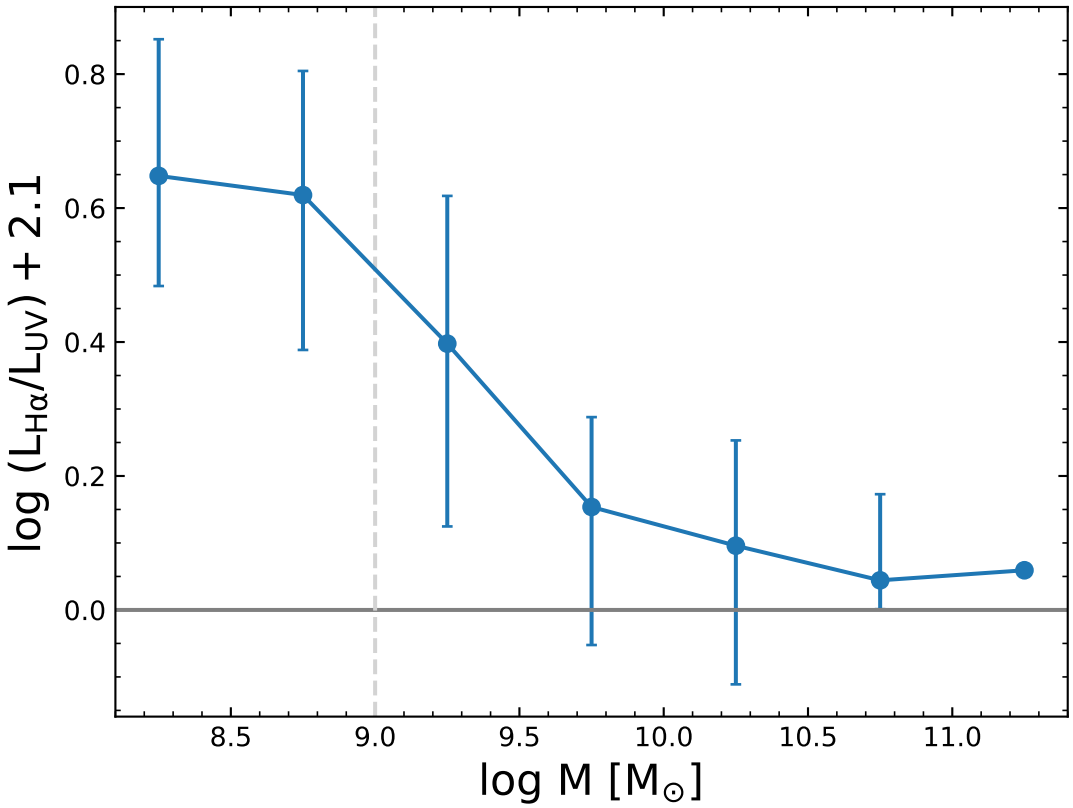

Figure 3.21: Hα/UV ratios of the starburst galaxies as a function of stellar mass. The blue circles represent median values in each stellar mass bin. The grey horizontal line shows the value expected from a constant SFH, while the dashed vertical line indicates the stellar mass completeness limit.

is mass incomplete at $\log M/M_\odot < 9.0$, we have to carefully interpret the measurements for the low-mass galaxies. Figure 3.22 shows the Hα/UV ratios of the starburst galaxies in each stellar mass bin. In the lowest two mass bins, where the stellar mass completeness is insufficient, the ratios are clearly higher than those expected from a constant SFH as already mentioned above. Now our concern is whether any selection effects cause the apparent trend or this is an intrinsic characteristic of the low-mass starburst galaxies. The Hα/UV ratios in the bins can be overestimated if UV-faint galaxies at fixed Hα luminosities are exclusively selected and/or Hα-bright galaxies at fixed UV luminosities are exclusively selected. The former is unlikely because there should be no anti-correlation between the K_s-band magnitudes and the UV luminosi-

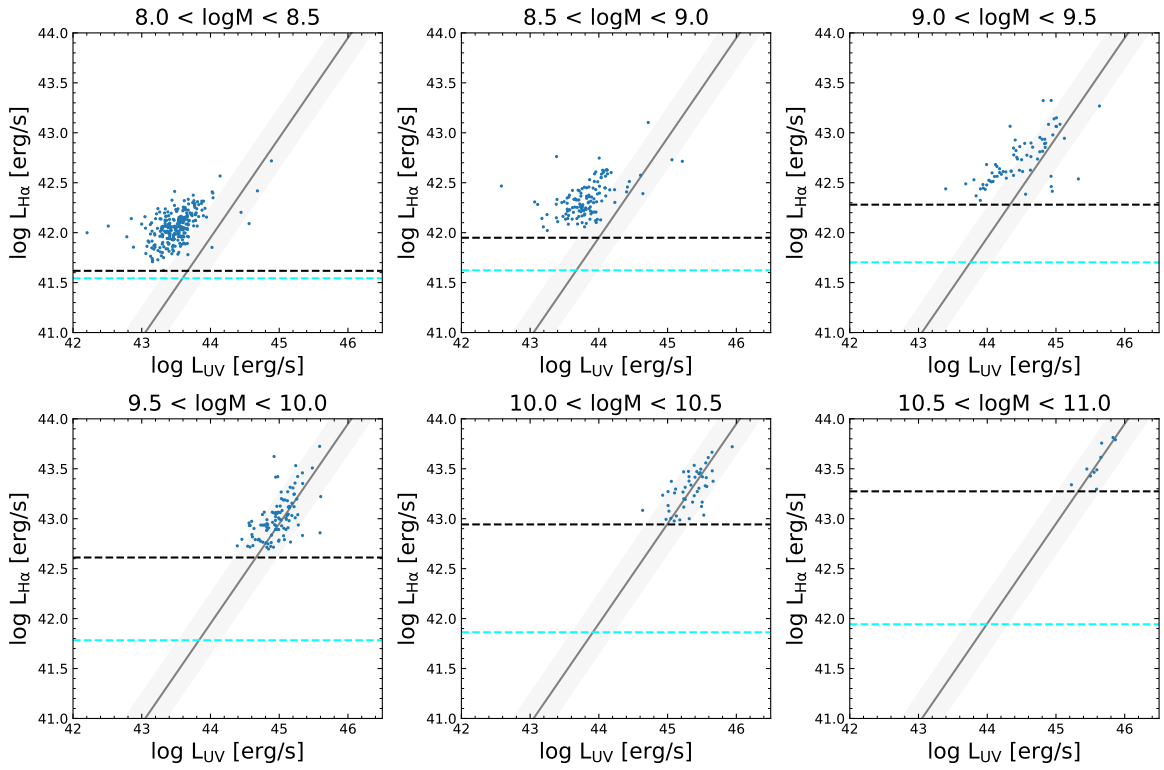

Figure 3.22: Comparisons of the Hα and the UV luminosities of the starburst galaxies, where Figure 3.19 is divided into the six bins. Each dashed black horizontal line represents the threshold of the Hα SFR to be classified as the starburst galaxies in our definition. Each dashed cyan horizontal line shows the SFR limit to be selected as the Hα emitters.

ties. The latter can be important when discussing the ratios of the whole Hα emitter sample. However, we are focusing on only the starburst galaxies most of which are expected to have enough Hα luminosities (SFRs) to be selected as the Hα emitters in all the bins. Hence the impact of the bias toward luminous Hα emitters on the Hα/UV ratios seems insignificant. We conclude that the trend in Figure 3.21 is real so that dominant mechanisms of the starbursts can vary with stellar masses of the galaxies.

Chapter 4

Properties of [OIII] emitters at $z = 2.1$–2.5

In this chapter, we investigate properties of the galaxies at $2.1 < z < 2.5$ showing the flux excesses in the two medium-band filters ($H_{\rm s}$ and $H_{\rm l}$) of the ZFOURGE. In this redshift range, [OIII] (rest-frame 4959 & 5007 Å) and Hβ (rest-frame 4861 Å) emission lines fall into these bands. Hence the galaxies with $H_{\rm s}$ or $H_{\rm l}$ excesses are candidates of [OIII](+Hβ) emitters.

[OIII] line strengths and their ratios to other lines are closely related to physical properties of galaxies. For example, a ratio between [OIII]$\lambda\lambda$4959, 5007 and [OII]$\lambda\lambda$3727, 3729, also known as the O_{32} index, has been used as a proxy of ionization parameters in previous studies. (e.g., Sanders et al. 2015, Khostovan et al. 2016, Nakajima & Ouchi 2014, Reddy et al. 2018). They have found a general trend that the [OIII]/[OII] increases with redshift up to $z \sim 3$ suggesting an enhancement of ionization parameters at high-z. Under assumptions of ionization equilibrium in HII regions modeled by Strömgren spheres, the ionization parameters depend on ionizing photon production rates, electron densities, and filling factors of the HII regions (Sanders et al. 2015). Using the spectroscopic data taken by the MOSDEF survey, Sanders et al. (2015) has argued that the enhanced [OIII]/[OII] at high-z reflects redshift evolution of the mass metallicity relation, where high-z galaxies have lower metallicities than those in the local universe (e.g., Hayashi et al. 2009, Mannucci et al. 2010, Yabe et al. 2015). Since low-metallicity stars produce more ionizing photons (Leitherer et al. 2014), the ionization parameters increase with decreasing metallicities.

Regarding the [OIII] strength itself, Reddy et al. (2018) have found that [OIII] equivalent widths increase with increasing sSFRs and decreasing metallicities. This is because higher sSFRs result in more ionizing photons produced in unit time while lower metallicities lead to more ionizing photons produced per unit SFR. In addition, they have shown that the [OIII] equivalent width has the strongest dependence on stellar mass among rest-frame optical emission lines, where [OIII] is more prominent in lower-mass galaxies.

These observational trends of the [OIII] emission line suggest that strong [OIII] emitters represent a unique population characterized by low stellar masses, low metallicities, high sSFRs, and high ionization parameters. Such a population is important to understand evolution of galaxies at early (young) phases.

Moreover, the most extreme [OIII] emitters have been related to large escape fractions of the ionizing photons. Nakajima & Ouchi (2014) have found that local galaxies showing large escape fractions have much higher [OIII]/[OII] ratios than those of normal galaxies. Hence they have suggested a possibility that high-z galaxies with high [OIII]/[OII] ratios are candidates of galaxies from which the ionizing photons escape. On the other hand, it has been known that galaxies with the largest [OIII] equivalent widths have occupied the upper left region of the BPT diagram (Baldwin et al. 1981), where galaxies with large Lyα equivalent widths have also lain (Erb et al. 2014, Trainor et al. 2016). This result also relate such strong [OIII] emitters to the large escape fractions, since the galaxies with large Lyα equivalent widths tend to show the large values (e.g., Reddy et al. 2016, Steidel et al. 2018). Large escape fractions of the ionizing photons have been thought to be a characteristic of star-forming galaxies at higher-z, which contribute the re-ionization of the universe.

The results of the previous works mentioned above motivate us to verify our method for [OIII] emission lines as well as for Hα to construct a large sample of the [OIII] emitters, which can help us understand the important populations of the star-forming galaxies.

4.1 Sample description

We select the [OIII](+Hβ) emitter candidates from 3320 galaxies at $2.1 < z < 2.5$, which is the same parent set as we used for the Hα emitter selection. Here we remove the identified 38 AGNs from our analysis for simplicity. By applying the threshold described in § 2.2, we obtain 1464 [OIII] emitters (623 and 841 from the $H_{\rm s}$ and $H_{\rm l}$-band, respectively). Among them, 1137 (78%) [OIII] emitters have been also selected as the Hα emitters, which we call "dual emitters". For the dual emitters, we can estimate contributions of Hβ fluxes to the total flux excesses using the Hα information (see § 2.2).

Figure 4.1 shows stellar mass distributions of the (single) [OIII] emitters and the dual emitters. We will investigate what kind of populations both the single and dual emitters are in § 4.4, but it should be noted that the discrepancy between the two distributions in Figure 4.1 around $\log M = 9.0$ is probably not real. This is explained by some factors. First, the pair of $H_{\rm s}$ and $H_{\rm l}$ medium-band filters covers a wider redshift range than the $K_{\rm s}$ broad-band filter (Figure 2.1). Thus it is possible that galaxies outside the target redshift range may contaminate our sample due to the photo-z uncertainties. Such galaxies can show the flux excesses only in the $H_{\rm s}/H_{\rm l}$-band even if they also have strong Hα emissions. However, given that the photo-z uncertainties of our sample are very small compared to the redshift window of the $K_{\rm s}$-band filter thanks to the medium-band filters of the ZFOURGE (see § 2.1), such a contamination is expected to be at most less than 10%. On the other hand, it seems that a combination of the stellar mass completeness and the different sensitivities to the two emission lines mainly causes the different shapes of the two distributions. Since the ZFOURGE catalog is 80% complete at $\log M/M_{\odot} \sim 9$, only strong emitters are detected in the $K_{\rm s}$-band below this limit. Hence the number of emitters decreases with decreasing stellar masses at $\log M/M_{\odot} < 9$. In addition, the equivalent width completeness of Hα strongly depends on stellar mass if assuming the typical value of Reddy et al. (2018) (see § 3.2.1), which quickly reduces the number of the low-mass dual emitters, while the stellar mass dependence of the [OIII] equivalent width is more moderate as we will see in the next section. However, as shown in Figure 3.7, there

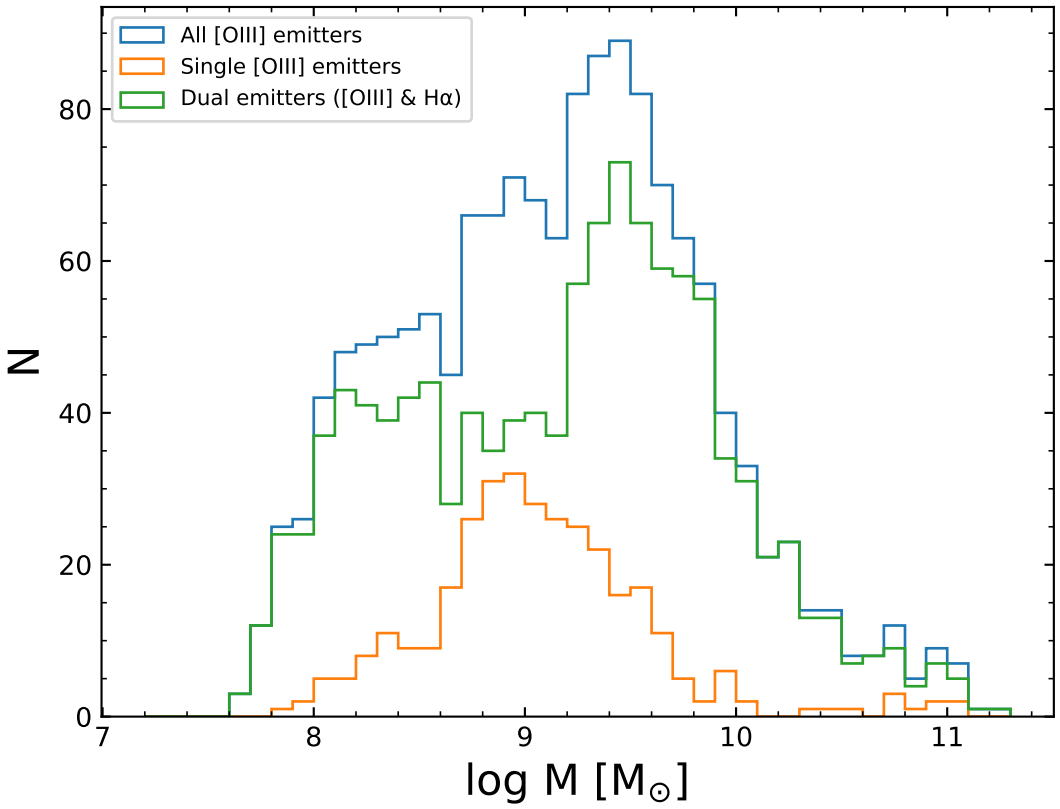

Figure 4.1: Stellar mass distribution of our [OIII] emitters (blue). We also show the distributions of the two sub-populations, the single [OIII] emitters and the dual emitters, in orange and green, respectively.

are many lowest-mass ($\log M/M_\odot < 8.5$) galaxies with extremely large Hα equivalent widths. These populations likely form the second peak of the dual emitter distribution. We will investigate dual emitter fractions in our sample more quantitatively in § 4.4.

At $2.26 < z < 2.36$, Hβ falls into the H_s-band while [OIII]λ5007 falls into the H_l-band. 357 emitters in our sample are in this redshift range and they are all selected by only the flux excesses in the H_l-band probably because their Hβ fluxes are not strong enough to produce significant flux excesses alone. As their flux excesses totally consist of [OIII], though there are the small photo-z uncertainties, we correct the excesses to the total values (i.e., [OIII]+Hβ). Using other H_l-band excess galaxies outside $2.26 < z < 2.36$, we find a median [OIII]/Hβ of ~ 5.4. Then the flux excesses of the emitters at $2.26 < z < 2.36$ are corrected with this ratio. We should note that this

correction does not affect our results shown in the following sections. In addition, we ignore a possibility that [OIII]λ4959 and [OIII]λ5007 fall into different filters because the redshift difference of the two lines is smaller than the photo-z uncertainties.

4.2 Equivalent widths

In this section, we investigate equivalent widths of the galaxies with the flux excesses in the $H_{\rm s}/H_{\rm l}$-band. Here we assume that the flux excesses consist of only [OIII]λ4959, [OIII]λ5007, and Hβ emission lines and ignore other lines because they are very weak.

4.2.1 Limiting equivalent widths

First, we check the limiting equivalent width of our [OIII](+Hβ) emitters in the same way as we did for the Hα emitters in § 3.2.1. Figure 4.2 shows it as a function of stellar mass, which is given by

$$\log EW_{\rm lim}([{\rm OIII}]+{\rm H}\beta) = -0.52 \log M/M_{\odot} + 6.97. \tag{4.1}$$

This limit is higher than that of the Hα equivalent width (§ 3.2.1), which is probably due to larger photometric errors in the $H_{\rm s}/H_{\rm l}$-band than those in the $K_{\rm s}$-band. However, if assuming the distribution of Reddy et al. (2018), the completeness is still larger than 85% at $\log M/M_{\odot} > 9$.

4.2.2 Stellar mass dependence

Figure 4.3 shows the equivalent widths of our sample as a function of stellar mass. By fitting the galaxies above $\log M/M_{\odot} = 9$, we obtain the best-fit relation as follows:

$$\log EW([{\rm OIII}]+{\rm H}\beta) = -0.42 \log M/M_{\odot} + 6.39. \tag{4.2}$$

Our result is consistent with a previous spectroscopic result (Reddy et al. 2018), though slightly lower than a result from the HiZELS (Khostovan et al. 2016). If we select the galaxies which have the flux excesses both in the $K_{\rm s}$ and $H_{\rm s}/H_{\rm l}$-band (i.e., dual emitters), a very similar best-fit relation between the [OIII] equivalent widths and the

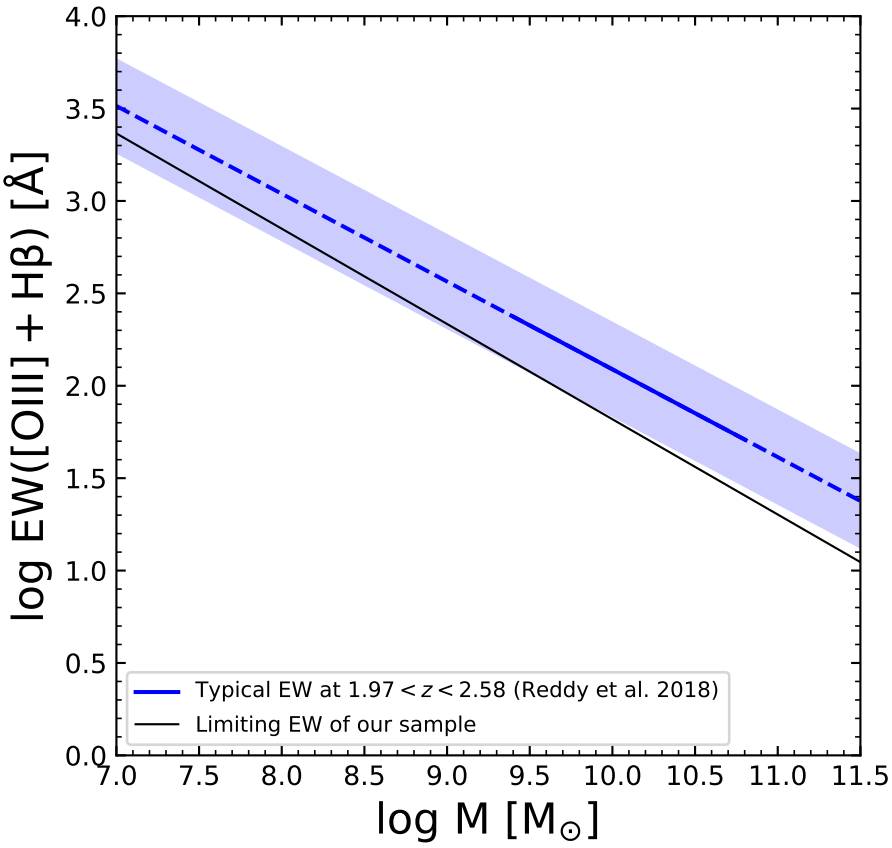

Figure 4.2: Limiting equivalent width of [OIII]+Hβ as a function of stellar mass (black solid line). The blue line and intervals show the typical [OIII]+Hβ equivalent width and its scatter reported by Reddy et al. (2018) for the galaxies with $\log M \simeq 9.3$–10.7. As the stellar mass dependence of [OIII]+Hβ is stronger than that of Hα, our selection may miss part of the emitters even above the stellar mass completeness limit ($\log M > 9$).

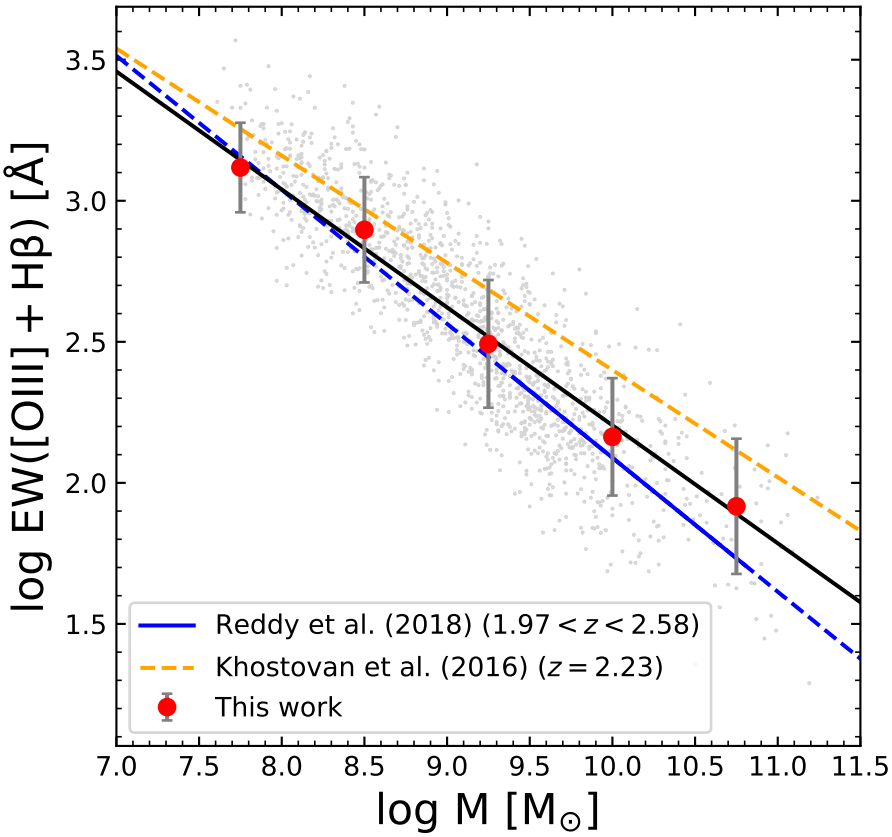

Figure 4.3: [OIII]+Hβ equivalent width as a function of stellar mass. The grey circles represent individual galaxies, while the red circles show median values in each stellar mass bin. The best-fit relation is obtained by fitting the medians in the range of $\log M/M_{\odot} > 9$ (black line). The blue line and the dashed yellow line indicate the best-fit relations reported by Reddy et al. (2018) and Khostovan et al. (2016), respectively.

stellar masses is found, which is given by

$$\log EW([\mathrm{OIII}]) = -0.44 \log M/M_{\odot} + 6.46, \tag{4.3}$$

where the contributions of Hβ to the $H_{\mathrm{s}}/H_{\mathrm{l}}$-band flux excesses are estimated from the dust-corrected Hα luminosities (Figure 4.4). This suggests that the flux excesses in the $H_{\mathrm{s}}/H_{\mathrm{l}}$-band are dominated by the [OIII] emission lines as we will show later.

As shown above, the [OIII] equivalent widths depend on the stellar masses more strongly than those of Hα for which the slope of the best-fit relation is -0.24 (see § 3.2.2). More interestingly, the median equivalent widths of our [OIII] emitters agree

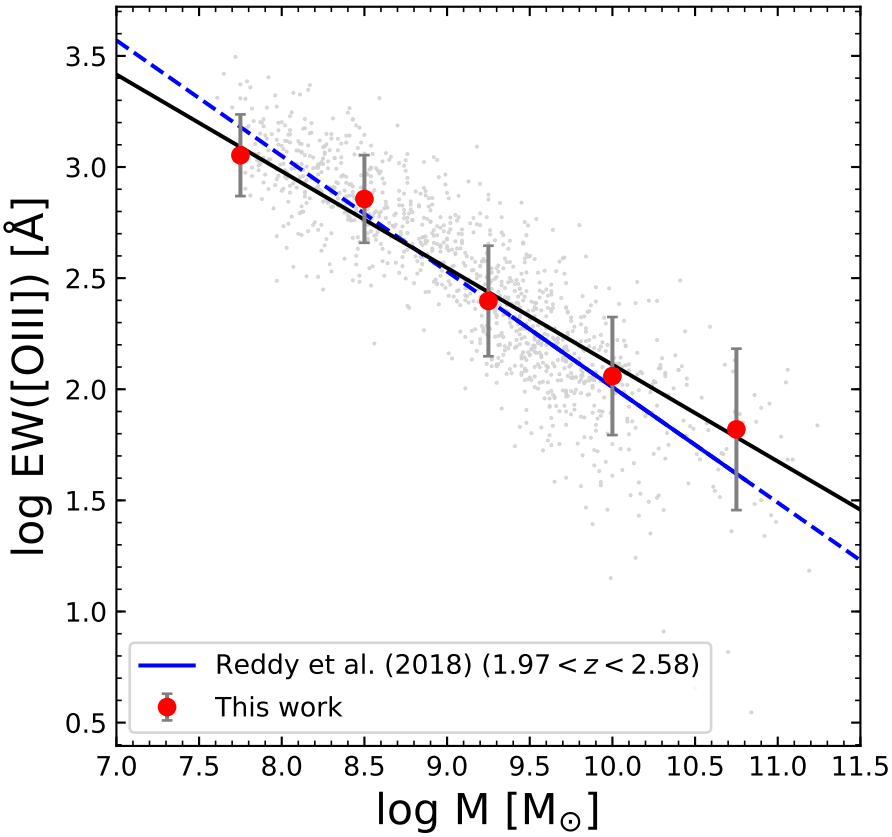

Figure 4.4: [OIII] equivalent widths of the dual emitters as a function of stellar mass, which are obtained by subtracting the Hβ contributions from the [OIII] + Hβ equivalent widths. We estimate the Hβ contributions using the Hα fluxes derived from the K_s-band flux excesses. The color coding is the same as Figure 4.3.

well with an extrapolation of the best-fit relation even in $\log M/M_\odot < 9$, where the extreme ones are selected as the Hα emitters (Figure 3.7). This might suggest that the low-mass [OIII] emitters represent the galaxies with very high sSFRs.

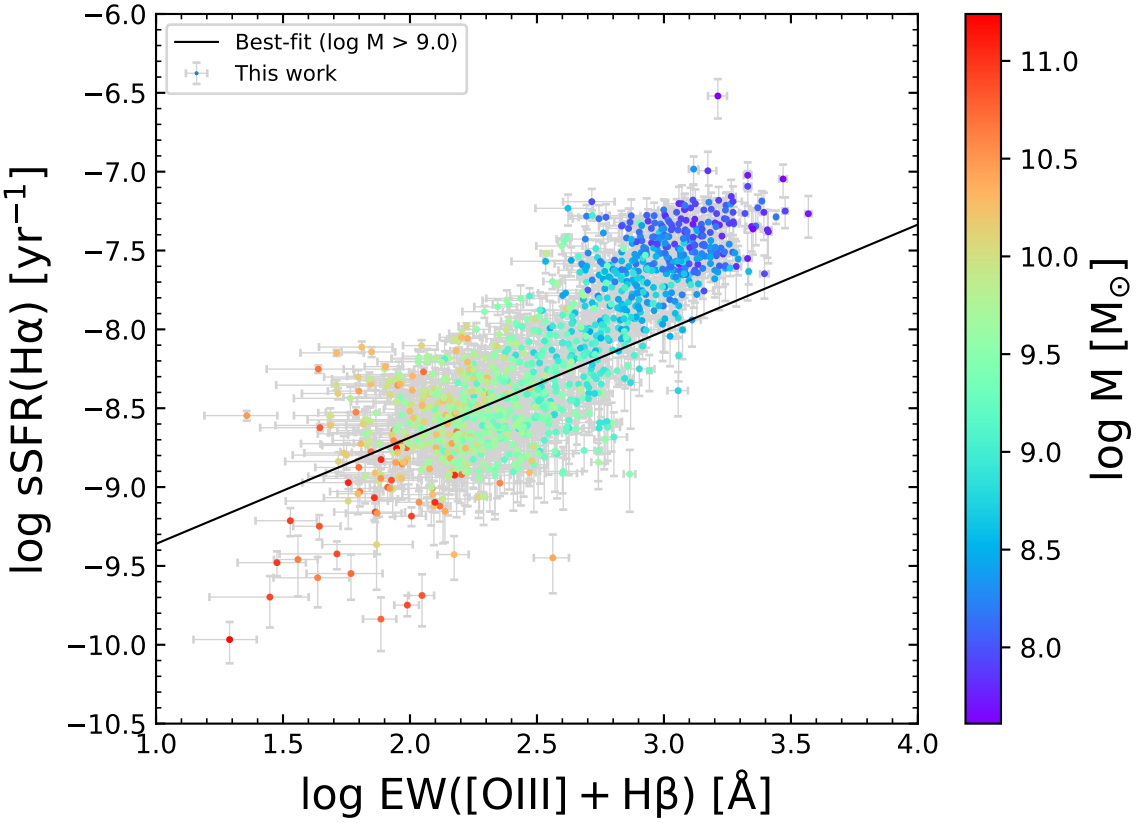

Figure 4.5: Hα sSFRs of the dual emitters as a function of [OIII]+Hβ equivalent width. Individual galaxies are color-coded based on their stellar masses. The black line shows the best-fit relation obtained by fitting only the galaxies with $\log M/M_\odot > 9$.

4.3 Correlation of [OIII] with other properties

4.3.1 Hα sSFR

Figure 4.5 shows sSFRs measured from the Hα luminosities as a function of equivalent width of [OIII]+Hβ, where only the dual emitters are included. It is clear that their equivalent widths strongly depend on the Hα sSFRs, where the best-fit relation above $\log M/M_\odot > 9$ is given by

$$\log \mathrm{sSFR}(\mathrm{H}\alpha) = 0.67 \log EW([\mathrm{OIII}] + \mathrm{H}\beta) - 10.0. \quad (4.4)$$

The sSFR dependence of the [OIII](+Hβ) equivalent widths can be explained by increasing ionizing photon production rates with SFRs at fixed stellar masses as suggested in Reddy et al. (2018). Similarly, the anti-correlation with the stellar masses can be interpreted as a reflection of the decreases of the metallicities with decreasing stellar masses, which lead to harder (bluer) ionizing spectra. Both effects result in larger [OIII] equivalent widths. Therefore it is reasonable that the low-mass galaxies with the highest sSFRs show the largest [OIII] equivalent widths. In other words, we may be able to find candidates of galaxies with such extreme properties by selecting the strongest [OIII] emitters, for example, with $EW([\mathrm{OIII}] + \mathrm{H}\beta) > 1000$ Å.

In addition, the fact that the galaxies with the highest Hα sSFRs (i.e., highest equivalent widths) also have the highest [OIII] equivalent widths indicates the high reliability of our emitter selection based on the flux excess.

4.3.2 [OIII]/Hβ

Figure 4.6 shows a correlation between the [OIII]+Hβ equivalent widths and [OIII]λ5007/Hβ ratios, which can be fitted by

$$\log\left([\mathrm{OIII}]\lambda5007/\mathrm{H}\beta\right) = 0.39 \log EW([\mathrm{OIII}] + \mathrm{H}\beta) - 0.45. \quad (4.5)$$

As expected from connections between the [OIII] equivalent widths and the locations on the BPT diagram found in previous studies, we find that the [OIII]λ5007/Hβ ratios increase with the [OIII]+Hβ equivalent widths. Although precise locations on the BPT diagram also depend on [NII]/Hα ratios, we can expect the strongest [OIII] emitters to occupy the same locations as strong Lyα emitters given that the [NII]/Hα ratios, which are sensitive to metallicities, are generally lower in low-mass (i.e., high equivalent width) galaxies.

4.3.3 Dust attenuation

Figure 4.7 shows a correlation between the [OIII]+Hβ equivalent widths and the amounts of the dust attenuation derived from the SED fitting. It is clear that the stronger [OIII] emitters are less obscured by the dust. This trend is reasonable given that the dust attenuation correlates with the SFR (§ 3.3). As shown in Figure 4.3,

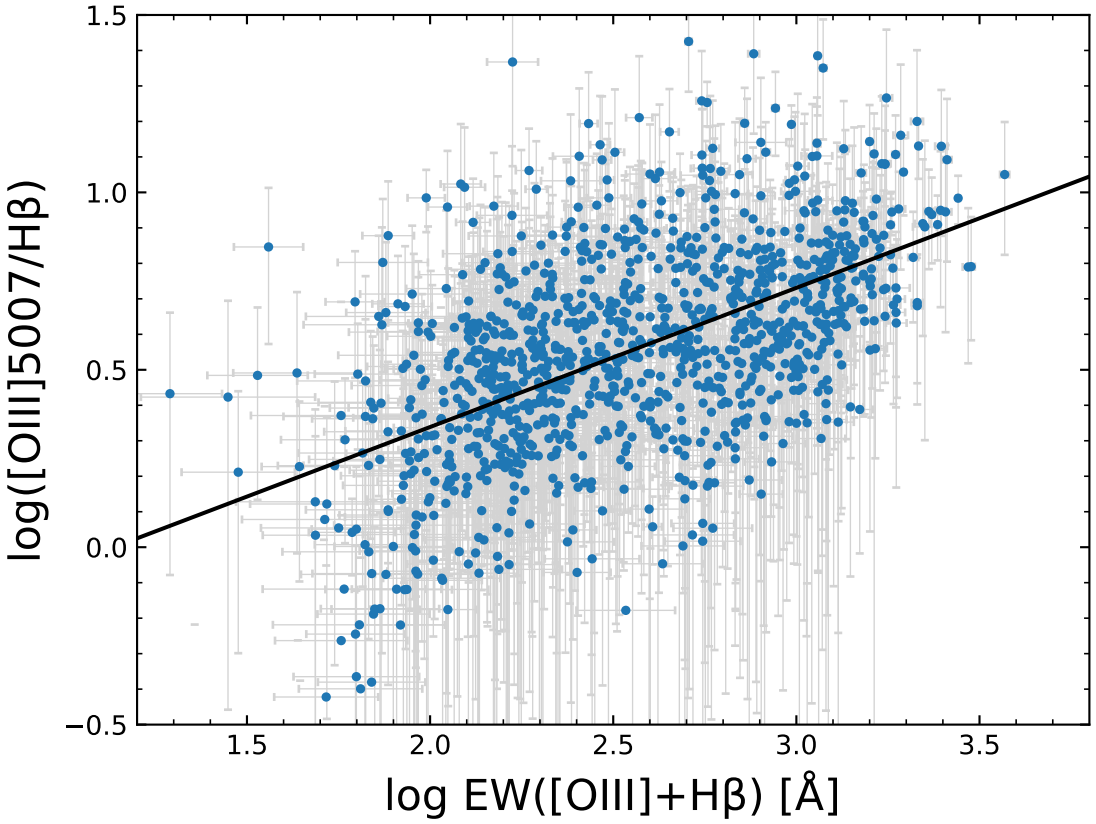

Figure 4.6: [OIII]λ5007/Hβ as a function of [OIII] + Hβ equivalent width. The blue circles represent individual dual emitters in our sample, while the black line shows the best-fit relation.

the lower mass galaxies have higher equivalent widths. Since such low-mass galaxies generally have lower SFRs (not sSFRs) compared to the more massive ones, the A_V values have the equivalent width dependence seen in Figure 4.7.

4.3.4 Ionization parameter

Unfortunately we cannot argue ionization parameters of our sample due to a lack of [OII] information. Nevertheless, we can infer that the low-mass galaxies with the highest [OIII] equivalent widths are expected to have large ionization parameters, which is due to the different stellar mass dependences of [OII] and [OIII]. According to Reddy et al. (2018), [OII] equivalent widths do not significantly vary with stellar

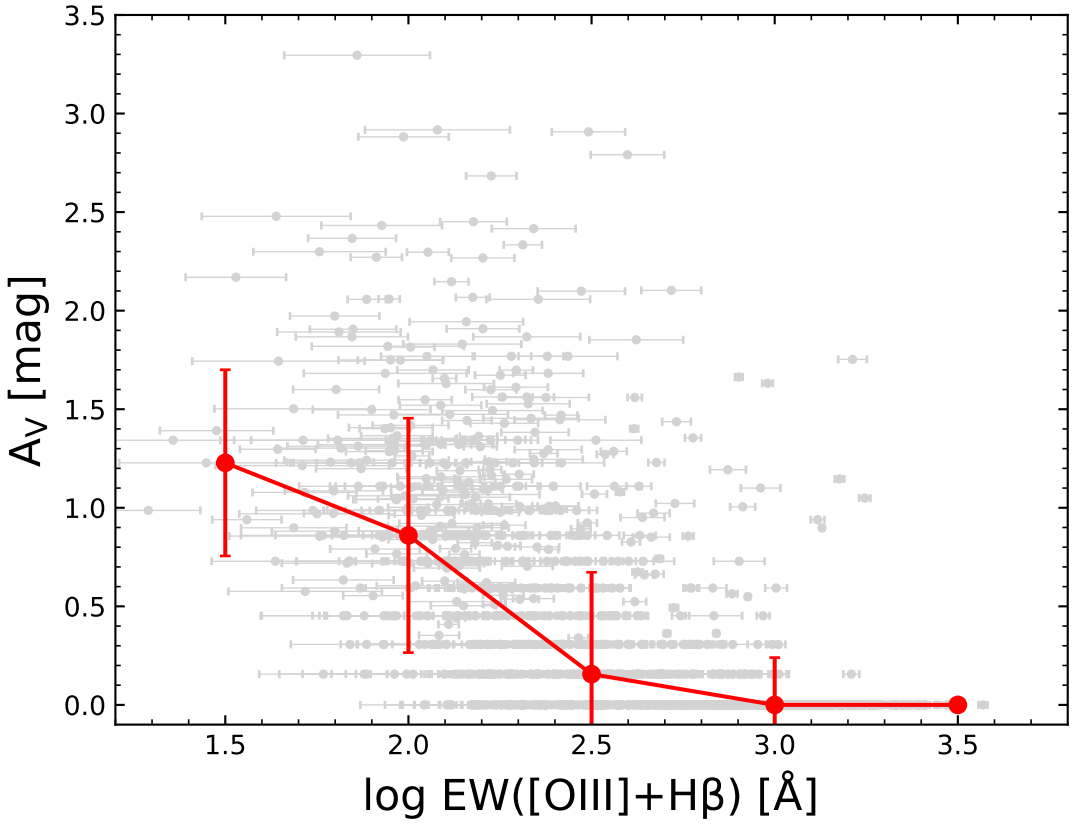

Figure 4.7: The amount of the dust attenuation (A_V) as a function of [OIII] + Hβ equivalent width for the dual emitters. The grey circles represent individual galaxies while median values in each bin are shown in red.

masses, where the best-fit slope is -0.171. On the other hand, as we have also shown, the [OIII] equivalent widths depend much strongly on the stellar masses. Hence, if assuming a constant [OII] strength through the entire stellar mass range, the [OIII]/[OII] ratio increases with decreasing the stellar mass. Since large [OIII]/[OII] ratios are one of characteristics of the local galaxies with large escape fractions, the low-mass [OIII] emitters in our sample might be interesting targets for future observations to understand ionizing photon escapes at $2.1 < z < 2.5$

4.3.5 Hα luminosity

Suzuki et al. (2016) have suggested a possibility to use the [OIII] luminosity as a SFR indicator for high-z galaxies. It is observable in the NIR wavelength range even at $z \gtrsim 3$, where redshifted Hα can no longer be observed with ground-based instruments. In addition, the increasing [OIII]/[OII] with redshifts and its relative robustness against the dust absorption encourage the use of [OIII] rather than [OII] for the SFR estimates at high-z. On the other hand, however, it has been thought that the sensitivity of [OIII] to the physical conditions of galaxies, which we have mentioned and shown in this section, makes itself uncertain for the SFR estimates.

Nevertheless, Bowman et al. (2019) have found a good correlation between UV SFRs and [OIII] luminosities in the range of SFR $\sim$ 0–100 $M_\odot$ yr^{-1}. Therefore it is worth examining a relation between Hα SFRs and [OIII] luminosities in our sample. Figure 4.8 shows the correlation between them, where the best-fit relation is given by

$$\log L([\mathrm{OIII}]) = 0.62 \log \mathrm{SFR}(\mathrm{H}\alpha) + 42.0. \tag{4.6}$$

We find a typical scatter of ± 0.16 dex around the best-fit relation. The tight correlation suggests that metallicities and/or ionization parameters do not fluctuate significantly at fixed SFRs. This can be understood given the result of Sanders et al. (2015) that the [OIII] strengths are mainly determined by gas-phase metallicities. Since SFRs and metallicities should be correlated via the SFMS and the mass-metallicity relation, galaxies in a certain SFR bin are expected to show similar metallicity values resulting in the tight distribution. In addition, the slope of Equation 4.6 is less than unity, which implies an extra dependence of the [OIII] luminosity. Qualitatively, this can be also explained by the mass-metallciity relation. In galaxies with large SFRs, there are many massive stars producing ionizing photons but their production efficiencies are decreased because massive galaxies tend to be metal-rich. Although measurements of the metallicities are necessary to confirm above interpretations, our result agrees well with Bowman et al. (2019). Thus we conclude that the [OIII] luminosity can be used as a SFR indicator at $2.1 < z < 2.5$.

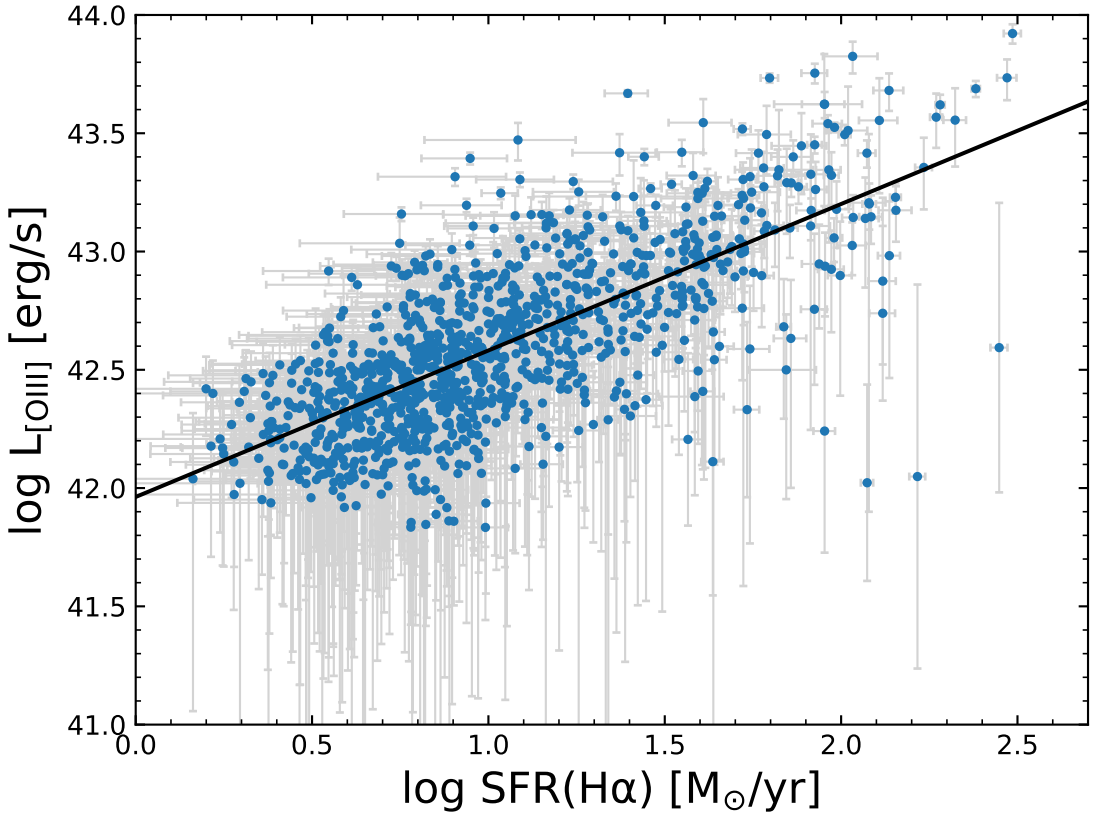

Figure 4.8: Correlation between [OIII] luminosities and Hα SFRs. The blue circles represent individual dual emitters in our sample, while the black line shows the best-fit relation.

4.4 Overlap with the Hα emitters

In the previous section, we have shown the correlations of the [OIII](+Hβ) strengths and other properties confirming that the strong [OIII] emitters are the galaxies with low stellar masses, high sSFRs, high excitation conditions, and less extinctions as expected from previous studies. Thus, given that the Hα emitters consist of diverse populations of star-forming galaxies as suggested by Oteo et al. (2015), we expect the [OIII] emitters to be a sub-population of the Hα emitters. In this section, we investigate how the two emitters overlap and what differentiates the dual emitters from the single emitters.

4.4.1 Distributions of properties

Figure 4.9 shows distributions of the stellar masses (upper left), Hα sSFRs (upper right), Hα equivalent widths (lower left), and [OIII]+Hβ equivalent widths (lower right). We perform Kolmogorov-Smirnov (KS) test for each of them to compare the distributions of each population.

According to the KS test, the stellar mass distributions of the three sub-populations are different from each other. However, as mentioned in § 4.1, there might be significant effects of the completeness. Especially, the distribution of the single [OIII] emitters peaked at the mass completeness limit of $\log M/M_{\odot} \sim 9$ suggests that there are a considerable number of galaxies, whose Hα fluxes are enough high to be detected in the $K_{\rm s}$-band but insufficient to be selected as the Hα emitters. Therefore it is difficult to know intrinsic stellar mass distributions of the sub-populations using our sample.

The Hα sSFR distributions of the dual emitters and the single Hα emitters are different with a p-value of the KS test of ~ 0.0004. It is clear that the second peak around $\log \mathrm{sSFR}\ \mathrm{yr}^{-1} \sim -7.5$ is more remarkable for the dual emitters. This indicates that galaxies with higher sSFRs tend to be the dual emitters, which is reasonable given that the [OIII] strengths increase with the sSFRs.

On the other hand, we find no significant difference between the distributions of the Hα equivalent widths, where the p-value of the KS test is 0.85. This seems slightly strange given that the Hα equivalent width has been thought to be a proxy of sSFR. However, we should note it is possible that there are contributions of massive galaxies in the high equivalent width end, for which our selection is more sensitive to Hα than [OIII], while high sSFR galaxies should be the low-mass ones.

The distributions of the [OIII]+Hβ equivalent widths are significantly different between the dual emitters and the single [OIII] emitters. This may be explained by the same reason as the stellar mass distributions because the peak value of the distribution of the single [OIII] emitters, $\log EW([\mathrm{OIII}] + \mathrm{H}\beta)/\text{Å} \sim 2.5$, typically corresponds to $\log M/M_{\odot} \sim 9$.

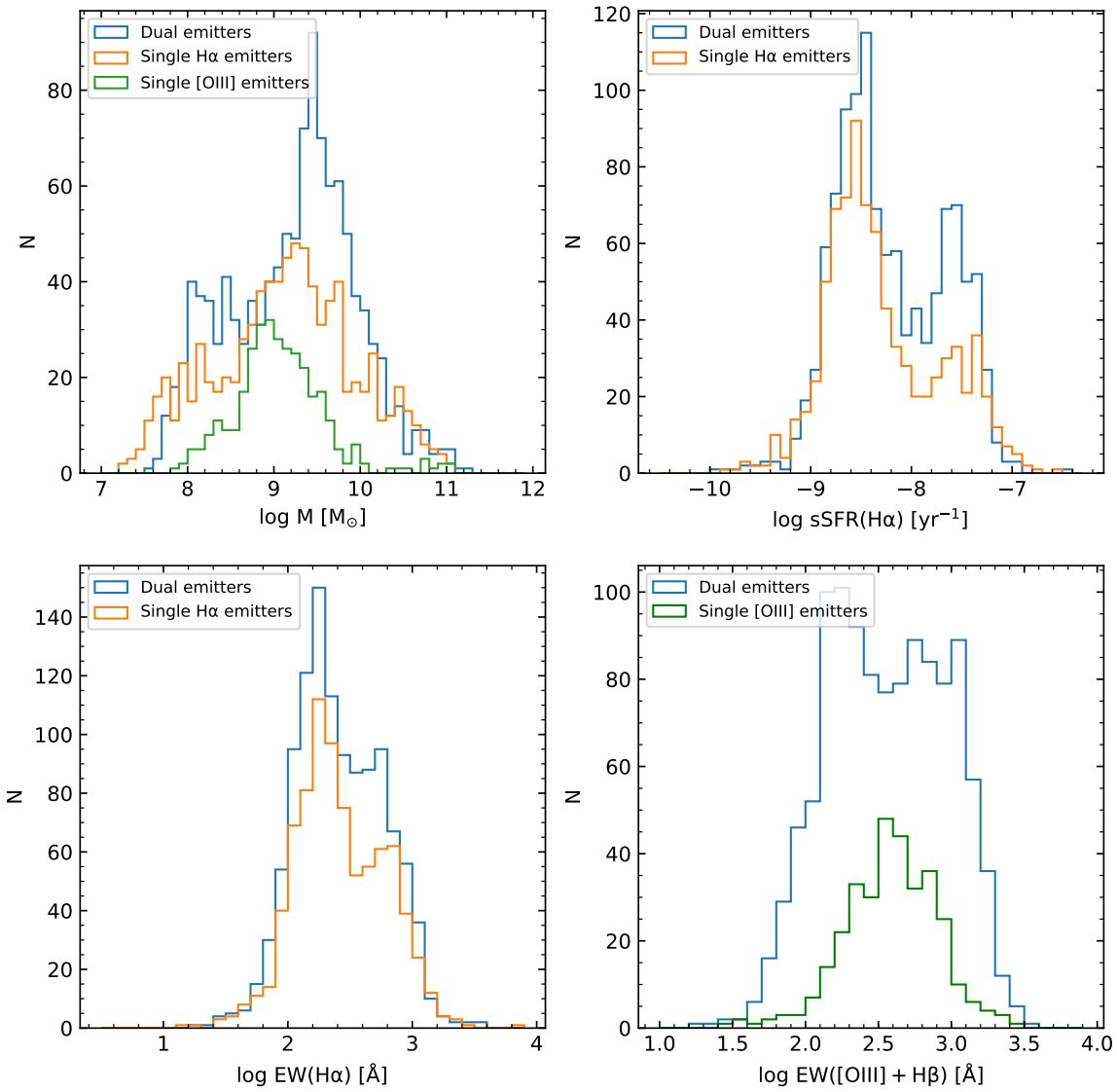

Figure 4.9: (Top left): Stellar mass distributions of the dual emitters, the single Hα emitters, and the single [OIII] emitters shown in blue, orange, and green, respectively, as well as the other panels. (Top right): Hα sSFR distributions of the dual emitters and the single Hα emitters. (Bottom left): Hα equivalent width distributions of the dual emitters and the single Hα emitters. (Bottom right): [OIII]+Hβ equivalent width distributions of the dual emitters and the single [OIII] emitters.

4.4.2 Dual emitter fraction

To approach the differences between the emitters more quantitatively, we investigate dual emitter fractions, which are ratios of the numbers of the dual emitters to the total as a function of stellar mass.

4.4.2.1 Effects of completeness

When considering the dual emitter fractions of our Hα emitters and [OIII] emitters, it is challenging to evaluate how the stellar mass completeness and the equivalent width completeness affect the results. Below the mass completeness limit of $\log M/M_{\odot} \sim 9$, as mentioned above, only strong Hα emitters are detected in the $K_{\rm s}$-band, which leads to a bias against the [OIII] emitters with weak Hα emissions. Therefore we use only the emitters above this stellar mass limit for the dual emitter fraction analysis.

Even at $\log M/M_{\odot} > 9$, the different sensitivities of our selection to the two emitters make a direct comparison difficult. As shown in Figure 3.6 and Figure 4.2, the equivalent width completeness of our Hα emitters increases with stellar masses while that of the [OIII] emitters is nearly constant if assuming the distributions of Reddy et al. (2018). This difference introduces a systematic bias at the high-mass end, where galaxies are more easily selected as the Hα emitters.

To evaluate this effect, we perform a brief simulation as follows. First, we assume the best-fit equivalent width and its typical scatter of Reddy et al. (2018) as the mean and standard deviation of the intrinsic distributions of the both emitters. Then we calculate what fractions of the emitters can be missed due to our limiting equivalent widths, which are functions of stellar mass. As a result, we find that the missing fraction of the Hα emitters decreases from 9% to nearly 0% with increasing the stellar mass between $9 < \log M/M_{\odot} < 11$, while that of the [OIII] emitters is 8–12% in the same stellar mass range. Therefore we take the different missing fractions of the emitters into account as the systematic uncertainties in the dual emitter fractions. Figure 4.10 shows the dual emitter fractions of both the Hα and [OIII] emitters with errorbars including poisson and the missing emitter fractions above.

The dual emitter fractions of the [OIII] emitters are higher than 70% in all the bins suggesting that they represent a sub-population of the Hα emitters as expected.

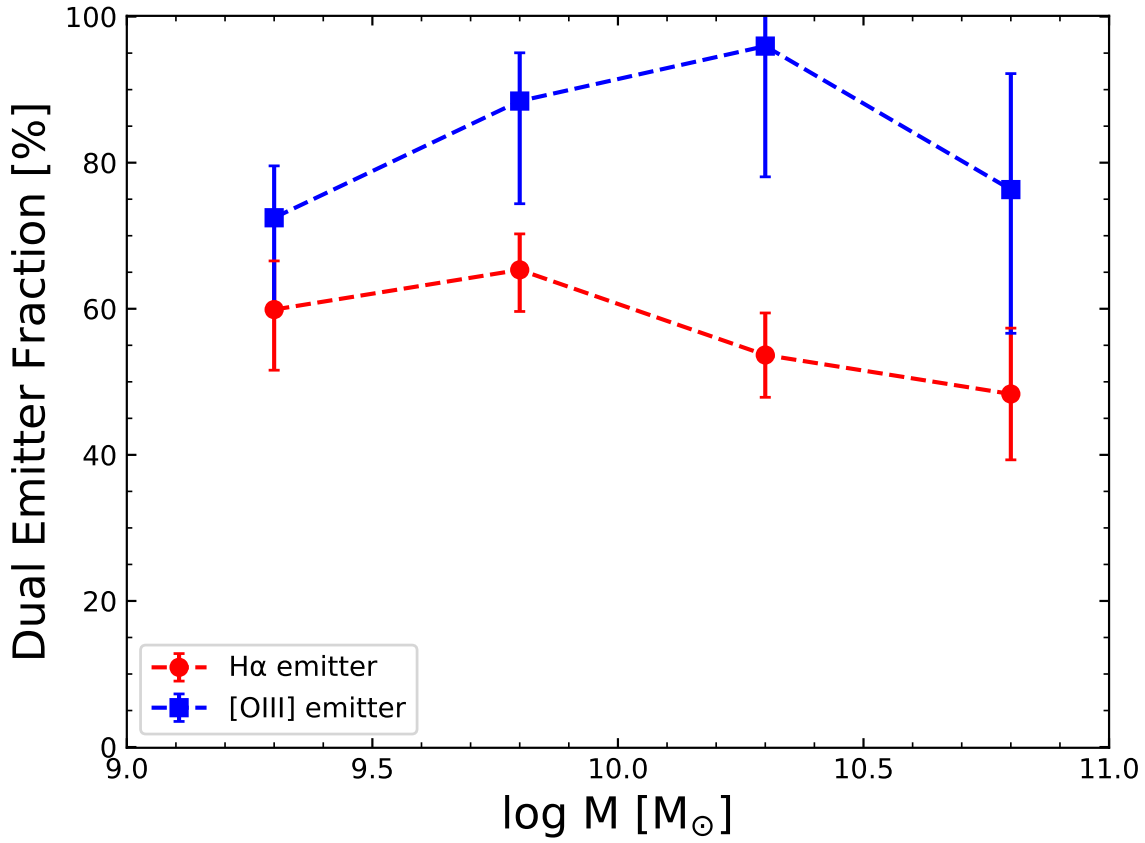

Figure 4.10: Dual emitter fractions as functions of stellar mass for both the Hα emitters (red) and the [OIII] emitters (blue). Each errorbar includes poisson and the uncertainties due to equivalent width sensitivities of our method.

It is not clear why the fraction is lower in the lowest-mass bin. Although above the 80% completeness limit, there might be a considerable number of galaxies which are detected by the K_s-band but not selected as the Hα emitters.

On the other hand, the dual emitter fractions of our Hα emitters are $\sim$ 50–60% in the range of $9 < \log M/M_\odot < 11$. There are some possible causes which differentiate the dual emitters from the single Hα emitters, such as metallicities, ionization parameters, and/or environments. A further investigation of the connections between different populations is one of our future works.

Chapter 5

Summary & Conclusions

5.1 Summary of this thesis

In this thesis, we have established a method to derive emission line fluxes from broad-band photometry and applied it to investigate properties of the Hα emitters and the [OIII] emitters at $z = 2.1$–2.5. A summary of our results is following.

In Chapter 2, we have described the details of our method, where the flux excess is defined as a difference between an observed flux and a continuum flux estimated by the SED fitting. When performing the SED fitting, it has been essential to take the effects of the emission lines into account, otherwise the continuum fluxes have been overestimated as well as stellar masses. Hence we have used the spectral templates of Bruzual & Charlot (2003) modified by Salmon et al. (2015) to contain the emission lines, where the line fluxes have been calculated from the number of ionizing photons.

We have compared Hα fluxes derived from the flux excesses with those derived by narrow-band color excesses, long-slit spectroscopy (ZFIRE), and integral-field spectroscopy (KMOS^{3D}), and found 73%, 67%, 62% of the galaxies have had consistent fluxes within a factor of 2 in each comparison, respectively. On the other hand, the scatters around the one-to-one relations have been 0.16, 0.21, and 0.23 dex in each comparison. As the typical scatter among the three methods rather than ours has been ~ 0.2 dex, we have concluded that our method have derived reasonable fluxes.

In Chapter 3, we have investigated properties of the Hα emitters at $2.1 < z < 2.5$

selected by the flux excesses in the K_s-band. Almost all galaxies in our sample have been located on the star-forming region of the UVJ diagram. Since our selection method and the UVJ diagram have been independent, this result has suggested that our method has worked properly to select the star-forming galaxies.

The sensitivity of our method to the Hα equivalent width depends on stellar masses of the galaxies due to the definition of the flux excess. Enough sensitivity has been achieved at $\log M/M_\odot \gtrsim 9$ when assuming the equivalent width distribution reported by Reddy et al. (2018). There has been many lower-mass galaxies with $\log M/M_\odot =$ 7.3–9.0 detected due to their large equivalent widths, which has implied their large sSFRs.

We have found a correlation between SFRs and the amounts of dust attenuation, where more active star-forming galaxies have been more obscured by the dust. In addition, A_V values derived from the IRX have been systematically larger than those estimated by the SED fitting. These offsets may be explained by the robustness of each method against the dust attenuation. Since the UV continua can be easily absorbed by the dust, the UV slopes only contain information on the surface regions. Therefore the amounts of the attenuation derived from the UV slopes can be underestimated in very dusty galaxies.

We have performed a simulation to evaluate the luminosity completeness of the Hα emitters and found it complete above $\log L_{\mathrm{H}\alpha}/\mathrm{erg\ s^{-1}} \sim 42.5$. When comparing our H$\alpha$ luminosity function with that of Sobral et al. (2013), they have shown a good agreement in the faint-end. On the other hand, our luminosity function has exhibited an excess in the bright-end. We have shown that the offset can be mostly explained by the missing Hα fluxes in Sobral et al. (2013). The luminosity dependence of the dust attenuation also has had a contribution to the offset as Sobral et al. (2013) had assumed $A_{\mathrm{H}\alpha} = 1$ mag for all the galaxies. Nevertheless, as the number of such luminous galaxies has been very small, our SFRD at $z \sim 2.3$ has been still consistent with previous studies.

The best-fit SFMS of our Hα emitters obtained at $\log M/M_\odot > 9$ has been consistent with those previously reported. In addition, there has been many galaxies with $\log M/\mathrm{M}_\odot =$ 7–9 having much higher sSFRs than expected from the extrapolation of

the SFMS. We have found that most of them have had large Hα/UV luminosity ratios, which can not be explained when assuming a constant SFH. This has suggested that they have been candidates of the galaxies which have experienced starbursts within ~ 10 Myr.

In Chapter 4 we have derived [OIII]+Hβ fluxes of the galaxies at $2.1 < z < 2.5$ from the flux excesses in the $H_{\rm s}$ and $H_{\rm l}$ medium-band filters. For the galaxies also selected as the Hα emitters, we have estimated the contribution of Hβ from the Hα information.

The limiting equivalent width of [OIII]+Hβ has also depended on the stellar mass, however, since the [OIII]+Hβ equivalent widths has more quickly decreased with increasing stellar masses as reported by Reddy et al. (2018), the expected equivalent completeness has not changed significantly with the stellar mass. The best-fit relation between the equivalent widths and stellar masses of our sample has agreed well with that of Reddy et al. (2018), which has suggested the validity of our method to these lines as well as Hα.

There has been also correlations between the [OIII]+Hβ equivalent width and galaxy properties other than the stellar mass. We have found that the strong [OIII] emitters have tended to have large sSFRs, large [OIII]λ5007/Hβ ratios, and small amounts of the dust attenuation, which have been consistent with the expectations from previous studies.

When it has come to the differences between the Hα emitters and the [OIII] emitters, the different sensitivities to each of them have made interpretations difficult. Nevertheless, there might have been a trend that the galaxies with large sSFRs have tended to be the dual emitters.

Finally we have investigated the dual emitter fractions in both populations as functions of stellar mass. Above $\log M/M_{\odot} \sim 9$, more than 70% of the [OIII] emitters have been also selected as the Hα emitters, while ~ 55% of the Hα emitters have been also selected as the [OIII] emitters. This result has qualitatively agreed with the idea that Hα emitters have represented diverse populations of star-forming galaxies while [OIII] emitters has been a sub-population characterized by large sSFRs, large [OIII]λ5007/Hβ ratios, and weak dust attenuation.

5.2 Conclusions and future prospects

5.2.1 Derivation of emission line flux from broad-band photometry

We have established the method to derive emission line fluxes from broad/medium-band photometry at $z = 2.1$–2.5 using the ZFOURGE catalog in combination with the SED fitting. This enables us to efficiently construct large samples of emission line galaxies at high-z universe.

However, there is still a room for improvements. For example, even if the observation were complete across whole the stellar mass range, the sensitivity of the $K_{\rm s}$-band filter to Hα would not be sufficient to select weak emitters at $\log M/M_{\odot} \sim 9$. In addition, since the observed-frame 2–3 μm is only sampled by the $K_{\rm s}$-band filter in the ZFOURGE, there might be uncertainties in determining the continuum levels when the $K_{\rm s}$-band fluxes are boosted by emission lines, even though the Spitzer/IRAC data puts the constraints on the longer wavelengths.

Simultaneous-color Wide-field Imager and Multi-object Spectrograph (SWIMS; e.g., Konishi et al. 2018) can improve the above situations with its K medium-band filters. SWIMS has three medium-band filters to cover 1.96–2.38 μm, which are more sensitive to emission lines than the $K_{\rm s}$-band filter due to their narrower bandwidths. Moreover, when the emission lines fall into one of the medium-band filters, the other two filters can sample continua depending on the combinations of the emission lines and redshifts. Hence the fitting accuracy of the SED fitting is expected to be improved or we can even estimate the continuum fluxes using the adjacent filters instead of the SED fitting, which will make it possible to evaluate the reliability of the fitting.

5.2.2 The most luminous Hα emitters

We have obtained the Hα luminosity function at $2.1 < z < 2.5$ considering the dust attenuation more properly than previous studies. As a result, we have shown that there has been more luminous Hα emitters in the bright-end of the luminosity function than previously known. Their Hα luminosities have corresponded to SFRs larger than

a few 100 $M_{\odot}\mathrm{yr}^{-1}$. However, the small number of the sample and their large AGN fraction have made interpretations difficult. To better understand the evolution of such luminous Hα emitters and their connections to other extreme populations such as sub-millimetre galaxies, FIR-detected galaxies, and extreme mergers, both larger imaging surveys and spectroscopic follow-ups are essential. Our method is an efficient way to detect such very rare objects.

5.2.3 Low-mass star-forming galaxies with high sSFR

The deep NIR data of the ZFOURGE has enabled us to discover many low-mass Hα emitters much above the SFMS at $2.1 < z < 2.5$. They have also exhibited the high Hα/UV ratios, which have suggested their bursty SFHs. Moreover, they have been also selected as the [OIII] emitters with extremely large ($\gtrsim$ 1000 Å) equivalent widths. This has made their very large sSFRs reliable because the [OIII] equivalent width has been an independent proxy of the sSFR.

Such populations are very important to understand galaxy evolution. For example, since the evolution of low-mass galaxies have been thought to be closely related to supernova feedbacks, precise measurements of their Hα/UV ratios by spectroscopic follow-up observations can put a constraint on feedback models.

In addition, galaxies with high Hα/UV ratios have been also found in the local and higher-z ($z > 4$) universe but typical stellar masses of such galaxies have been larger at high-z (Faisst et al. 2019, Emami et al. 2019). It has been thought that more massive galaxies have more rapidly assembled their stellar masses in the early universe, which has been known as the downsizing of galaxies. Therefore, if the typical stellar mass of the galaxies with bursty SFHs evolves with redshift, it might provide us with an important hint to understand evolutionary mechanisms of the downsizing of star-forming galaxies. Although we can apply our method to other filters to investigate the Hα/UV ratios of galaxies at different redshifts, however, we must carefully consider different image depths among the filters and the redshift dependence of the completeness due to the evolution of the Hα equivalent width.

The large [OIII] equivalent widths of the low-mass galaxies have suggested that

they have also had high [OIII]λ5007/Hβ ratios and weak dust attenuation as well as their large sSFRs. We can expect them to have also large ionization parameters, which will be ascertained by applying our method to the J medium-band filters of the ZFOURGE, into which the [OII] emission lines at $2.1 < z < 2.5$ fall. Such properties are the characteristics of the local galaxies with large escape fractions. Therefore further investigation for the strong [OIII] emitters may help us understand the ionizing photon escapes at $2.1 < z < 2.5$

In conclusion, the combination of our flux excess method and the deep imaging data of the ZFOURGE have enabled us to discover the star-forming galaxies with extreme properties, which are very interesting targets for future observations.

Bibliography

Baldwin, J. A., Phillips, M. M., & Terlevich, R. 1981, Publications of the Astronomical Society of the Pacific, 93, 5, doi: 10.1086/130766

Behroozi, P. S., Wechsler, R. H., & Conroy, C. 2013, The Astrophysical Journal, 770, 57, doi: 10.1088/0004-637X/770/1/57

Bell, E. F., Papovich, C., Wolf, C., et al. 2005, The Astrophysical Journal, 625, 23, doi: 10.1086/429552

Bouwens, R. J., Illingworth, G. D., Oesch, P. A., et al. 2015, The Astrophysical Journal, 803, 34, doi: 10.1088/0004-637X/803/1/34

Bowman, W. P., Zeimann, G. R., Ciardullo, R., et al. 2019, arXiv:1903.07573 [astro-ph]. http://arxiv.org/abs/1903.07573

Brammer, G. B., van Dokkum, P. G., & Coppi, P. 2008, The Astrophysical Journal, 686, 1503, doi: 10.1086/591786

Bruzual, G., & Charlot, S. 2003, Monthly Notices of the Royal Astronomical Society, 344, 1000, doi: 10.1046/j.1365-8711.2003.06897.x

Calzetti, D., Armus, L., Bohlin, R. C., et al. 2000, The Astrophysical Journal, 533, 682, doi: 10.1086/308692

Chabrier, G. 2003, Publications of the Astronomical Society of the Pacific, 115, 763, doi: 10.1086/376392

Dekel, A., Zolotov, A., Tweed, D., et al. 2013, Monthly Notices of the Royal Astronomical Society, 435, 999, doi: 10.1093/mnras/stt1338

Dutton, A. A., Van Den Bosch, F. C., & Dekel, A. 2010, Monthly Notices of the Royal Astronomical Society, no, doi: 10.1111/j.1365-2966.2010.16620.x

Emami, N., Siana, B., Weisz, D. R., et al. 2019, The Astrophysical Journal, 881, 71, doi: 10.3847/1538-4357/ab211a

Erb, D. K., Steidel, C. C., Shapley, A. E., et al. 2006, The Astrophysical Journal, 647, 128, doi: 10.1086/505341

Erb, D. K., Steidel, C. C., Trainor, R. F., et al. 2014, The Astrophysical Journal, 795, 33, doi: 10.1088/0004-637X/795/1/33

Faisst, A. L., Capak, P. L., Emami, N., Tacchella, S., & Larson, K. L. 2019, arXiv:1909.03076 [astro-ph]. http://arxiv.org/abs/1909.03076

Faisst, A. L., Capak, P., Hsieh, B. C., et al. 2016, The Astrophysical Journal, 821, 122, doi: 10.3847/0004-637X/821/2/122

Ferland, G., Korista, K., Verner, D., et al. 1998, Publications of the Astronomical Society of the Pacific, 110, 761, doi: 10.1086/316190

Fioc, M., & Rocca-Volmerange, B. 1997, Astronomy and Astrophysics, 326, 950. https://ui.adsabs.harvard.edu/abs/1997A%26A...326..950F/abstract

Forrest, B., Tran, K.-V. H., Broussard, A., et al. 2018, The Astrophysical Journal, 863, 131, doi: 10.3847/1538-4357/aad232

Fumagalli, M., Patel, S. G., Franx, M., et al. 2012, The Astrophysical Journal, 757, L22, doi: 10.1088/2041-8205/757/2/L22

Geach, J. E., Smail, I., Best, P. N., et al. 2008, Monthly Notices of the Royal Astronomical Society, 388, 1473, doi: 10.1111/j.1365-2966.2008.13481.x

Giacconi, R., Zirm, A., Wang, J., et al. 2002, The Astrophysical Journal Supplement Series, 139, 369, doi: 10.1086/338927

Graham, A. W., & Driver, S. P. 2005, Publications of the Astronomical Society of Australia, 22, 118, doi: 10.1071/AS05001

Gruppioni, C., Pozzi, F., Rodighiero, G., et al. 2013, Monthly Notices of the Royal Astronomical Society, 432, 23, doi: 10.1093/mnras/stt308

Hayashi, M., Motohara, K., Shimasaku, K., et al. 2009, The Astrophysical Journal, 691, 140, doi: 10.1088/0004-637X/691/1/140

Hopkins, P. F., Kereš, D., Oñorbe, J., et al. 2014, Monthly Notices of the Royal Astronomical Society, 445, 581, doi: 10.1093/mnras/stu1738

Inoue, A. K. 2011, Monthly Notices of the Royal Astronomical Society, 415, 2920, doi: 10.1111/j.1365-2966.2011.18906.x

Kashino, D., Silverman, J. D., Sanders, D., et al. 2017, The Astrophysical Journal, 835, 88, doi: 10.3847/1538-4357/835/1/88

Kennicutt, J. 1998, Annual Review of Astronomy and Astrophysics, 36, 189, doi: 10.1146/annurev.astro.36.1.189

Kennicutt, Jr, R. C., & Evans, II, N. J. 2012, Annual Review of Astronomy and Astrophysics, 50, 531, doi: 10.1146/annurev-astro-081811-125610

Khostovan, A. A., Sobral, D., Mobasher, B., et al. 2016, Monthly Notices of the Royal Astronomical Society, 463, 2363, doi: 10.1093/mnras/stw2174

Konishi, M., Motohara, K., Takahashi, H., et al. 2018, 0702, 1070226, doi: 10.1117/12.2310060

Koprowski, M. P., Dunlop, J. S., Michałowski, M. J., et al. 2017, Monthly Notices of the Royal Astronomical Society, 471, 4155, doi: 10.1093/mnras/stx1843

Koyama, Y., Kodama, T., Hayashi, M., et al. 2015, Monthly Notices of the Royal Astronomical Society, 453, 879, doi: 10.1093/mnras/stv1599

Kriek, M., & Conroy, C. 2013, The Astrophysical Journal Letters, 775, L16, doi: 10.1088/2041-8205/775/1/L16

Kriek, M., van Dokkum, P. G., Labbe, I., et al. 2009, The Astrophysical Journal, 700, 221, doi: 10.1088/0004-637X/700/1/221

Lamareille, F., Brinchmann, J., Contini, T., et al. 2009, Astronomy and Astrophysics, 495, 53, doi: 10.1051/0004-6361:200810397

Lawrence, A., Warren, S. J., Almaini, O., et al. 2007, Monthly Notices of the Royal Astronomical Society, 379, 1599, doi: 10.1111/j.1365-2966.2007.12040.x

Lee, J. C., Ly, C., Spitler, L., et al. 2012, Publications of the Astronomical Society of the Pacific, 124, 782, doi: 10.1086/666528

Lee, N., Sanders, D. B., Casey, C. M., et al. 2013, The Astrophysical Journal, 778, 131, doi: 10.1088/0004-637X/778/2/131

Leitherer, C., Ekström, S., Meynet, G., et al. 2014, The Astrophysical Journal Supplement Series, 212, 14, doi: 10.1088/0067-0049/212/1/14

Madau, P., & Dickinson, M. 2014, Annual Review of Astronomy and Astrophysics, 52, 415, doi: 10.1146/annurev-astro-081811-125615

Mannucci, F., Cresci, G., Maiolino, R., Marconi, A., & Gnerucci, A. 2010, Monthly Notices of the Royal Astronomical Society, 408, 2115, doi: 10.1111/j.1365-2966.2010.17291.x

Meurer, G. R., Heckman, T. M., & Calzetti, D. 1999, The Astrophysical Journal, 521, 64, doi: 10.1086/307523

Morgan, H. L., & Edmunds, M. G. 2003, Monthly Notices of the Royal Astronomical Society, 343, 427, doi: 10.1046/j.1365-8711.2003.06681.x

Nakajima, K., & Ouchi, M. 2014, Monthly Notices of the Royal Astronomical Society, 442, 900, doi: 10.1093/mnras/stu902

Nanayakkara, T., Glazebrook, K., Kacprzak, G. G., et al. 2016, The Astrophysical Journal, 828, 21, doi: 10.3847/0004-637X/828/1/21

Nelson, E. J., van Dokkum, P. G., Förster Schreiber, N. M., et al. 2016, The Astrophysical Journal, 828, 27, doi: 10.3847/0004-637X/828/1/27

Nestor, D. B., Shapley, A. E., Steidel, C. C., & Siana, B. 2011, The Astrophysical Journal, 736, 18, doi: 10.1088/0004-637X/736/1/18

Nordon, R., Lutz, D., Saintonge, A., et al. 2013, The Astrophysical Journal, 762, 125, doi: 10.1088/0004-637X/762/2/125

Oteo, I., Sobral, D., Ivison, R. J., et al. 2015, Monthly Notices of the Royal Astronomical Society, 452, 2018, doi: 10.1093/mnras/stv1284

Overzier, R. A., Heckman, T. M., Wang, J., et al. 2011, The Astrophysical Journal Letters, 726, L7, doi: 10.1088/2041-8205/726/1/L7

Persson, S. E., Murphy, D. C., Smee, S., et al. 2013, Publications of the Astronomical Society of the Pacific, 125, 654, doi: 10.1086/671164

Qin, J., Zheng, X. Z., Wuyts, S., Pan, Z., & Ren, J. 2019, arXiv:1909.13505 [astro-ph]. http://arxiv.org/abs/1909.13505

Rasappu, N., Smit, R., Labbé, I., et al. 2016, Monthly Notices of the Royal Astronomical Society, 461, 3886, doi: 10.1093/mnras/stw1484

Reddy, N. A., & Steidel, C. C. 2009, The Astrophysical Journal, 692, 778, doi: 10.1088/0004-637X/692/1/778

Reddy, N. A., Steidel, C. C., Pettini, M., Bogosavljević, M., & Shapley, A. E. 2016, The Astrophysical Journal, 828, 108, doi: 10.3847/0004-637X/828/2/108

Reddy, N. A., Shapley, A. E., Sanders, R. L., et al. 2018, The Astrophysical Journal, 869, 92, doi: 10.3847/1538-4357/aaed1e

Rodighiero, G., Daddi, E., Baronchelli, I., et al. 2011, The Astrophysical Journal, 739, L40, doi: 10.1088/2041-8205/739/2/L40

Salmon, B., Papovich, C., Finkelstein, S. L., et al. 2015, The Astrophysical Journal, 799, 183, doi: 10.1088/0004-637X/799/2/183

Sanders, R. L., Shapley, A. E., Kriek, M., et al. 2015, The Astrophysical Journal, 816, 23, doi: 10.3847/0004-637X/816/1/23

Schaerer, D., & de Barros, S. 2009, Astronomy and Astrophysics, 502, 423, doi: 10.1051/0004-6361/200911781

Scoville, N., Aussel, H., Brusa, M., et al. 2007, The Astrophysical Journal Supplement Series, 172, 1, doi: 10.1086/516585

Skelton, R. E., Whitaker, K. E., Momcheva, I. G., et al. 2014, The Astrophysical Journal Supplement Series, 214, 24, doi: 10.1088/0067-0049/214/2/24

Smit, R., Bouwens, R. J., Labbé, I., et al. 2014, The Astrophysical Journal, 784, 58, doi: 10.1088/0004-637X/784/1/58

Smit, R., Bouwens, R. J., Franx, M., et al. 2015, The Astrophysical Journal, 801, 122, doi: 10.1088/0004-637X/801/2/122

Sobral, D., Best, P. N., Smail, I., et al. 2014, Monthly Notices of the Royal Astronomical Society, 437, 3516, doi: 10.1093/mnras/stt2159

Sobral, D., Smail, I., Best, P. N., et al. 2013, Monthly Notices of the Royal Astronomical Society, 428, 1128, doi: 10.1093/mnras/sts096

Sobral, D., Best, P. N., Geach, J. E., et al. 2009, Monthly Notices of the Royal Astronomical Society, 398, 75, doi: 10.1111/j.1365-2966.2009.15129.x

Sparre, M., Hayward, C. C., Feldmann, R., et al. 2017, Monthly Notices of the Royal Astronomical Society, 466, 88, doi: 10.1093/mnras/stw3011

Speagle, J. S., Steinhardt, C. L., Capak, P. L., & Silverman, J. D. 2014, The Astrophysical Journal Supplement Series, 214, 15, doi: 10.1088/0067-0049/214/2/15

Spitler, L. R., Straatman, C. M. S., Labbé, I., et al. 2014, The Astrophysical Journal, 787, L36, doi: 10.1088/2041-8205/787/2/L36

Stark, D. P., Schenker, M. A., Ellis, R., et al. 2013, The Astrophysical Journal, 763, 129, doi: 10.1088/0004-637X/763/2/129

Steidel, C. C., Bogosavljević, M., Shapley, A. E., et al. 2018, The Astrophysical Journal, 869, 123, doi: 10.3847/1538-4357/aaed28

Steidel, C. C., Rudie, G. C., Strom, A. L., et al. 2014, The Astrophysical Journal, 795, 165, doi: 10.1088/0004-637X/795/2/165

Straatman, C. M. S., Spitler, L. R., Quadri, R. F., et al. 2016, The Astrophysical Journal, 830, 51, doi: 10.3847/0004-637X/830/1/51

Suzuki, T. L., Minowa, Y., Koyama, Y., et al. 2019, Publications of the Astronomical Society of Japan, 71, 69, doi: 10.1093/pasj/psz047

Suzuki, T. L., Kodama, T., Sobral, D., et al. 2016, Monthly Notices of the Royal Astronomical Society, 462, 181, doi: 10.1093/mnras/stw1655

Tacchella, S., Dekel, A., Carollo, C. M., et al. 2016, Monthly Notices of the Royal Astronomical Society, 457, 2790, doi: 10.1093/mnras/stw131

Tadaki, K.-i., Kodama, T., Tanaka, I., et al. 2013, The Astrophysical Journal, 778, 114, doi: 10.1088/0004-637X/778/2/114

Tasca, L. A. M., Le Fèvre, O., Ribeiro, B., et al. 2017, Astronomy & Astrophysics, 600, A110, doi: 10.1051/0004-6361/201527963

Thomas, D., Steele, O., Maraston, C., et al. 2013, Monthly Notices of the Royal Astronomical Society, 431, 1383, doi: 10.1093/mnras/stt261

Tomczak, A. R., Quadri, R. F., Tran, K.-V. H., et al. 2014, The Astrophysical Journal, 783, 85, doi: 10.1088/0004-637X/783/2/85

Trainor, R. F., Strom, A. L., Steidel, C. C., & Rudie, G. C. 2016, The Astrophysical Journal, 832, 171, doi: 10.3847/0004-637X/832/2/171

Trujillo, I., Aguerri, J., Cepa, J., & Gutiérrez, C. 2001, Monthly Notices of the Royal Astronomical Society, 328, 977, doi: 10.1046/j.1365-8711.2001.04937.x

Tziamtzis, A., Lundqvist, P., Gröningsson, P., & Nasoudi-Shoar, S. 2011, Astronomy ¥ Astrophysics, 527, A35, doi: 10.1051/0004-6361/201015576

van Dokkum, P. G., Whitaker, K. E., Brammer, G., et al. 2010, The Astrophysical Journal, 709, 1018, doi: 10.1088/0004-637X/709/2/1018

Villar, V., Gallego, J., Pérez- González, P. G., et al. 2008, The Astrophysical Journal, 677, 169, doi: 10.1086/528942

Whitaker, K. E., van Dokkum, P. G., Brammer, G., & Franx, M. 2012, The Astrophysical Journal, 754, L29, doi: 10.1088/2041-8205/754/2/L29

Whitaker, K. E., Labbe, I., van Dokkum, P. G., et al. 2011, The Astrophysical Journal, 735, 86, doi: 10.1088/0004-637X/735/2/86

Whitaker, K. E., Franx, M., Leja, J., et al. 2014, The Astrophysical Journal, 795, 104, doi: 10.1088/0004-637X/795/2/104

Williams, R. J., Quadri, R. F., Franx, M., van Dokkum, P., & Labbé, I. 2009, The Astrophysical Journal, 691, 1879, doi: 10.1088/0004-637X/691/2/1879

Wisnioski, E., Schreiber, N. M. F., Fossati, M., et al. 2019, arXiv:1909.11096 [astro-ph]. http://arxiv.org/abs/1909.11096

Wuyts, S., Labbe, I., Franx, M., et al. 2007, The Astrophysical Journal, 655, 51, doi: 10.1086/509708

Yabe, K., Ohta, K., Akiyama, M., et al. 2015, Publications of the Astronomical Society of Japan, 67, 102, doi: 10.1093/pasj/psv079